EUMETSAT Satellite Application Facility on Climate Monitoring

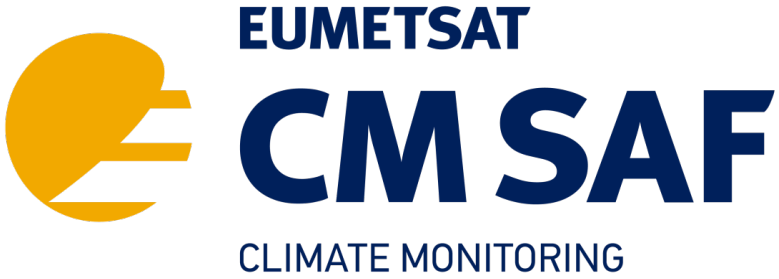

Algorithm Theoretical Basis Document
CM SAF Cloud, Albedo, Radiation data record, AVHRR-based, Edition 3 (CLARA-A3)
Surface Black-sky, White-sky and Blue-sky Albedo

DOI: 10.5676/EUM_SAF_CM/CLARA_AVHRR/V003

	TCDR	ICDR
Black-sky albedo from AVHRR-GAC	**CM-11222**	**CM-6221**
White-sky albedo from AVHRR-GAC	**CM-11223**	**CM-6223**
Blue-sky albedo from AVHRR-GAC	**CM-11224**	**CM-6224**

Reference Number: SAF/CM/FMI//ATBD/CLARA/SAL
Issue/Revision Index: 3.3
Date: 06.02.2023

Document Signature Table

	Name	Function	Signature	Date
Author	Terhikki Manninen, Aku Riihelä, Emmihenna Jääskeläinen	CM SAF scientists		06.02.2023
Editor	Marc Schröder	CM SAF Science Coordinator	2	06.02.2023
Approval	Steering Group			
Release	Rainer Hollmann	Project Manager		

Distribution List

Internal Distribution	
Name	**No. Copies**
DWD / Archive	

External Distribution		
Company	**Name**	**No. Copies**
Public		

Document Change Record

Issue/ Revision	Date	DCN No.	Changed Pages/Paragraphs
3.0	23.04.2021	SAF/CM/FMI/ATBD/CLARA/SAL	Initial version for PCR 3.2 review
3.1	16.06.2021	SAF/CM/FMI/ATBD/CLARA/SAL	RIDs from PCR 3.2 implemetend
3.2	05.10.2022	SAF/CM/FMI/ATBD/CLARA/SAL	Updates for joint DRR3.2/ORR covering TCDR and ICDR Layout revision

3.3	06.02.2023	SAF/CM/FMI/ATBD/CLARA/SAL	Updates following discussions at DRR3.2/ORR Adapted iCDR processing

Applicable Documents

Reference	Title	Code
AD 1	EUMETSAT CM SAF CDOP 4 Product Requirements Document (PRD)	SAF/CM/DWD/PRD/ Issue 4.1

Reference Documents

Reference	Title	Code
RD 1		
RD 2		

Table of Contents

1 The EUMETSAT SAF on Climate Monitoring (CM SAF) 10

2 Introduction to CLARA-A3 SAL, CLARA-A3 WAL and CLARA-A3 BAL 12

3 CLARA-A3 SAL, WAL and BAL Algorithm Description 14

3.1 Definitions of albedo quantities 14

3.1.1 SAL (Black-sky surface albedo) 14

3.1.2 WAL (White-sky surface albedo) 15

3.1.3 BAL (Blue-sky surface albedo) 15

3.2 Overview of SAL, WAL, and BAL retrieval in CLARA-A3 16

3.3 Calculating SAL over land areas 20

3.3.1 Topography correction 20

3.3.2 Atmospheric correction 22

3.3.3 BRDF 29

3.4 Calculating albedo estimates over sea areas 35

3.4.1 Sea surface albedo using wind speed data 37

3.4.2 Sea ice 40

3.5 Calculating SAL over snow-covered areas 41

3.6 Narrow-to-Broadband Conversion of SAL 42

3.7 Level 3 processing for spatiotemporally aggregated SAL, WAL, and BAL 44

3.7.1 Overview & spatio-temporal averaging 44

3.7.2 Deriving final albedo estimates, cloud probability usage 45

4 Uncertainty and sensitivity analysis of the algorithm 54

4.1 Input data uncertainty 54

4.2 Uncertainty budget estimates 55

4.3 AOD sensitivity analysis 57

4.3.1 SMAC atmospheric corrections sensitivity analysis 59

4.3.2 SAL albedo values sensitivity to change of AOD 63

5 Assumptions and limitations 70

5.1 Assumptions and mandatory inputs 70

5.2 Constraints and limitations 70

6 ICDR specific adaptations 73

7 References 74

8 Appendix A: Topography effect on BRDF 79

9 Appendix B: SMAC numeric equations 91

10 Appendix C: Symbols 92

11 Glossary – List of Acronyms in alphabetical order 93

List of Tables

Table 3-1: Kernel coefficients used in CLARA SAL BRDF correction computation. Coefficients are land cover specific. Coefficients a_{x1} are for red channel, a_{x2} are for NIR channel. (Wu et al. 1995)..... 32

Table 3-2: The rules for reclassifying USGS land cover classification to conform with available BRDF model classes 33

Table 3-3: The rules for reclassifying GLC2000 land cover classification to conform with available BRDF model classes. 33

Table 3-4: The rules for reclassifying GlobCover land cover classification to conform with available BRDF model classes. 33

Table 3-5: The Land use classifications used in CLARA-A3 SAL. 34

Table 3-6: Data gaps of the daily OSI-SAF ice concentration data for northern hemisphere (NH) and southern hemisphere (SH). 41

Table 3-7: Parameter values of eq. 66 for monthly mean, standard deviation, skewness and kurtosis of surface albedo. 47

Table 3-8. Simulated statistics for the absolute and relative absolute differences of the estimates (^) and true values of albedo (α), standard deviation (σ) skewness (γ) and kurtosis (β). The calculations were made for simulated true albedo values (α) of 10%, 20%, 30%, 40%, 50%, 60%, 70% and 80%. The albedo values are in the range 0 – 100%..... 47

Table 3-9: Monthly mean black-sky surface albedo values based on AVHRR reflectance and *CP* values and the monthly means of the corresponding (satellite clear-sky overpass) times of in situ surface albedo measurements for several in situ sites (König-Langlo et el., 2013; Driemel et al., 2018). The number of observations included in the mean value are given as well as the mean distance of the satellite pixels from the in situ measurement mast. 50

Table 4-1: Uncertainty estimates for input data used for SAL retrieval and their effect on SAL accuracy. 54

Table 4-2: Estimates of uncertainty sources and their effects on the observed CLARA SAL product. All values are in relative albedo (percent). 55

Table 4-3: Estimates of uncertainty sources (not already included in retrieval of SAL) and their effects on the observed CLARA WAL product. All values are in relative albedo (percent). 57

Table 4-4: Estimates of uncertainty sources (not already included in retrieval of SAL and WAL) and their effects on the observed CLARA BAL product. All values are in relative albedo (percent)..... 57

Table 4-5: Mean and standard deviation of the SAL values of the test area (Europe) using different AOD values. 64

Table 4-6: Mean and standard deviation of the change in SAL values caused by the change in AOD value in Europe..... 65

Table 4-7: The mean absolute difference in SAL values for different levels of albedo in Europe..... 65

Table 4-8: Mean and standard deviation of the SAL values of the test area using different AOD values. 67

Table 4-9: Mean and standard deviation of the change in SAL values caused by the change in AOD value. 67

Table 4-10: The mean absolute difference in SAL values for different levels of albedo. 68

Table 8-1: The average land use class albedo values derived for the USGS land use classes (http://edcdaac.usgs.gov/glcc/glcc.html) using PlaPaDa data base, urban albedo calculator and Finnish Meteorological Institute (FMI) radiation data of snow covered land (Breuer et al., 2003, http://www.staff.uni-giessen.de/~gh1461/plapada/plapada.html). 86

List of Figures

Figure 3-1: The geometry of the angles used in definition of the black-sky surface albedo (directional-hemispherical reflectance)..... 15

Figure 3-2: Relationships of the albedo quantities in CLARA-A3 SAL. NOBS refers to the amount of valid satellite observations of snow and/or vegetated conditions..... 16

Figure 3-3: An illustration of the black-sky surface albedo product (SAL) computation phases. 17

Figure 3-4: Level 2 processing flow in CLARA-A3 SAL. 19

Figure 3-5: Location difference between apparent and true pixel locations..... 21

Figure 3-6: Illustration of contributions to the atmospheric correction equation. After Tanré, 1990. ... 23

Figure 3-7: Example of data division using the AVHRR LUC data. The coloured areas (black, red and blue) have all the land use classification value 1 (Broadleaf Evergreen Forest). Based on the location the land use class is divided into 3 areas (marked by the different colors), which are handled separately in processing the AOD time series. 28

Figure 3-8: An example of calculated OMI-AOD on 1st of May 2005. 29

Figure 3-9: The BRDF geometry and relevant angles. For all non-isotropic objects, the reflectance changes as the illumination (subscript s) and viewing (subscript v) angles for elevation and azimuth change. 30

Figure 3-10: Variation of wind speed in one pixel during 1979-1984 and 1987-1996 as a function of the day of the year (DOY). The wind speed estimates are based on SMMR or SSM/I data. The regression polynomial (red curve) is w = 7.43593 + 0.0253204 DOY + 0.000017422 DOY^2 - 2.46116*10^-7 DOY^3, where w is the wind speed. This example point is situated at 60°N, 42°E..... 39

Figure 3-11: Wind speed examples based on SMMR (top left), anemometer (top right), SSM/I (bottom left) and SSMIS (bottom right) data. The values are in m/s. 40

Figure 3-12: Satellite zenith and azimuth angles of successful CLARA-A3 SAL retrievals during 2020 at Summit Camp in Greenland (left). The polar plot shows viewing (satellite) zenith angles in the radial axis and viewing azimuth angles in the angular axis. On the right, an example of the deviation of angular snow reflectance from its isotropic mean as modeled by the snow kernel proposed by Jiao et al. (2019). 42

Figure 3-13: Overview of CLARA-A3 SAL/WAL/BAL level 3 processing flow 45

Figure 3-14: Absolute (left) and relative (right) difference between the albedo estimate and the true albedo value as a function of the number of points included in the mean albedo value..... 48

Figure 3-15: The SAL retrieval distributions at the BSRN stations Desert Rock, Southern Great Plains in April 2009 and Cabauw in July 2081 and Neumayer Station in November July 2008. The cloud probability of the satellite retrievals is indicated with the yellow-graytones. The final albedo estimates (eq. 67) are shown as dashed red lines and the in situ albedo distributions as dotted blue curves. The map (© Google Maps) shows the locations of the measurement site within a square of 10 km x 10 km. 49

Figure 3-16: The SAL retrieval distributions at Laptev Sea (75.320°N, 125.720°E), Arctic Ocean (73.370°N, 139.180°W) and Kara Sea (2.680°N, 62.860°E) in April 2009 and July 2018. The cloud probability of the satellite retrievals is indicated with the yellow-graytones. 50

Figure 4-1: The monthly AOD distributions in 2010 of the global AOD data set based on TOMS/OMI time series used for atmospheric correction in SAL retrieval. The mean values are indicated by solid vertical lines and the 10% and 90% quantiles with dashed vertical lines. 59

Figure 4-2: The sensitivity of VIS and NIR albedos of barren ground on changing AOD for different TOA reflectances using SMAC with moderate angles. 60

Figure 4-3: The sensitivity of VIS and NIR albedos of barren ground on changing AOD for different TOA reflectances using SMAC with extreme angles. 60

Figure 4-4: The sensitivity of VIS and NIR albedos of cropland on changing AOD for different TOA reflectances using SMAC with moderate angles. 60

Figure 4-5: The sensitivity of VIS and NIR albedos of cropland on changing AOD for different TOA reflectances using SMAC with extreme angles. 61

Figure 4-6: The sensitivity of VIS and NIR albedos of forest on changing AOD for different TOA reflectances using SMAC with moderate angles. 61

Figure 4-7: The sensitivity of VIS and NIR albedos of forest on changing AOD for different TOA reflectances using SMAC with extreme angles. 62

Figure 4-8: The sensitivity of VIS and NIR albedos of grassland on changing AOD for different TOA reflectances using SMAC with moderate angles. 62

Figure 4-9: The sensitivity of VIS and NIR albedos of grassland on changing AOD for different TOA reflectances using SMAC with extreme angles. 63

Figure 4-10: SAL values of Europe using AOD values of 0.1, 0.3, 0.5 and daily AOD. The islands of Sardinia and Corse are at the lower right corner. 64

Figure 4-11: The absolute change in SAL albedo values in Europe between 0.3->0.1, 0.5->0.1 and daily->0.1. The pixels without data are marked with grey. 65

Figure 4-12: SAL values of North Western Africa using different AOD values. SAL value 0 represents pixels without data. 66

Figure 4-13: The absolute change in SAL albedo values between (from left to right) 0.3->0.1, 0.5->0.1 and daily->0.1. The pixels without data have been marked with grey. 69

Figure 8-1: The ASTER DEM (left) and corresponding slope (middle) and azimuth (right) angle images from the Alps. 79

Figure 8-2: The possible sun and satellite zenith angle range for the inclined terrain case (red arrows). The flat terrain case would have a full 0 … 90° range (blue arrows included). 81

Figure 8-3: The ratio of the inclined and flat terrain short wave albedo of barren land for various ground (θ_g) and sun (θ_s) inclination angle and the azimuth angle difference (ϕ_s-ϕ_g) values. The pink shade of the images corresponding to ϕ_s-ϕ_g=90° and ϕ_s-ϕ_g=179° indicates the angle combinations, which do not contribute to the reflection at all. The lines are spaced with 2 % interval. The white area shows the parameter range producing inclined terrain albedo values matching flat terrain albedo values with ±1% accuracy. 82

Figure 8-4: The ratio of the inclined and flat terrain short wave albedo of grassland for various ground (θ_g) and sun (θ_s) inclination angle and the azimuth angle difference (ϕ_s-ϕ_g) values. The pink shade of the images corresponding to ϕ_s-ϕ_g=90° and ϕ_s-ϕ_g=179° indicates the angle combinations, which do not contribute to the reflection at all. The lines are spaced with 2 % interval. The white area shows the parameter range producing inclined terrain albedo values matching flat terrain albedo values with ±1% accuracy. 83

Figure 8-5: The ratio of the inclined and flat terrain short wave albedo of cropland for various ground (θ_g) and sun (θ_s) inclination angle and the azimuth angle difference (ϕ_s-ϕ_g) values. The pink shade of the images corresponding to ϕ_s-ϕ_g=90° and ϕ_s-ϕ_g=179° indicates the angle combinations, which do not contribute to the reflection at all. The lines are spaced with 2 % interval. The white area shows the parameter range producing inclined terrain albedo values matching flat terrain albedo values with ±1% accuracy. 84

Figure 8-6: The ratio of the inclined and flat terrain short wave albedo of forested land for various ground (θ_g) and sun (θ_s) inclination angle and the azimuth angle difference (ϕ_s-ϕ_g) values. The pink shade of the images corresponding to ϕ_s-ϕ_g=90° and ϕ_s-ϕ_g=179° indicates the angle combinations, which do not contribute to the reflection at all. The lines are spaced with 2 % interval. The white area shows the parameter range producing inclined terrain albedo values matching flat terrain albedo values with ±1% accuracy. 85

Figure 8-7: The histogram of the true terrain and flat terrain albedo ratio values for the Alpine test area for two sun and satellite angle cases. Left) The sun zenith angle was 31 °, the sun azimuth angle was 141°, the satellite zenith angle was 25° and the satellite azimuth angle was 181°. Right) The sun zenith angle was 70 °, the sun azimuth angle was 118°, the satellite zenith angle was 50° and the satellite azimuth angle was 181°. 87

Figure 8-8: The difference between the flat terrain and true terrain albedo values at the Alps. The slope and aspect values were derived from ASTER DEMs and the land use classes from USGS land use map. The sun zenith angle was 31°, the sun azimuth angle was 141°, the satellite zenith angle was 25° and the satellite azimuth angle was 181° 88

Figure 8-9: The difference between the flat terrain and true terrain albedo values at the Alps. The slope and aspect values were derived from ASTER DEMs and the land use classes from USGS land use map. The sun zenith angle was 70°, the sun azimuth angle was 118°, the satellite zenith angle was 50° and the satellite azimuth angle was 181°. 89

Figure 8-10: The difference between the flat terrain and true terrain albedo values at the Alps. A detail of Figure 7-8 (left) and Figure 7-9 (right) has been median filtered to 1 km resolution to correspond to the CLARA SAL product. The colour code is the same as in those two Figures. 90

1 The EUMETSAT SAF on Climate Monitoring (CM SAF)

The importance of climate monitoring with satellites was recognized in 2000 by EUMETSAT Member States when they amended the EUMETSAT Convention to affirm that the EUMETSAT mandate is also to “contribute to the operational monitoring of the climate and the detection of global climatic changes". Following this, EUMETSAT established within its Satellite Application Facility (SAF) network a dedicated centre, the SAF on Climate Monitoring (CM SAF, http://www.cmsaf.eu).

The consortium of CM SAF currently comprises the Deutscher Wetterdienst (DWD) as host institute, and the partners from the Royal Meteorological Institute of Belgium (RMIB), the Finnish Meteorological Institute (FMI), the French National Centre for Scientific Research (CNRS), the Royal Meteorological Institute of the Netherlands (KNMI), the Swedish Meteorological and Hydrological Institute (SMHI), the Federal Office of Meteorology and Climatology MeteoSwiss (MeteoSwiss), and the Meteorological Service of the United Kingdom (UK MetOffice). Since the beginning in 1999, the EUMETSAT Satellite Application Facility on Climate Monitoring (CM SAF) has developed and will continue to develop capabilities for a sustained generation and provision of Climate Data Records (CDR’s) derived from operational meteorological satellites.

In particular the generation of long-term data sets is pursued. The ultimate aim is to make the resulting data sets suitable for the analysis of climate variability and potentially the detection of climate trends. CM SAF works in close collaboration with the EUMETSAT Central Facility and liaises with other satellite operators to advance the availability, quality and usability of Fundamental Climate Data Records (FCDRs) as defined by the Global Climate Observing System (GCOS). As a major task the CM SAF utilizes FCDRs to produce records of Essential Climate Variables (ECVs) as defined by GCOS. Thematically, the focus of CM SAF is on ECVs associated with the global energy and water cycle.

Another essential task of CM SAF is to produce data sets that can serve applications related to the new Global Framework of Climate Services initiated by the WMO World Climate Conference-3 in 2009. CM SAF is supporting climate services at national meteorological and hydrological services (NMHSs) with long-term data records but also with data sets produced close to real time that can be used to prepare monthly/annual updates of the state of the climate. Both types of products together allow for a consistent description of mean values, anomalies, variability and potential trends for the chosen ECVs. CM SAF ECV data sets also serve the improvement of climate models both at global and regional scale.

As an essential partner in the related international frameworks, in particular WMO SCOPE-CM (Sustained COordinated Processing of Environmental satellite data for Climate Monitoring), the CM SAF - together with the EUMETSAT Central Facility, assumes the role as main implementer of EUMETSAT’s commitments in support to global climate monitoring. This is achieved through:

- Application of highest standards and guidelines as lined out by GCOS for the satellite data processing,

- Processing of satellite data within a true international collaboration benefiting from developments at international level and pollinating the partnership with own ideas and standards,
- Intensive validation and improvement of the CM SAF climate data records,
- Taking a major role in data set assessments performed by research organisations such as WCRP. This role provides the CM SAF with deep contacts to research organizations that form a substantial user group for the CM SAF CDRs,
- Maintaining and providing an operational and sustained infrastructure that can serve the community within the transition of mature CDR products from the research community into operational environments.

A catalogue of all available CM SAF products is accessible via the CM SAF webpage, http://www.cmsaf.eu. Here, detailed information about product ordering, add-on tools, sample programs and documentation is provided.

2 Introduction to CLARA-A3 SAL, CLARA-A3 WAL and CLARA-A3 BAL

Surface albedo describes the fraction of all incident (solar shortwave) radiation which is reflected away from the surface being illuminated. It depends on the surface properties and the illumination conditions and is a key component in the treatment of Earth's surface energy budget and therefore significantly important for our planet's climate. Surface albedo has been designated as one of the Essential Climate Variables (ECV) of the Global Climate Observing System (GCOS), as required by Intergovernmental Panel on Climate Change (IPCC) and United Nations Framework Convention on Climate Change (UNFCCC) (GCOS Secretariat 2006). The directional-hemispherical reflectance, or black-sky albedo, is one way to estimate the surface albedo.

In this document the term surface albedo has the following three alternatives:

	TCDR	ICDR
Black-sky surface albedo from AVHRR-GAC	**CM-11222**	**CM-6221**
White-sky surface albedo from AVHRR-GAC	**CM-11223**	**CM-6223**
Blue-sky surface albedo from AVHRR-GAC	**CM-11224**	**CM-6224**

The physical definitions of these parameters are described in Sections 3.1.1, 3.1.2, and 3.1.3, respectively.

Global long-term monitoring of Earth's climate parameters, such as surface albedo, is best accomplished using satellite remote sensing instruments. The need for robust long-term datasets is answered by the Satellite Application Facility on Climate Monitoring (CM SAF) project through the CM SAF cLouds, ALbedo and Radiation (CLARA) dataset family. The basic principle of the CLARA dataset family is to utilize an intercalibrated Advanced Very High Resolution Radiometer (AVHRR) data record (Fundamental Climate Data Record, FCDR) to coherently provide datasets (Thematic Climate Data Record, TCDR) of cloud properties, surface radiation parameters and surface albedo almost four-decade length of AVHRR coverage. The surface albedo of the CLARA-A3 CDR is provided for cases without the atmosphere contribution (black-sky albedo, SAL), isotropic diffuse conditions (white-sky albedo, WAL) and varying cloud conditions (blue-sky albedo, BAL).

This document describes the algorithm basis, production system and uncertainty analysis of the surface albedo components of the CLARA-A3 dataset family. The full names of the surface albedo dataset are thus CLARA-A3 SAL, CLARA-A3 WAL and CLARA-A3 BAL (CLARA dataset, AVHRR 3rd release, black-sky Surface albedo; CLARA dataset, AVHRR 3rd release, White-sky surface albedo; CLARA dataset, AVHRR 3rd release, Blue-sky surface albedo). The CLARA-A3 SAL is an evolved version of the initial CLARA-A1 SAL black-sky albedo dataset (Riihelä et al., 2013), followed by CLARA-A2 SAL black-sky albedo dataset (Anttila et al., 2016) featuring improvements in the aerosol background treatment, periodically taking into account changes in land cover as observed by newer land cover maps, ocean wind impacts on ocean albedo, versatile statistical values and other more minor corrections and improvements in the algorithm.

The improvement of CLARA-A3 to CLARA-A2 are:

Improvement	**A2**	**A3**	**Details in:**
AVHRR Input data processing	PPS v2014 Patch 1	PPS v2021 based on the EUM AVHRR FDR	CLARA-A3 Cloud ATBD
	Land cover maps 1993 -2009	Land cover maps 1993 -2015	Table 3-5
	No distinction for desert areas in atmospheric correction	Atmospheric correction also desert specific	
Retrieval	Binary cloud mask	Cloud probability based cloud screening	3.7.2.1
	Black-sky surface albedo SAL	Black-sky surface albedo SAL White-sky surface albedo WAL Blue-sky surface albedo BAL	3.2
	Monthly and pentad means, standard deviations, medians, skewness, kurtosis	All A2 outputs available for SAL, also separately for snow and non-snow. WAL and BAL over snow available as temporal means only.	
Spatial/temporal extension	1982-2015	1979-2020	

3 CLARA-A3 SAL, WAL and BAL Algorithm Description

The algorithm description is organized as follows. To begin, we briefly introduce the principal inputs to the algorithm, followed by physical formulations of the three albedo quantities being estimated. We then provide a high-level overview of the processing necessary to generate the estimates from satellite data, accompanied by some background information justifying the choices made for the algorithm components. Then, we describe the level 2 (overpass) SAL processing step by step, and finally discuss the generation of the final WAL and BAL estimates during level 3 processing.

The main inputs of the CLARA-A3 SAL/WAL/BAL algorithm are as follows:

- Red and NIR channel TOA reflectances (AVHRR channels 1 & 2)
- Sun Zenith Angles (SZA)
- Viewing/Satellite Zenith angles (VZA)
- Relative Azimuth angles between Sun and the satellite / Separate Sun and Satellite Azimuth angles required for reliable topography correction computation
- Cloud probability for each AVHRR-GAC pixel
- Cloud identification and observed radiance quality data
- Land cover data
- Aerosol optical depth at 550 nm
- Atmospheric composition description data (water vapour content, ozone content, surface pressure)

3.1 Definitions of albedo quantities

3.1.1 SAL (Black-sky surface albedo)

The physical quantity that CLARA SAL describes is the black-sky broadband surface albedo, mathematically written as (Schaepman-Strub et al., 2006)

$$\alpha(\theta_s,\phi_s) = \int_0^{2\pi}\int_0^{\pi/2} \rho(\theta_s,\phi_s;\theta_v,\phi_v)\cos(\theta_v)\sin(\theta_v)d\theta_v d\phi_v \qquad (1)$$

The black-sky surface albedo is the integral of radiation reflected from a single incident direction (θ_s, ϕ_s) towards all viewing directions (θ_v, ϕ_v) in the zenithal and azimuthal planes, as described by the reflectance ρ. The angles are illustrated in Figure 3-1. The spectral dependency of albedo is omitted here; a full broadband albedo would be obtained by integrating the directional-hemispherical reflectance (black-sky albedo) over the waveband under investigation.

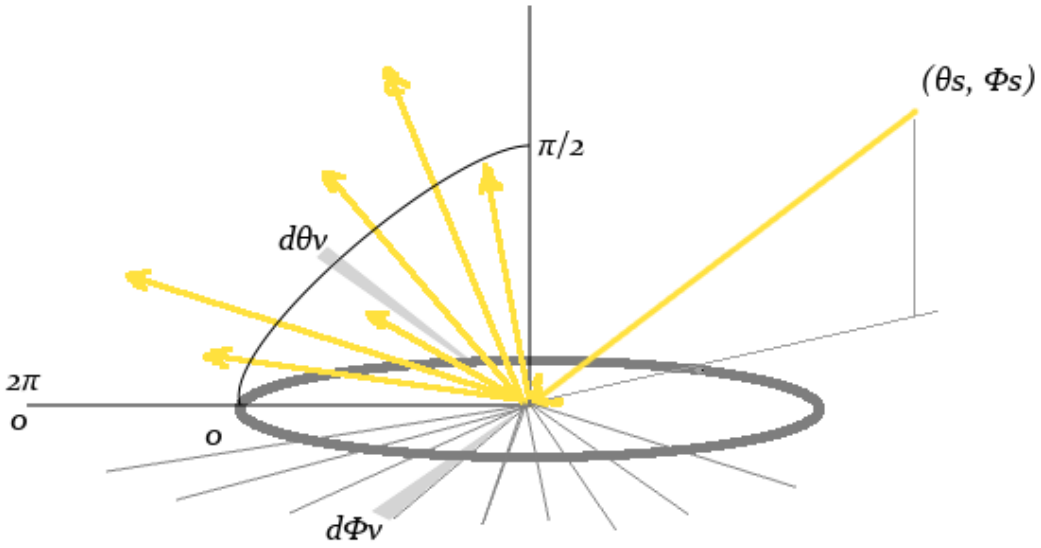

Figure 3-1: The geometry of the angles used in definition of the black-sky surface albedo (directional-hemispherical reflectance).

3.1.2 WAL (White-sky surface albedo)

The physical quantity that CLARA WAL describes is the white-sky broadband surface albedo, mathematically written as (Schaepman-Strub et al., 2006)

$$\alpha(2\pi, 2\pi) = \frac{1}{\pi}\int_0^{2\pi}\int_0^{\pi/2} \rho(\theta_s, \phi_s; 2\pi)\cos\theta_s \sin\theta_s \, d\theta_s d\phi_s \quad (2)$$

The white-sky surface albedo is the integral of radiation reflected from all incident directions (θ_s, ϕ_s) towards all viewing directions in the zenithal and azimuthal planes, as described by the reflectance ρ. The illumination is considered fully isotropic – this assumption is likely not fully valid directionally or spectrally in real-world conditions. The spectral dependency of albedo in the general sense is not considered in this equation; a full broadband albedo would be obtained by integrating the bihemispherical reflectance (white-sky albedo) over the waveband under investigation.

The white-sky albedo values are calculated per pixel for snow-free terrain for individual images and at monthly and pentad level for snow/ice pixels.

3.1.3 BAL (Blue-sky surface albedo)

The physical quantity that CLARA BAL describes is the blue-sky broadband surface albedo, mathematically written as (Schaepman-Strub et al., 2006)

$$\alpha(\theta_s, \phi_s, 2\pi) = f_{dir}\alpha(\theta_s, \phi_s) + (1 - f_{dir})\alpha(2\pi, 2\pi) \quad (3)$$

The blue-sky surface albedo is the weighted sum of the black-sky and white-sky albedo values, the weights being the fraction of the direct irradiance f_{dir} and the fraction of the diffuse irradiance (1-f_{dir}). The CLARA BAL is derived from the CLARA SAL and CLARA WAL values using the direct irradiance fraction (see section 3.7.2.3). Note that the representation of blue-sky albedo as a weighted sum of black/white-sky albedo involves an assumption of a fully isotropic diffuse illumination field, implying that increased retrieval uncertainty may manifest under e.g. heavy aerosol loading conditions (Román et al., 2010). However, under most atmospheric conditions, and particularly at SZA range of 55-60 degrees, the assumption is justified.

3.2 Overview of SAL, WAL, and BAL retrieval in CLARA-A3

A high-level overview of SAL/WAL/BAL processing in CLARA-A3 is illustrated below in Figure 3-2. SAL is computed first for all valid pixels in an AVHRR overpass, along with WAL for non-snow land surface pixels (Yang et al., 2008), with fraction of direct radiation calculated as input for the level 3 processing (section 3.7). During the level 3 processing, WAL is computed for snow-covered areas based on statistical relationships observed between white- and black-sky albedo observations (Manninen et al., 2019; Manninen et al., 2020). The blue-sky albedo component BAL is finally computed as a weighted mean of SAL and WAL, with the temporal mean of the fraction of direct radiation in the grid cell in question serving as the weight.

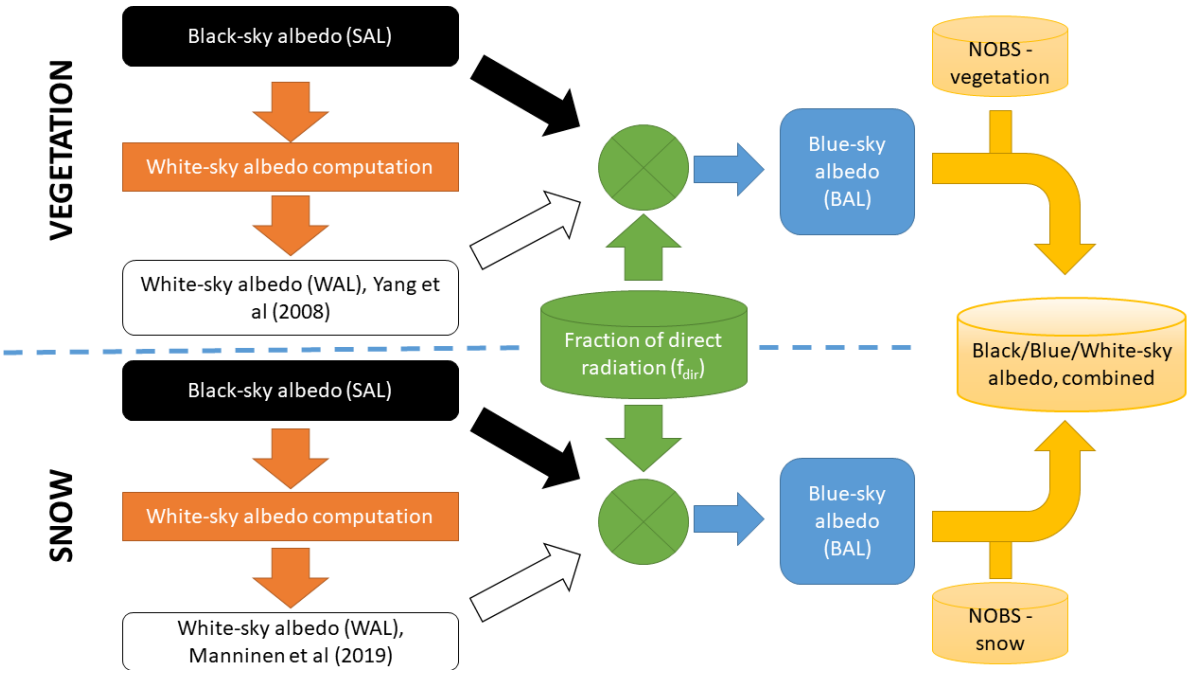

Figure 3-2: Relationships of the albedo quantities in CLARA-A3 SAL. NOBS refers to the amount of valid satellite observations of snow and/or vegetated conditions.

The definition of broadband albedo for SAL, WAL and BAL is the wavelength range of 0.25 - 2.5 µm, according to the narrow-to-broadband (NTBC) algorithms that ultimately determine the

range. The full solar spectrum extends further into infrared, but it should be kept in mind that the regions of 2.5 - 4 µm contribute as little as 0.03% to the total broadband albedo (van Leeuwen and Roujean 2002). AVHRR channels 1 and 2 (0.58-0.68 µm and 0.725-1 µm) are used for the CLARA SAL product generation as radiance sources.

The CLARA SAL, -WAL and -BAL data record spans the Earth completely from pole to pole, although no coverage exists during polar winters due to lack of solar illumination. The satellite observations are processed at the nominal Global Area Coverage (GAC) resolution (~5 km at nadir). During spatiotemporal aggregation (level 3 processing), the user-deliverable end products are formed with the spatial resolution of 0.25 degrees on the global grid, and 25 km on polar region grids (EASE-2 grid). One degree in latitude/longitude is approximately 111 km at the equator, although the relationship is very different close to the poles.

Temporal aggregation occurs on the pentad (5-day) and monthly mean levels of the SAL, WAL and BAL surface albedo estimates. In addition, the monthly and pentad standard deviation, skewness, kurtosis and median values are provided. The number of individual retrievals behind the monthly and pentad values are given as well as the monthly mean of the cosine of the solar zenith angle value of the satellite pixels. Also, snow-covered and snow-free albedo estimates are available separately, as well as their combination based on weighing by amounts of valid snow/snow-free observations.

SAL processing overview

To give a brief overview into SAL processing, it should first be noted that the process of deriving a broadband black-sky surface albedo product from satellite radiance observations is challenging. The radiation of the Sun must first propagate the Earth's atmosphere, then be scattered from the Earth's surface, and propagate the atmosphere again going up before it is observed by the satellite instruments. All of these factors influence the observed radiation and thereby they must be compensated for in the algorithm to ensure a non-biased retrieval of the black-sky surface albedo (see Figure 3-3 for a general outline of the SAL computation stages).

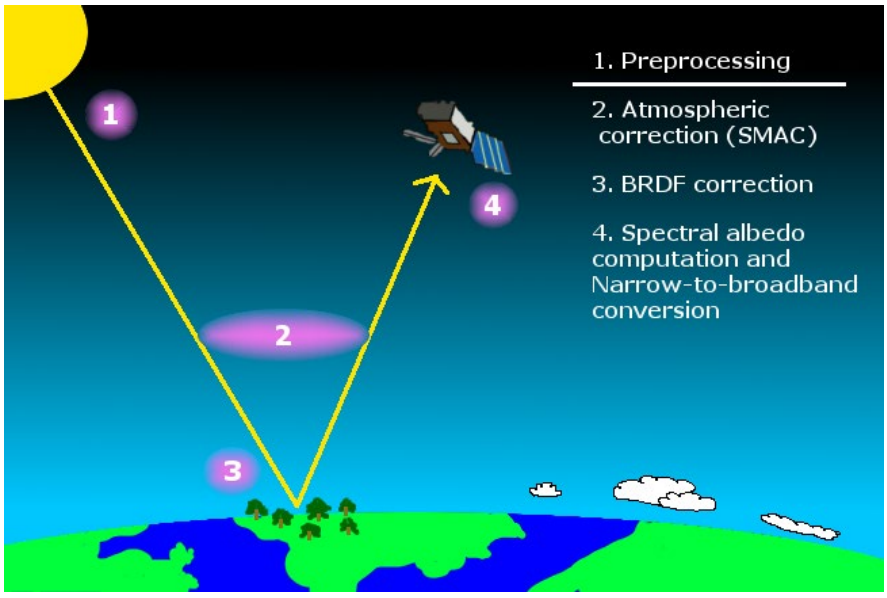

Figure 3-3: An illustration of the black-sky surface albedo product (SAL) computation phases.

The derivation of the directional-hemispherical reflectance (black-sky broadband surface albedo) from monodirectional radiances observed by a satellite in an orbit of 870 (NOAA) kilometers has several factors that need to be taken into account. The radiance observed by the satellite instrument represents only a single viewing and illumination geometry (Bidirectional Reflectance Distribution Function (*BRDF) problem*), the observed radiances are limited in wavelength by the instruments' spectral response (*spectral conversion problem*), and the radiances contain a contribution from the scattering mechanisms of the atmosphere between the instrument and the observed surface (*atmospheric problem*). The wavelength ranges of the radiation emission from the atmosphere can be neglected because the instrument channels used to derive the surface albedo are beyond the thermal emission wavelengths. In addition, many pixels are partly or completely covered by clouds. The reflectance properties of most clouds also resemble snow quite closely. Both of these issues must be solved to exempt the cloud-contaminated pixels from the computation and to identify cloud-free snow and sea ice pixels for later computation (*Cloud detection/masking problem*).

On process flow terms, the algorithm at the overpass level is set up as shown in Figure 3-4. Details concerning user messaging, error detection and other details have been omitted from the figure for clarity. The main processing steps in deriving the broadband surface albedo product from observed satellite radiances are as follows:

1. The radiances are converted into pixelwise Top-of-atmosphere (TOA) reflectances. This preprocessing step is handled by the Polar Platform System (PPS v2021 for CLARA-A3) software package. The PPS output contains both a binary cloud mask and cloud probability values. Processing is attempted only for land and snow/sea ice pixels for which the cloud probability is smaller than 20%. The cloud mask includes separate classes for snow covered pixels and they are used for snow covered area determination.
2. The classification of snow covered pixels in Arctic and Antarctic sea areas provided by PPS are verified by using Ocean and Sea Ice Satellite Application Facility (OSI-SAF) sea ice extent data.
3. The open water albedo is determined on the basis of the sun zenith angle and the surface wind data using the algorithm by Jin et al. (2004 and 2011).
4. For land pixels a topography related radiometric and geolocation correction is performed. The correction implementation is described in sections 3.3.1 and Appendix A.
5. The pixels that are not covered by snow are given a land use information using land use classification data. This process is described in more detail in 3.3.2.
6. The TOA reflectances of pixels of land surfaces are reduced to surface reflectances by removing the atmospheric effects with a correction based on the Simplified method for the atmospheric correction of satellite measurements in the solar spectrum (SMAC) algorithm (Rahman and Dedieu 1994). See section 3.3.2 for details.
7. The surface reflectances of pixels on land and not covered by snow are expanded into hemispherical spectral albedos by applying a BRDF algorithm based on the work of Roujean et al. (1992) and Wu et al. (1995). The BRDF algorithm is applied to both 0.6 and 0.8 μm channel separately. Details in section 3.3.3. For pixels classified as being covered by snow, the correction for BRDF effects is handled at the weekly and monthly level by a temporal averaging of the various directional reflectances derived as the observed product (Riihelä et al., 2010). Thus, over- or underestimations of the mean pentad/monthly snow albedo will occur in the observed CLARA SAL images.
8. The spectral albedos are processed to a shortwave broadband black-sky albedo via a narrow-to-broadband (NTB) conversion (details in section 3.6). The conversion is both instrument and pixel land cover specific. The land cover information comes from four different land use classification (LUC) datasets. The NTBC algorithm is chosen as follows:

- For water pixels, SAL is derived using the algorithm after Jin et al. (2011).
- For snow pixels, the observed BB directional reflectance is computed from the spectral directional reflectance (see above) by a NTBC algorithm by Xiong et al. (2002).
- For other types of land cover, the NTBC conversion is based on Liang (2000).

9. Sun Zenith Angle normalization was not included in this release for technical reasons and to preserve coherency between land and snow albedo retrievals. Its effect is considered a part of the retrieval uncertainty of the pentad/monthly mean products.

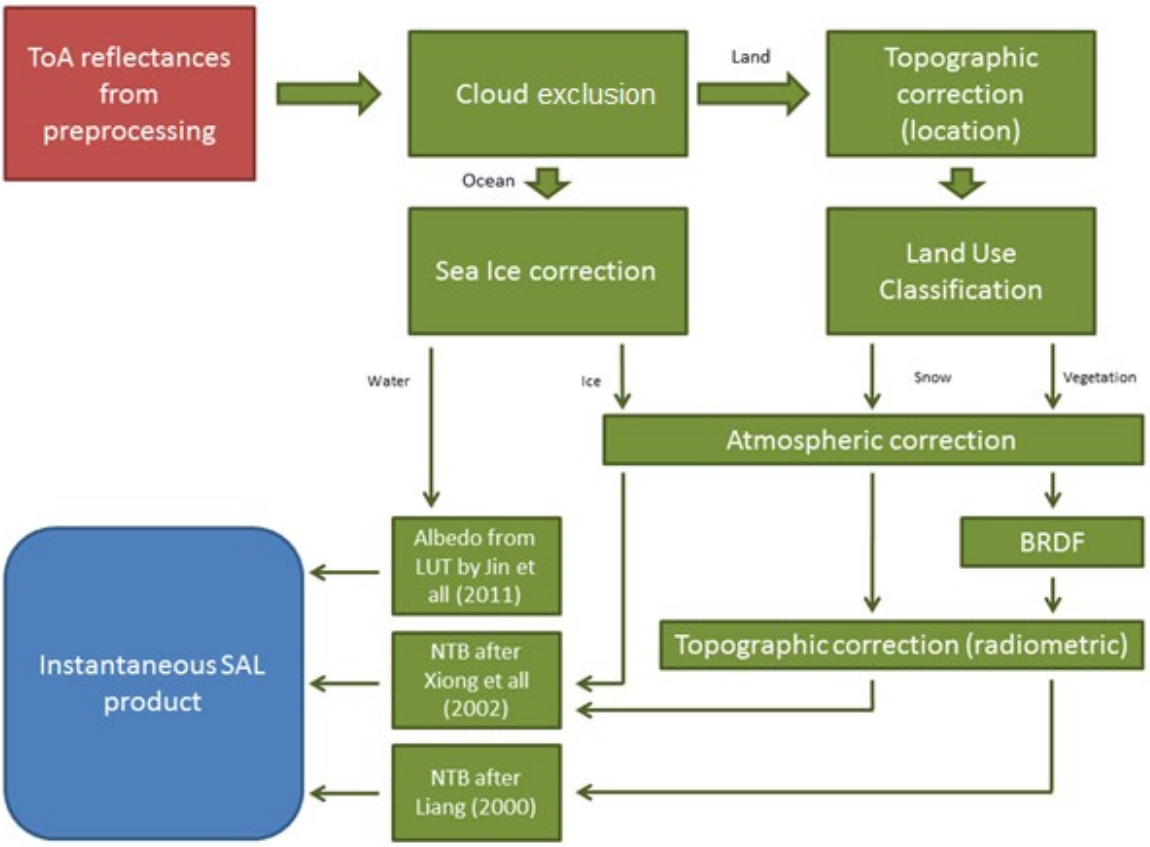

Figure 3-4: Level 2 processing flow in CLARA-A3 SAL.

WAL processing overview

Since optical satellite instruments don't observe the white-sky albedo, it has to be estimated on the basis of the black-sky albedo. In the MODIS MCD43 albedo retrievals, the approach is to estimate the weights of different scattering processes in available clear-sky observations, and then to use these weights to estimate white-sky albedo. For CLARA, the direct integration of (the available) black-sky albedo over the solar zenith angle and the azimuth angle (Eq. 2) is not advisable, because of issues related to grazing angle scattering. Although the irradiance coming from the solar zenith angles larger than 80° is only 3% of the total amount, its effect on scattering may be larger than that. On the other hand, integration of an empirical fit to the black-sky albedo dependence of the solar zenith angle would be highly prone to numerical

errors, as the sun has never nadir view outside the tropics and in closer to the poles the solar zenith angle range covered is very small. Thus, empirical relationships between the black-sky and white-sky albedo are used (Figure 3-2) for: 1) snow-free land (Yang et al., 2008), 2) snow-covered open land (Manninen et al., 2019) and 3) forests with snow cover (Manninen et al., 2019). The first relationship is parametrized with the solar zenith angle and the latter two depend on the monthly solar zenith angle and black-sky albedo statistics and they are derived only as monthly and pentad averages. The reason that the white-sky albedo of a forested area can't be treated as a weighted average of the white-sky albedos of snow and forest is that neglecting the multiple scattering between the canopy and the snow of the forest floor could result in an error of 20% (Jääskeläinen and Manninen, 2021).

BAL processing overview

The blue-sky albedo is derived as a weighted average of the black and white-sky albedos (Eq. 3, Figure 3-2), the weights being the fraction of the direct irradiance (= 1 – fraction of diffuse irradiance). For satellite products the diffuse irradiance is assumed to be completely isotropic (Lucht et al., 2000), although subpixel cloudlets certainly cause anisotropy both spatially and spectrally. According to simulations by Pinty et al., (2005), the isotropic blue-sky albedo may differ up to 8% from the true one, depending on the AOD. As the albedo products are defined to be broadband versions, also the direct/diffuse irradiance is derived for blue-sky retrieval only for broadband, not spectrally.

3.3 Calculating SAL over land areas

3.3.1 Topography correction

The topography affects the satellite image most significantly in two ways (Manninen et al., 2011): 1) the altitude difference with respect to sea level will cause the geolocation of the pixel to be shifted and 2) the inclination of the slopes of the terrain within a pixel will alter its reflectance value. As the BRDF calculations are based on a horizontal plane assumption, erroneous values will be obtained for inclined slopes. In addition, the slope distribution of the terrain covered by the pixel may contain slopes that are not seen at all by the sun or the satellite. These kinds of situations will cause even larger errors than small slope inclinations. Multiple reflections from slope to slope would be a second order effect affecting the observable reflectance. However, since the first order correction already involves CPU-intensive calculations, the second order effect is not studied here at all.

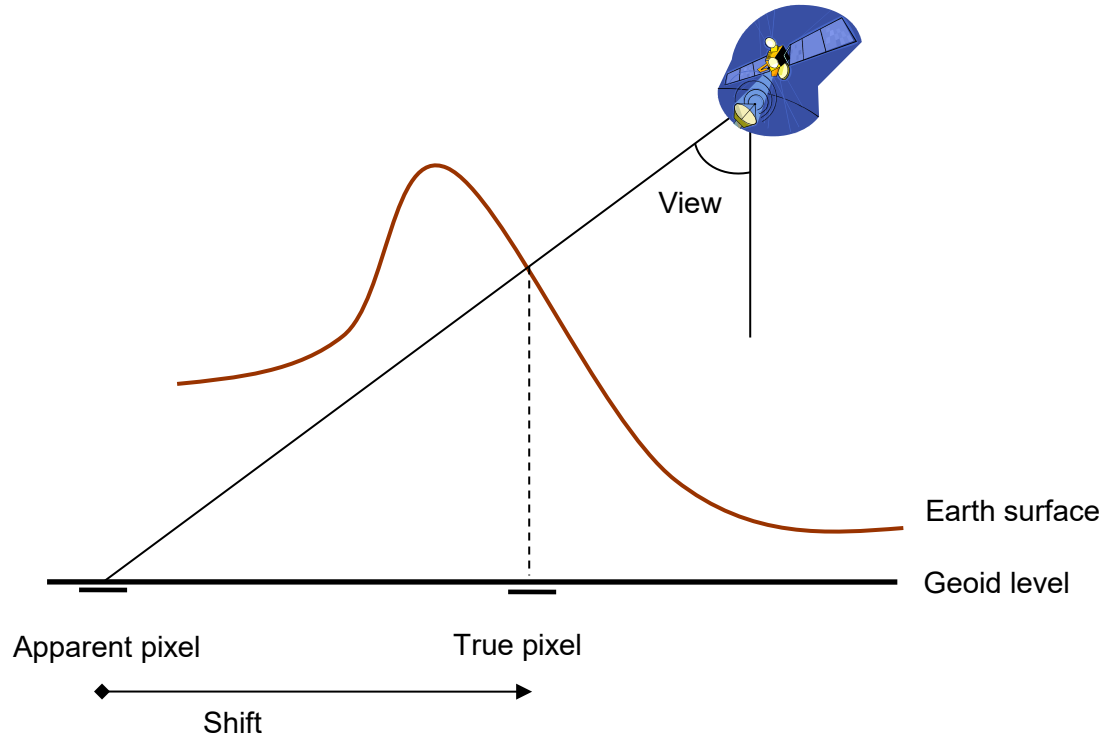

Figure 3-5: Location difference between apparent and true pixel locations.

The geolocation shift is corrected using latitude/longitude coordinates that the PPS software provides for each image pixel. These co-ordinates have been computed from satellite attitude data without any information of the terrain altitude, and are thus not accurate for elevated areas at higher view angles. A true elevation of 3000 meters causes a pixel shift of 2500 m when the viewing angle is 40 degrees. Thus the effect can be significant. Figure 3-5 shows how the digital elevation model (DEM) is used for computing the true pixel location from the apparent one. Initial pixel coordinates refer to locations on the geoid surface. Computing true locations shift pixels closer to the nadir on elevated areas, but some pixels may be left in shade. Pixel dimensions also change on tilted areas. The CLARA SAL uses Global 30 Arc-Second Elevation (GTOPO30) digital elevation model to correct the pixel location.

The correction of topographic effect on the reflectance values is based on calculating slope and aspect angle distributions for each satellite pixel and correcting the bidirectional reflectance distribution function (BRDF) using local incidence angles instead of the global ones. Calculations are mainly based on a higher resolution NASA's Shuttle Radar Topography Mission (SRTM) DEM. Outside its coverage (i.e. polar areas north/south of the latitude 60°N/60°S) the GTOPO30 DEM (USGS – doi:10.5066/F7DF6PQS) is used. The slope information is used to calculate the distributions of different slope angles and inclinations. The effect of slope angles is different for different land use types. Therefore the information on distribution of slope angles is combined with the land use information. The effect of the topography correction on BRDF will be discussed in more detail in Appendix A.

The calculation of topography effects requires for full illumination-viewing geometry data to be available. To accommodate this need, the PPS preprocessing package provides CLARA SAL

with all relevant angular data: satellite zenith angles, Sun zenith angles, satellite azimuth angles, and Sun azimuth angles.

3.3.2 Atmospheric correction

The atmosphere affects the ground reflectivity observed by the satellite. For black-sky surface albedo calculations, this effect must be removed. The algorithm chosen to perform this is the Simplified Method for Atmospheric Corrections (SMAC) (Rahman and Dedieu 1994). The algorithm uses the following input for each pixel:

- TOA reflectance, *from PPS pre-processing output*
- Surface pressure, *from ECMWF ERA5 data [hPa]*
- Ozone content, *from ECMWF ERA5 data [atm-cm]*
- Aerosol optical depth (AOD) at 550 nm, *calculated from Total Ozone Mapping Spectrometer (TOMS) and Ozone monitoring instrument (OMI) aerosol index* (AI)
- Total column water vapour content, *from ECMWF ERA5 data* $[\frac{g}{cm^2}]$
- Differential sun-satellite azimuth angle

The algorithm is based originally on the 5S radiative transfer code (Tanré et al., 1990), but later fitted against the more recent 6S radiative transfer model code (Vermote et al., 1997), aiming for simplified calculations to greatly enhance computation speed. The main simplification is the treatment of the various atmospheric radiative components (e.g. Rayleigh scattering) by analytic terms, which are sensor- and waveband-specific. The data volumes processed to derive the distributable CM SAF CLARA SAL products are large, and therefore speed is essential. The aerosol optical depth is calculated using aerosol index data from TOMS and OMI instruments.

The atmosphere behaves differently in extremely dry conditions with high aerosol content than in so called normal conditions. Therefore, the SMAC algorithm provides the option of computing the correction separately for desert areas. In CLARA-A3, computations over barren and desert land cover will select the desert-specific numeric SMAC coefficients for processing.

The SMAC algorithm is based on an inverse solution to the following atmospheric absorption/scattering equation (Rahman and Dedieu 1994, eq. 2)

$$\rho_{TOA}(\theta_s, \theta_v, \Delta\varphi) = t_g(\theta_s, \theta_v)\left\{\rho_a(\theta_s, \theta_v, \Delta\varphi) + \frac{T(\theta_s)T(\theta_v)\rho(\theta_s,\theta_v,\Delta\varphi)}{1-\rho(\theta_s,\theta_v,\Delta\varphi)S}\right\} \quad (4)$$

We solve the surface reflectance from the equations above as follows:

$$\rho(\theta_s, \theta_v, \Delta\varphi) = \frac{\rho_{TOA} - t_g \rho_a(\theta_s, \theta_v, \Delta\varphi)}{t_g T(\theta_s) T(\theta_v) + S\rho_{TOA} - t_g \rho_a(\theta_s, \theta_v, \Delta\varphi) S} \quad (5)$$

where

ρ_{TOA} = reflectance at the top of the atmosphere

t_g = total gaseous transmission (both upward and downward paths)

ρ_a = atmospheric reflectance, a function of the optical properties of air molecules and aerosols as well as the illumination/viewing geometry, contribution from photons that have not interacted with the surface but only the atmosphere

$T(\theta_s)$ = atmospheric (scattering) transmission (downward)

$T(\theta_v)$ = atmospheric (scattering) transmission (upward)

S = spherical albedo of the atmosphere as viewed from the ground (corresponding to photons 'trapped' in successive ground-atmosphere scatterings)

Figure 3-6 further illustrates the origin of the terms in equation 6. Surface reflection contributes through both direct and diffuse incident radiation. Adjacency effects are omitted, i.e. the surface is assumed homogeneous at the imaged footprint scale.

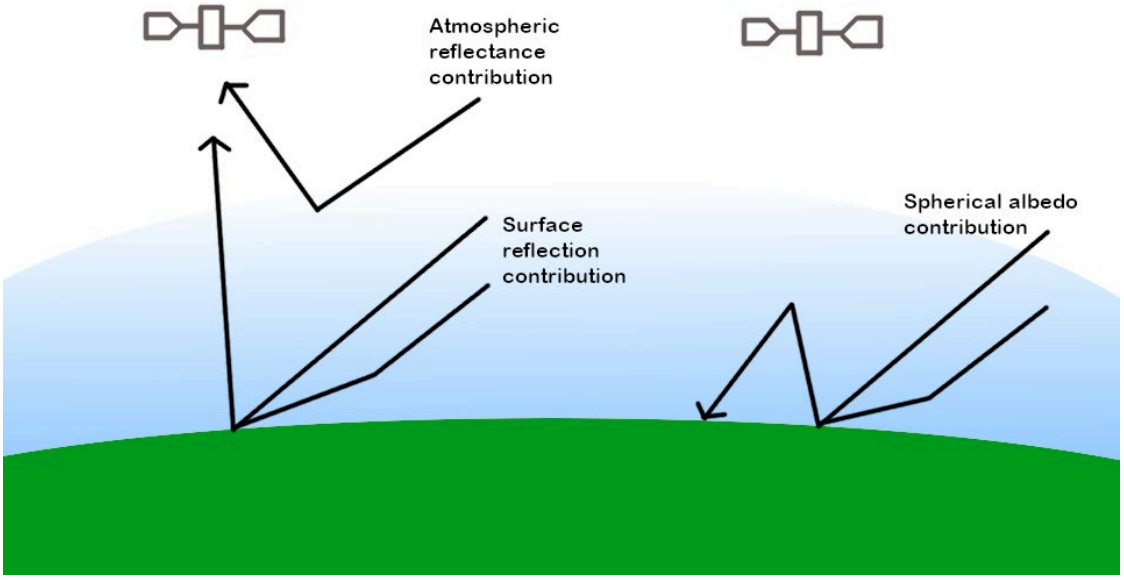

Figure 3-6: Illustration of contributions to the atmospheric correction equation. After Tanré, 1990.

The gaseous transmission term is

$$t_g = \prod e^{a(mU)^n} \quad (6)$$

where *a* and *n* are predefined constants (but different for each gas), *U* is the vertically integrated absorber amount and *m* is the airmass, which is defined as

$$m = \frac{1}{\cos\theta_s} + \frac{1}{\cos\theta_v} \quad (7)$$

The transmission is calculated separately for ozone, water vapour, oxygen, carbon dioxide, methane, nitrogen dioxide, and carbon monoxide. Total gaseous transmission in eq. 6 is the multiplication of all these components. All constants in the calculations are available from the CESBIO website, http://www.cesbio.ups-tlse.fr/us/serveurs4.htm.

The atmospheric reflectance ρ_a is

$$\rho_a = \rho_{ar} + \rho_{ap} - R_{ar} - R_{ap} - R_{6s} \quad (8)$$

where ρ_{ar} is the Rayleigh atmospheric reflectance, ρ_{ap} is the aerosol atmospheric reflectance, R_{ar}, R_{ap} and R_{6S} are the Rayleigh residual, the aerosol residual and 6S residual, respectively. (In other words, the total atmospheric reflectance is a sum of the atmospheric reflectances resulting from Rayleigh and aerosol scattering processes. The sum is then corrected by a substraction of residuals to account for numerical inaccuracies resulting from the simplification against the full radiative transfer model.)

The Rayleigh atmospheric reflectance is defined as

$$\rho_{ar} = \frac{\tau_r p_r(\xi)}{4\cos(\theta_s)\cos(\theta_v)} \quad (9)$$

The molecular optical depth τ_r is a predefined constant, but it is corrected for surface pressure variations by

$$\tau_r(P) = \tau_r(P_0)\frac{P}{P_0} \quad (10)$$

where *P* is surface pressure and P_0 = 1013 mbar.

The molecular phase scattering function

$$p_r(\xi) = 0.7190443(1+\cos^2(\xi)) + 0.0412742 \tag{11}$$

is calculated assuming a molecular depolarisation factor δ=0.0139 and where the scattering angle cosine is calculated by

$$\cos(\xi) = -(\cos(\theta_s)\cos(\theta_v) + \sqrt{(1-\cos^2(\theta_s))(1-\cos^2(\theta_v))}\cos(\Delta\varphi)) \tag{12}$$

The aerosol atmospheric reflectance requires more complicated calculations. To condense the equations, we first define $\mu_s=\cos(\theta_s)$,$\mu_v=\cos(\theta_v)$, $\kappa^2 = (1-\omega_0)(3-\omega_0\beta_1)$ and $\beta_1 = 3g$, where ω_0 is the single scattering albedo of the aerosol loading in the atmosphere and g is the asymmetry factor. Both are band-averaged, pre-defined constants loaded from SMAC coefficient file. The aerosol atmospheric reflectance is

$$\rho_{ap} = \frac{1}{\mu_s\mu_v}\left\{\begin{array}{l} \frac{X\mu_v}{1+\kappa\mu_v}(1-e^{\frac{-\tau_p(1+\kappa\mu_v)}{\mu_v}}) + \frac{Y\mu_v}{1+\kappa\mu_v}(1-e^{\frac{-\tau_p(1+\kappa\mu_v)}{\mu_v}}) \\ +(Z+P(\xi))\frac{\mu_s\mu_v}{\mu_s+\mu_v}(1-e^{-\tau_p(\frac{1}{\mu_s}+\frac{1}{\mu_v})}) \end{array}\right\} \tag{13}$$

where the coefficients *X*, *Y*, and *Z* are complicated numerical functions of the asymmetry factor, single scattering albedo, and the viewing geometry. The calculations are listed in Appendix B.

The average aerosol optical depth (for both AVHRR spectral bands) is calculated from the aerosol optical depth at 550nm (input) by

$$\tau_p = a_0 + a_1\tau_{550} \tag{14}$$

where a_0 and a_1 are predefined constants.

The residuals are calculated as follows. Firstly the Rayleigh residual is

$$R_{ar} = rr1 + \frac{rr2 * p_r(\xi) * ta * \frac{P}{P_0}}{\mu_s\mu_v + rr3 * \left(\frac{(ta * \frac{P}{P_0} * p_r(\xi))}{\mu_s\mu_v}\right)^2} \tag{15}$$

where *rr1*, *rr2*, *rr3* and *ta* are predefined constants from the SMAC coefficient file.

The aerosol residual is

$$R_{ap} = ra1 + ra2*(\tau_p * m * \cos(\xi)) + ra3*(\tau_p * m * \cos(\xi))^2 + ra4*(\tau_p * m * \cos(\xi))^3 \quad (16)$$

where *ra1*,*ra2*,*ra3* and *ra4* are predefined constants from the SMAC coefficient file and *m* is airmass factor, defined in eq. 7.

Finally, the 6S residual is

$$R_{6S} = rs1 + rs2*((\tau_p + ta*\frac{P}{P_o})*m*\cos(\xi)) + rs3*((\tau_p + ta*\frac{P}{P_o})*m*\cos(\xi))^2 + rs4*((\tau_p + ta*\frac{P}{P_o})*m*\cos(\xi))^3 \quad (17)$$

where *rs1*, *rs2*, *rs3*, *rs4* and *ta* are predefined constants from the SMAC coefficient file.

The atmospheric transmission terms *T* are defined as

$$T(\theta_x) = a_0 + \frac{a_1\tau_{550}}{\cos(\theta_x)} + \frac{a_2}{1+\cos(\theta_x)} \quad (18)$$

where the *a*-coefficients are predefined in the SMAC coefficient file.

The last term in the atmospheric correction is the spherical albedo of the atmosphere, given by

$$S = 1 - \frac{1}{(b_0 + b_1\tau_{550})} \quad (19)$$

where b_0 and b_1 are predefined constants from the SMAC coefficient file.

Finally, it should be mentioned that the aforementioned method assumes that the corrected area is large enough for neighboring area effects on the correction to be negligible. According to Rahman and Dedieu (1994), 1km pixel size is sufficient for this. The GAC pixel is much larger than this and therefore this assumption appears valid.

The output of the SMAC algorithm is surface reflectances.

3.3.2.1 Aerosol optical depth time series

In CLARA-A3, a daily AOD time series was constructed for the time frame 1979-2020 (Jääskeläinen et al., 2017). Because no AOD data set at wavelength 550 nm (needed by

SMAC) is available for the whole time range, the needed AOD is calculated from the TOMS and OMI Aerosol Index (AI) data, which cover almost the whole time range. The AI used here is measured in UV wavelength.

The AI is defined as

$$AI = -100 \cdot \left\{ \log_{10}\left[\left(\frac{I_{\lambda_1}}{I_{\lambda_2}}\right)_M\right] - \log_{10}\left[\left(\frac{I_{\lambda_1}}{I_{\lambda_2}}\right)_C\right]\right\} \quad (20)$$

where $I_{\lambda 1M}$and $I_{\lambda 2M}$are the radiances measured by instrument M at wavelengths $\lambda 1$ and $\lambda 2$ and $I_{\lambda 1C}$and $I_{\lambda 2C}$are the calculated radiances, which are produced by the radiative transfer model for pure Rayleigh atmosphere (Herman et al. 1997, Torres et al. 1998).

The relation between the AOD at UV range and 550 nm has been studied using the AOD values at UV wavelength range retrieved from OMI observations. The AOD at 550 nm is derived using the equation:

$$\tau_{550} = \tau_{UV}\left(\frac{550}{\lambda_{UV}}\right)^{-\alpha} \quad (21)$$

where τ_{550} is the AOD at 550 nm, τ_{UV} is the AOD at UV range (retrieved from OMI measurements), λ_{UV} is the wavelength of the retrieved AOD and α is the Ångström exponent, which is calculated as

$$\alpha = \frac{\log\left(\frac{\tau_{\lambda 1}}{\tau_{\lambda 2}}\right)}{\log\left(\frac{\lambda 1}{\lambda 2}\right)} \quad (22)$$

where $\tau_{\lambda 1}$ and $\tau_{\lambda 2}$ are the retrieved AOD values at wavelengths $\lambda 1$ and $\lambda 2$ (Ångström, 1929).

The AOD time series has been constructed by studying the relation between AI and AOD (derived from OMI) in the years 2005-2008, during which period there is both AI and calculated AOD at 550 nm available. The information on Sun zenith angle (SZA) is included in the conversion to increase accuracy. In this version of AOD, the SZA is calculated by using the knowledge of measuring time and place. The data has been divided to 65 areas based on the AVHRR land use classification data and local locations of LUC areas (see an example in Figure 3-7). The coastline resolution is improved using the GLC2000 data.

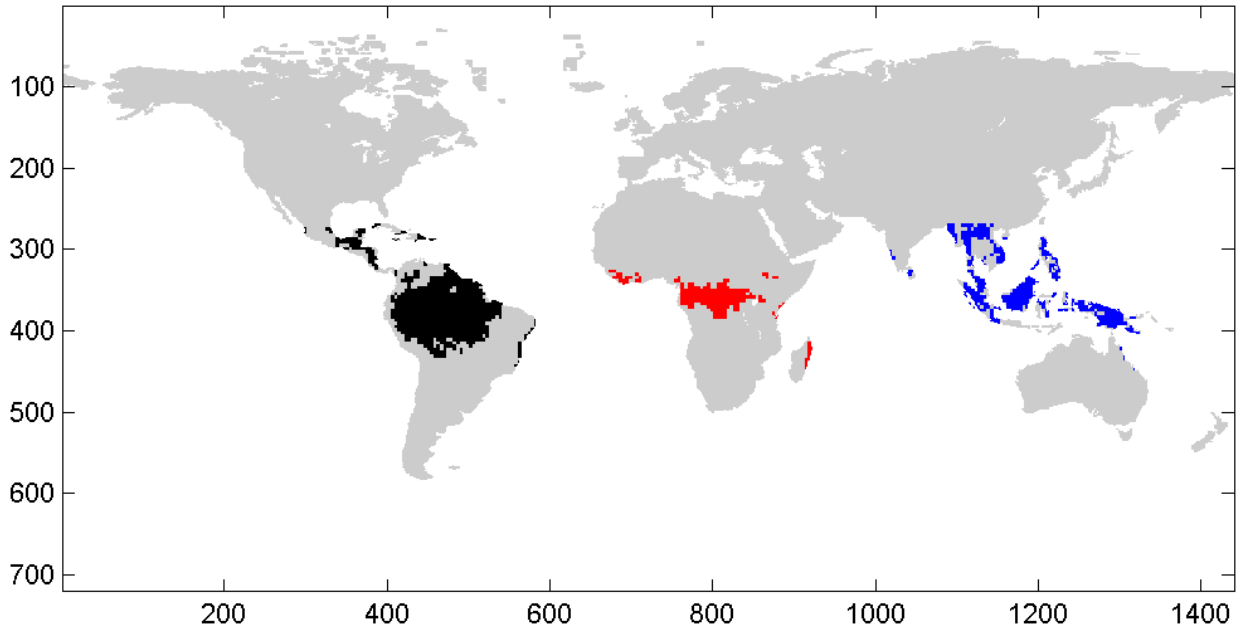

Figure 3-7: Example of data division using the AVHRR LUC data. The coloured areas (black, red and blue) have all the land use classification value 1 (Broadleaf Evergreen Forest). Based on the location the land use class is divided into 3 areas (marked by the different colors), which are handled separately in processing the AOD time series.

To keep the AOD time series homogeneous, only positive OMI-AI values are used in calculations. First the data needs to be deseasonalized. For OMI AI and AOD this is done by using OMI data for 2005-2008. Deseasonalization removes the annual variation from the data making it easier to use.

After the deseasonalization, the regression of the data ($AOD = \alpha \cdot AI \cdot cos(SZA) + \gamma$) is done separately for the different areas (65 areas). The data used in deriving the regression parameters to be applied in generating the AOD time series is screened to minimize possible errors. Since AI can be calculated also for cloudy conditions (in which case it shows small positive values), these cases are excluded using MODIS-AOD at 550 nm by verifying that the values are close enough to the values of OMI AOD at 550 nm (< 20% relative errors approved). In addition, only the AI values which fall in the range [0.5, 4.5] of the total variation are used. Since SMAC cannot be applied to AOD values higher than 1, the regression is made only for AI and SZA values which correspond to the AOD values below 1. The regression itself is quite linear: the higher the absolute value of the AI is, the higher the AOD is.

While constructing the AOD time series, to achieve a larger global coverage, the AI data is not screened as much as for the regression. Only the highest and lowest values are omitted. Even though the AI values can be measured for cloudy conditions, the screening for clouds was not implemented in the time series construction. This is because the cloudy pixels are excluded from the SAL calculation by the cloud mask.

The data is gathered into global daily maps (see example in Figure 3-8). The possible gaps in these maps are filled by using weighted mean to the whole map.

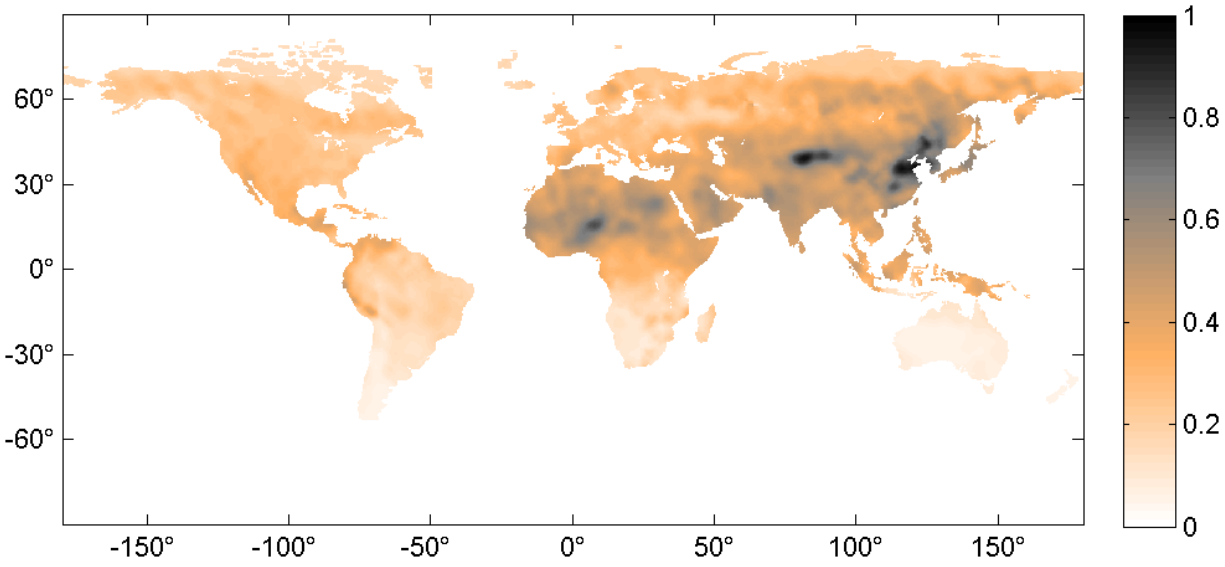

Figure 3-8: An example of calculated OMI-AOD on 1st of May 2005.

TOMS AI has only positive values and the spatial resolution of the data is coarser than for OMI (1° x 1.25°, OMI pixel being 0.25° x 0.25°). The two datasets are made coherent by dividing TOMS pixels into smaller ones and hence fitting the daily TOMS AI maps to the same grid as the daily OMI maps. This way also the constructed relation can be used and the assumed area division in the regression goes right. There is almost a three year gap in TOMS data (7th of May 1993 – 21th of July 1996). This gap has been filled using the data of the same pixel before and after the gap, also taking into consideration the time. Moreover, the TOMS instrument has a calibration problem (Kiss et al. 2007) affecting the data from the year 2000 onwards, most evidently from 2002 onwards. Hence the data from 2002 to 2004 is also discarded and this gap is filled the same way as the previous one.

The AOD time series is not applied for sea ice, ice sheets or water. For these areas the constant value of 0. is used (minor change from A2 value of 0.1 to better match observations over Polar regions).

Note: The AOD data for the years 2015-2020 was produced separately after the actual AOD time series and is a climatology of the AOD time series years 2005-2014. The extra years have not been validated. The climatology is also used in ICDR production.

3.3.3 BRDF

The satellite instruments measure radiances that are calibrated into TOA reflectances. If the effect of atmosphere, including clouds, is removed, the measures are estimates of ***bidirectional surface reflectance*** which represent only the viewing and illumination geometry at the moment of imaging. To expand the surface reflectance into spectral (hemispherical) albedo, a method is needed to describe the behavior of the reflectance with different viewing and illumination geometries. This is often referred to as an *anisotropy correction*. If the surface

reflected equally to all directions, this correction would not be necessary. However, all natural surfaces have some degree of anisotropy.

To account for the anisotropy, a mathematical relation capable of explaining the reflectance dependence on viewing and illumination angles is needed. This relation is called the Bidirectional Reflectance Distribution Function (BRDF), and its modelling and use have been widely discussed in literature. The term was first introduced by Nicodemus (1970), who defined the angular dependence of reflectance (i.e. BRDF) mathematically as

$$\rho(\theta_s,\varphi_s;\theta_v,\varphi_v)=\frac{dL_v(\theta_v,\varphi_v)}{dE_s(\theta_s,\varphi_s)} \tag{23}$$

where dL_v is the (differential) radiance reflected by the object in the direction specified by the zenithal reflection angle (θ_v) and azimuthal reflection angle (φ_v), dE_s is the (differential) irradiance received by the object from the radiation source in the direction specified by its zenithal incidence angle (θ_s) and azimuthal incidence angle(φ_s). The geometries are further illustrated in Figure 3-9.

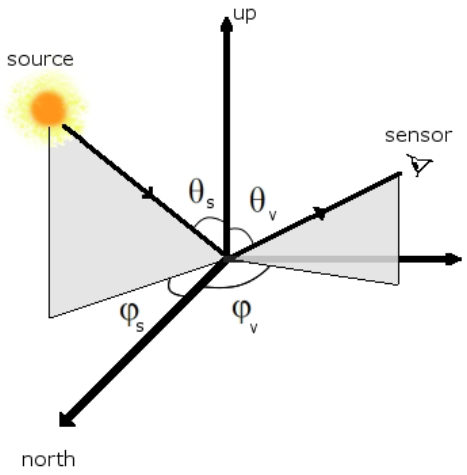

Figure 3-9: The BRDF geometry and relevant angles. For all non-isotropic objects, the reflectance changes as the illumination (subscript s) and viewing (subscript v) angles for elevation and azimuth change.

There are a large number of different BRDF models in existence. The most popular ones for remote sensing applications are the so-called kernel models, named after the fact that they model the reflectance of any surface type as a combination of isotropical, volume and geometrical scattering contributions (or kernels). In general terms the kernel reflectance models can be described as in Roujean et al. (1992) and Wu et al. (1995) by:

$$\rho=k_0+k_1f_1(\theta_s,\theta_v,\varphi)+k_2f_2(\theta_s,\theta_v,\varphi) \tag{24}$$

where the angles are as defined above, subscript 0 denotes nadir reflectance, subscript 1 denotes geometrical scattering term, and subscript 2 denotes volume scattering term. The model is valid for the waveband over which its kernels are defined. The *k* terms are the geometric and volume scattering kernels, and the *f* terms are their associated viewing and illumination angle dependency functions. Conceptually, geometric scattering results from discrete, opaque scatterers on the ground (and their shadowing effects), whereas volume scattering results from a collection of randomly dispersed facets of canopies and bare soils.

The BRDF needs to be calculable entirely from satellite observations and *a priori* known auxiliary data to be useful for the computation of CLARA SAL. A different approach has been chosen for non-snow-covered surfaces, snow-covered surfaces and large water bodies.

The BRDF of non-snow covered surfaces is incorporated in the product using a model developed by Wu et al. (1995). It uses normalized difference vegetation index (NDVI) as the parameter describing vegetation canopy physiology (through the *K* coefficients), and three angular parameters $\theta_s, \theta_v, \varphi$ as shown in eq. 24. It is based on the BRDF model by Roujean et al. (1992), and therefore works with a geometric approach to scattering modeling. The original model was modified with fits to AVHRR data to allow the usage of NDVI and to account for seasonal phenologically induced BRDF variation. The model coefficients (kernels) were derived separately for specific land cover types. Therefore the model may be called semi-empirical.

Wu's equations give the anisotropy factor Ω from eq. 24 (the BRDF relative to the nadir reflectance)

$$\Omega_i(\theta_s,\theta_v,\varphi) = \frac{\rho_i(\theta_s,\theta_v,\varphi)}{k_0} = 1 + a_{1i} f_1(\theta_s,\theta_v,\varphi) + a_{2i} f_2(\theta_s,\theta_v,\varphi) \tag{25}$$

The first term on the right is 1 because the nadir reflectance $\rho_i(0,0,\varphi) = k_0$ (Wu et al. 1995). Therefore the other kernels are $a_{1i} = k_1 / k_0$ and $a_{2i} = k_2 / k_0$. The subindex i is either 1 or 2, representing the AVHRR channels 1 (red) or 2 (nir) for which this model was developed for, meaning that

$$\Omega_{RED} = 1 + a_{11} f_1 + a_{21} f_2 \tag{26}$$

$$\Omega_{NIR} = 1 + a_{12} f_1 + a_{22} f_2 \tag{27}$$

where

$$f_1 = \frac{1}{2\pi} * [(\pi - \varphi) * cos(\varphi) + sin(\varphi)] * tan(\theta_s) * tan(\theta_v) - \frac{1}{\pi} * \left(tan(\theta_s) + tan(\theta_v) + \sqrt{tan(\theta_s)^2 + tan(\theta_v)^2 - 2 * tan(\theta_s) * tan(\theta_v) * cos(\varphi)} \right) \quad (28)$$

and

$$f_2 = \frac{4}{3\pi(cos(\theta_s) + cos(\theta_v))} \left[\left(\frac{\pi}{2} - \xi \right) cos(\xi) + sin(\xi) \right] - \frac{1}{3} \quad (29)$$

$$\xi = cos(\theta_s)cos(\theta_v) + sin(\theta_s)sin(\theta_v)cos(\varphi) \quad (30)$$

The angles $\theta_s, \theta_v, \varphi$ are the satellite image's sun zenith, viewing zenith and relative azimuth angles, respectively. The function dependencies have been omitted here for clarity. Overall, the normalized surface reflectances depend on the sun and viewing zenith angles, the azimuth difference angle between sun and satellite, the surface type and NDVI. The used kernels *a* are in Table 3-1. (Wu et al. 1995).

The kernels (*a)* are separate for forest, barren, grassland, and cropland land cover types (coefficient values are listed in Table 3-1). For SAL algorithm, these classes are compressed from global land use classification (LUC) datasets as shown in Table 3-2 to

Table 3-4. The LUC datasets used in CLARA-A2 SAL are listed in Table 3-5. The GLC2000 does not cover the whole area of CLARA-A2 SAL. For the areas not covered by the GLC2000, reprojected USGS data is used. The algorithm uses the land cover data that is nearest in time.

Table 3-1: Kernel coefficients used in CLARA SAL BRDF correction computation. Coefficients are land cover specific. Coefficients a_{x1} are for red channel, a_{x2} are for NIR channel. (Wu et al. 1995).

Scene type	a_{11}	a_{21}	a_{12}	a_{22}
Barren	0.21	1.629	0.212	1.512
Cropland	0	$3.622 * NDVI^{0.539}$	0	$1.62*NDVI^{0.109}$
Forest	0	$3.347 * NDVI^{0.153}$	0	$1.830*NDVI^{-0.105}$
Grassland	$1.335 * e^{-11.39*NDVI}$	$-0.493+ 14.94*NDVI - 18.32 * NDVI^2$	$7.745 * e^{-22.8*NDVI}$	$- 0.250 + 13.88 * NDVI - 20.43 *NDVI^2$

Table 3-2: The rules for reclassifying USGS land cover classification to conform with available BRDF model classes

USGS class	BRDF class
1, 19, 23	Barren
8, 11, 12, 13, 14, 15, 21	Forest
2, 3, 4, 5, 6	Cropland
7, 9, 10, 17, 18, 20, 22	Grassland
24	Snow
16	Water

Table 3-3: The rules for reclassifying GLC2000 land cover classification to conform with available BRDF model classes.

GLC2000 class	BRDF class
10, 19, 22	Barren
1, 2, 3, 4, 5, 6, 7, 8, 9, 11, 12	Forest
13, 15, 17	Cropland
14, 16, 18	Grassland
21	Snow
20	Water

Table 3-4: The rules for reclassifying GlobCover land cover classification to conform with available BRDF model classes.

GlobCover class	BRDF class
190, 200	Barren
40, 50, 60, 70, 90, 100, 110, 160, 170	Forest
11, 14, 20, 30,	Cropland
120, 130, 140, 150, 180	Grassland
220	Snow
210	Water

Table 3-5: The Land use classifications used in CLARA-A3 SAL.

LAND USE CLASSIFICATION	reference	used in CLARA-A3 SAL from
USGS 1993	http://edc2.usgs.gov/glcc/globdoc1_2.php	1.1.1982
GLC2000	http://bioval.jrc.ec.europa.eu/products/glc2000/glc2000.php	1.7.1996
GLOBCOVER 2005	http://due.esrin.esa.int/globcover/	1.7.2002
GLOBCOVER 2009	http://due.esrin.esa.int/globcover/	1.1.2007
ESA CCI 2015	https://www.arcgis.com/home/item.html?id=a1be33f800fc46f1abdb449664c2f78f	1.1.2012

It should be noted that the BRDF correction may have some inaccuracies in areas where the recorded land use classification does not correspond well to the physical characteristics of the scene. An example of this might be a tilled field where no green vegetation exists. CLARA SAL attempts to remove some of such effects by classifying the pixel as ”Barren” if the NDVI value is below 0.1, regardless of the LUC type. Also, man-made LUC changes may cause erroneous BRDF corrections because the LUC data is not updated regularly.

In the CLARA SAL algorithm, the anisotropy factor (Ω) is first used to normalize the surface reflectance to a common viewing and illumination geometry of zenith Sun, nadir view using (Li 1996)

$$\rho(0,0,\varphi) = \frac{\Omega(0,0,\varphi)}{\Omega(\theta_s,\theta_v,\varphi)} * \rho_{surf}(\theta_s,\theta_v,\varphi) \quad (31)$$

By dividing the BRDFs with the anisotropy factor we get the normalization factor which is then used to multiply the surface reflectance to get the anisotropy-corrected & normalized surface reflectance (Wu et al. 1995). For AVHRR channels, the eq 31 are

$$\rho_{RED}(0,0,\varphi) = \frac{\Omega_{RED}(0,0,\varphi)}{\Omega_{RED}(\theta_s,\theta_v,\varphi)} * \rho_{RED}(\theta_s,\theta_v,\varphi) \quad (32)$$

$$\rho_{NIR}(0,0,\varphi) = \frac{\Omega_{NIR}(0,0,\varphi)}{\Omega_{NIR}(\theta_s,\theta_v,\varphi)} * \rho_{NIR}(\theta_s,\theta_v,\varphi) \quad (33)$$

Now we have BRDF-corrected surface reflectances, normalized to a common viewing and illumination geometry. The next step produces hemispherical spectral surface albedo images.

Knowledge of the BRDF can also be used to derive the spectral albedo directly from surface reflectances through integration over all viewing directions. This relation is used in CLARA SAL to derive the spectral albedo with the integrated formula and angular terms by Roujean et al. (1992), combined with kernel coefficients by Wu et al. (1995)

$$\alpha(\theta_s) = \rho(0,0,\varphi) * (1 + a_{1i}I_1 + a_{2i}I_2) \quad (34)$$

keeping in mind that $\alpha(\theta_s) = k_0 + k_1I_1 + k_2I_2$, $a_i = k_i/k_0$ and $\rho(0,0,\varphi) = k_0$ (Roujean et al., 1992 and Wu et al., 1995). To get the actual absolute value, the nadir-normalized surface reflectance values are multiplied with the BRDF kernels. The hemispherical albedos for AVHRR channels 1 and 2 are

$$\alpha_{RED}(\theta_s) = \rho_{RED}(0,0,\varphi) * (1 + a_{11}I_1 + a_{21}I_2) \quad (35)$$

$$\alpha_{NIR}(\theta_s) = \rho_{NIR}(0,0,\varphi) * (1 + a_{12}I_1 + a_{22}I_2) \quad (36)$$

The integrated forms of the angular dependency terms are

$$I_1 = -0.9946 - 0.0281tan\,\theta_s - 0.0916tan^2\,\theta_s + 0.0108tan^3\,\theta_s \quad (37)$$

$$I_2 = -0.0137 + 0.0370tan\,\theta_s + 0.0310tan^2\,\theta_s - 0.0059tan^3\,\theta_s \quad (38)$$

The algorithm result $\alpha(\theta_s)$ at this stage is a spectral albedo for red and NIR wavelengths. The albedo corresponds to the sun zenith angle at the time of satellite observation.

3.4 Calculating albedo estimates over sea areas

The ice-free sea (lake) surface albedo retrieval of CLARA-A3 SAL is based on the method by Jin et al. (2011). As it does not use AVHRR data at all, there is no need to provide AOD

information for ocean pixels. It is an update of the previous look up table (LUT) based approach (Jin et al., 2002, 2004) that was used in the generation of open water albedo for CLARA-A1 SAL. In the current method the albedo α is parametrized for the direct and diffuse incident radiation separately, α_{dir} and α_{diff} respectively, and then each of them is further divided into two components: the contributions from surface (s) and water (w), respectively:

$$\alpha_{dir} = \alpha_{dir}^{s} + \alpha_{dir}^{w} \quad (39)$$

$$\alpha_{diff} = \alpha_{diff}^{s} + \alpha_{diff}^{w} \quad (40)$$

$$\alpha = f_{dir}\alpha_{dir} + f_{diff}\alpha_{diff} \quad (41)$$

$$f_{dir} + f_{diff} = 1.0 \quad (42)$$

where f_{dir} and f_{diff} represent the direct and diffuse fractions of the incident flux at surface in the specified spectrum, respectively. For the CLARA-A3 SAL black-sky albedo SAL, f_{diff} = 0, so that $\alpha = \alpha_{dir}$. For the white-sky albedo (WAL) f_{diff} = 1 and for the blue-sky albedo (BAL) values the long-term average of ocean areas f_{diff} = 0.7 is used in eq. 41. The ocean volume component for broadband albedo is small and it is approximately 0.006 for the so called case 1 waters, which constitute 99% of the oceans (Jin et al., 2011). Thus, the effect of chlorophyll variation is not taken into account and $\alpha_{diff}^{w} = \alpha_{dir}^{w} = 0.006$. The surface component of the albedo corresponding to the direct illumination is

$$\alpha_{dir}^{s}(\lambda, \theta, w) = \alpha_{dir}^{s}(n(\lambda), \mu(\theta), \sigma(w)) = r_f(n, \mu) - \frac{r_f(n,\mu)}{r_f(n_0,\mu)} f(\mu, \sigma) \quad (43)$$

where $\mu = \cos(\theta)$ and θ is the solar zenith angle, $r_f(n, \mu)$ is the Fresnel reflectance, $n^0 = 1.34$ is approximately the refractive index of water in the visible spectrum (Jin, 2011) and σ is the mean slope distribution width of the Gaussian function defining the surface roughness and depends on the wind speed w as follows

$$\sigma^2 = 0.003 + 0.00512\, w \quad (44)$$

The regression function $f(\mu, \sigma)$ reduces to zero when w = 0 and is defined as

$$f(\mu, \sigma) = (p_0 + p_1\mu + p_2\mu^2 + p_3\mu^3 + p_4\sigma + p_5\mu\sigma)exp(p_6 + p_7\mu + p_8\mu^2 + p_9\sigma + p_{10}\mu\sigma) \quad (45)$$

where the fitting coefficients p_i(i=0,1,2,…,10)=(0.0152, -1.7873, 6.8972, -8.5778, 4.071, 7.7447, 0.1643, -7.8409, -3.5639, -2.3588, 10.0538).

Major portion of the solar incidence at surface is within the visible spectrum with maximum at around 500 nm. For broadband solar radiation, the direct albedo component from surface reflection can be represented by the spectral parameterization of eq. 43 with $n = n_0 = 1.34$ (Jin, 2011; Röttgers, 2011).

The foam albedo is taken to be α_{wc} = 0.55, and its effect on the total albedo α (from eq. 51, which may represent black-, white-, or blue-sky albedo) is introduced as a weighted sum as follows

$$\alpha = f_{wc}\alpha_{wc} + (1 - f_{wc})(\alpha + 0.006) \quad (46)$$

where f_{wc} is the fractional surface coverage of white-caps, which depends on the wind speed

$$f_{wc} = 2.95 \times 10^{-6} w^{3.52} \quad (47)$$

Technically, the foam correction is applied in both black- and white-sky calculations in order to retain it for all delivered albedo quantities. In the version CLARA-A1 SAL only the sun zenith angle was taken into account. In CLARA-A2 SAL also the wind speed was included in the calculations. The solar zenith angles used correspond to clear-sky AVHRR overpasses. This is to keep the same logistics in ocean and land areas, and because on land the albedo is derived only for cloud free pixels. In both CLARA-A1 SAL and CLARA-A2 SAL the ice-free sea albedo was normalized to the sun zenith angle value of 60°. Ocean albedo is not normalized in CLARA-A3 SAL.

The white-sky albedo components of oceans are (Jin et al., 2011)

$$\alpha_{dif}^{S}(\lambda, w) = \alpha_{dif}^{S}(n(\lambda), \sigma(w)) = -0.1479 + 0.1502n - 0.0176n\sigma \quad (48)$$

The diffuse volume component is the same as the direct volume component at μ = 0.676 and similar foam correction (Eq. 46) is used for the white-sky albedo as for black-sky albedo. Finally, the blue-sky albedo is again derived from Eq. 3.

3.4.1 Sea surface albedo using wind speed data

In this section it is described how the wind speed data required for the ocean surface albedo determination (Section 3.4) is compiled from Scanning Multi-channel Microwave Radiometer (SMMR), Special Sensor Microwave Imager (SSM/I), Special Sensor Microwave Imager Sounder (SSMIS) and anemometer based wind speed data. To keep the albedo detached from modelling, the wind speed estimates were based only on satellite/anemometer data. Moreover,

in first place they were chosen to be derived only from microwave radiometer data, in order to keep the data set as homogeneous as possible. However, between SMMR and SMM/I data sets there was a gap during January 1985 – June 1987, for which time range the wind speed was estimated from anemometer data.

Daily wind speed data based on SSM/I or SSMIS are available globally from July 1987 onwards, except for December 1987 (Wentz, 1997). For that month again anemometer data was used as substitute. The SSM/I and SSMIS data were intercalibrated. The products are in a 0.25° x 0.25° grid. Weekly composites of SSM/I wind speed data were constructed by averaging the daily data. The window of the data was chosen so, that their centres match the centers of the pentads of the SAL products to be calculated. Thus the successive weekly averages slightly overlap. In one or two cases the weekly mean had minor gaps. To fill them the weekly average was replaced by a nine day average.

Monthly wind speed data is available from SMMR during the years 1979-1984, (NIMBUS-7 SMMR Global Air-Sea Parameters in Swath (Wentz,1997, Vazquez, 1997). The data is in the form of 719*1440 pixels, i.e. the pixel size is 0.25° in both latitude and longitude direction. The spatial resolution is 60 km x 60 km.

When satellite data were not available, anemometer based data were used instead (Tokinaga, 2013). WASWind (Wave and Anemometer-based Sea Surface Wind) provides a bias-corrected marine surface wind dataset over the global oceans (Thomas et al., 2008). WASWind has been constructed from wind observations in ICOADS (International Comprehensive Ocean-Atmosphere Data Set) and is available at monthly resolution on a 4° x 4° grid from 1950 to 2009. This data set was markedly sparser than the satellite based data sets. In addition, values were missing in large areas of the southern hemisphere.

Therefore ‘climatological’ values were calculated for the missing pixels using the SMMR and SSM/I data sets during years 1979 – 1996. This was obtained the following way: For each anemometer product pixel the dependence of the wind speed on the Julian day was analyzed using polynomial fitting of third order (Figure 3-10). The monthly value of the SMMR data was allocated to the 15th day of the month. If there were available fewer than 5 points for the regression, the third degree polynomial was replaced by a constant that equaled the average value of the 5 points.

Now, the missing values from the anemometer wind speed product were replaced by the estimates calculated for the 15th day of the month in question applying the regression polynomials (or constants). If the calculated value deviated more than 10 m/s from the neighbor pixel towards north (previous row), it was decrease/increased so, that the difference was exactly 10 m/s, which value then replaced the missing value. This restriction was made, because the typical difference between neighbor pixels in north/south direction was at most 10 m/s in the original anemometer based wind speed product. After filling the gaps of the original wind speed product, its pixel size was decreased from 4° to 0.25° to match that of the radiometer based wind speed products. The intermediate values were obtained using linear interpolation.

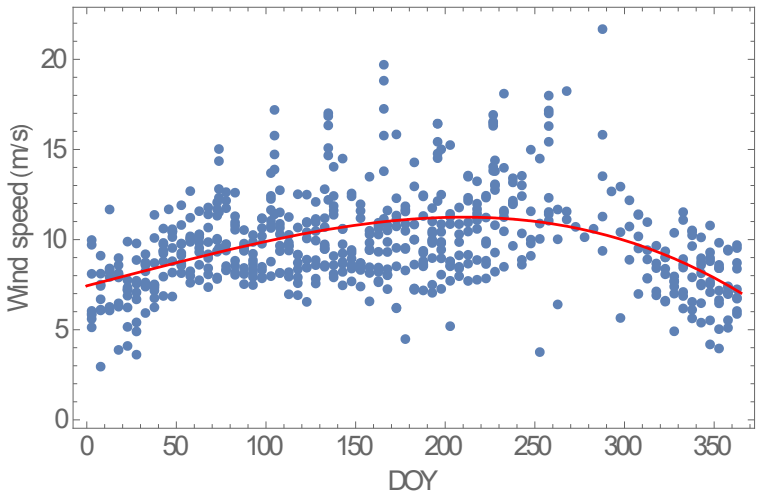

Figure 3-10: Variation of wind speed in one pixel during 1979-1984 and 1987-1996 as a function of the day of the year (DOY). The wind speed estimates are based on SMMR or SSM/I data. The regression polynomial (red curve) is w = 7.43593 + 0.0253204 DOY + 0.000017422 DOY^2 - 2.46116*10^-7 DOY^3, where w is the wind speed. This example point is situated at 60°N, 42°E.

The calibration of the anemometer based wind speed data was compared with that of the SSM/I. It turned out that the anemometer wind speeds had to be multiplied by 0.954 to achieve equal level. The coefficient of determination for this relation was only 0.88, which is understandable as the anemometer data is more point wise and the satellite data aerial averages. A corresponding relationship between the anemometer based wind speed and that of SMMR turned out to be 1.096 with R^2=0.84. Thus the SMMR based wind speed estimates were multiplied by 0.870 (= 0.954/1.096). Finally, the gaps within the wind speed data of SMMR were filled with linear interpolation. Extrapolation was not used, hence the southern edge of wind speed values varies. Despite of the scaling, the wind speed values before 1988 are of lower quality than the times series beginning in1988.

In the Arctic sea ice area the wind speed is taken into account in open water pixels, if the wind speed estimate is available. If the wind speed value is unknown, the albedo is calculated assuming it to be 0 m/s. It is possible that the OSI-SAF ice extent information does not fully agree with the ice information of the wind speed data. In that case the wind speed value may be missing, although there is open water in the pixel. However, then the pixel is probably very close to the ice edge, so that the wind speed effect on the water surface is attenuated by the minimal ice concentration (<15%). Then the assumption of completely calm water (i.e. wind speed = 0 m/s) is acceptable.

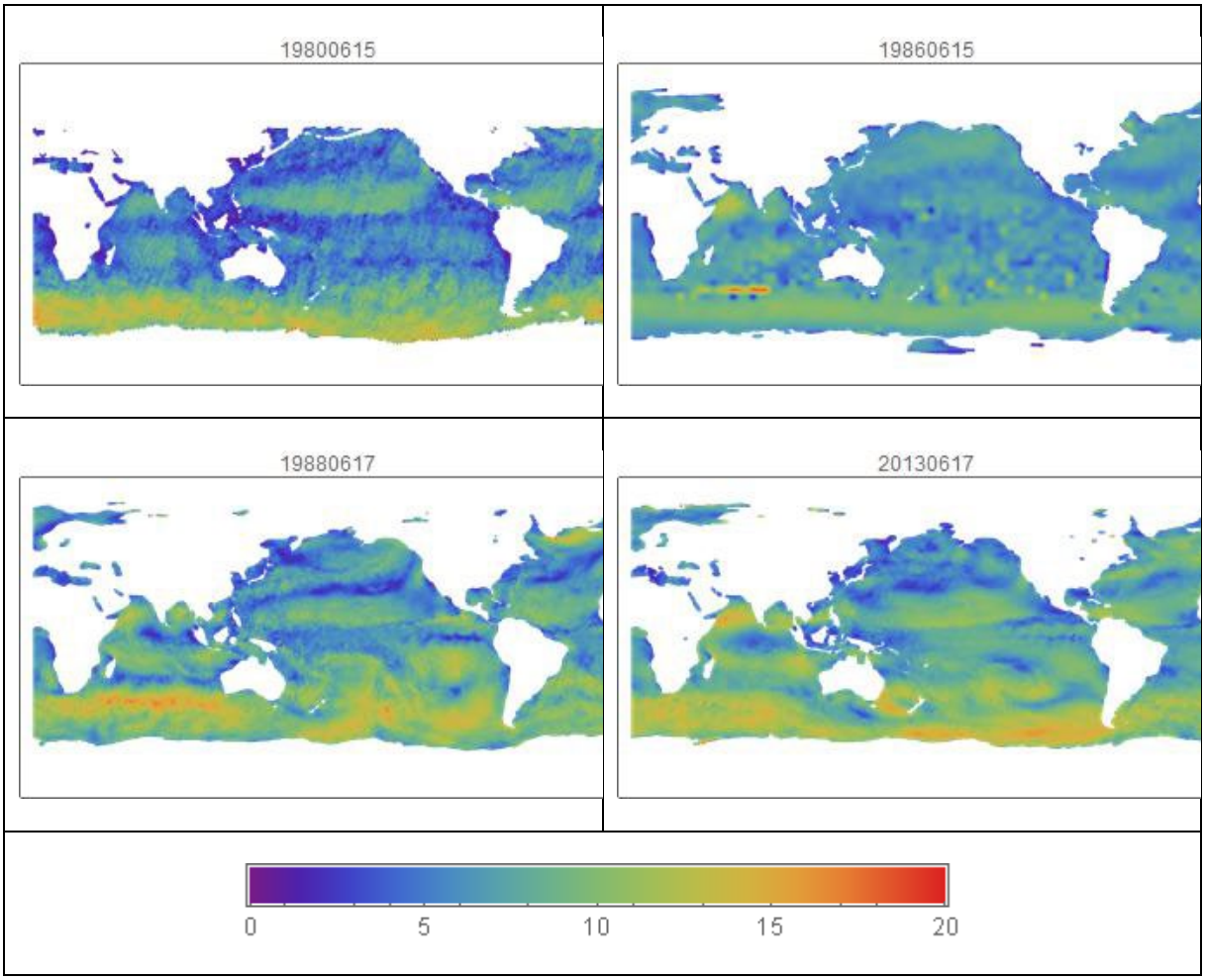

Figure 3-11: Wind speed examples based on SMMR (top left), anemometer (top right), SSM/I (bottom left) and SSMIS (bottom right) data. The values are in m/s.

Examples of the wind speed time series are shown in Figure 3-11. NASA EOSDIS data center GHRC DAAC is acknowledged for the satellite based wind data.

3.4.2 Sea ice

The CLARA-A3 SAL algorithm uses Ocean and Sea Ice SAF (OSI-SAF) sea ice extent data (http://osisaf.met.no/docs/osisaf_ss2_pum_ice-conc-edge-type.pdf), which is provided via the PPS output, to confirm the snow/ice – no snow/ice classifications. The SAL algorithm uses the OSI-SAF data to decide whether the pixel is open water or ice covered. The threshold used is 1 %.

The OSI-SAF sea ice extent data consist of daily maps of ice cover in the Arctic and Antarctic areas. For the data-gaps of OSI-SAF the SAL algorithm uses the nearest OSI-SAF data available. The data gaps are shown in Table 3-6 .

Table 3-6: Data gaps of the daily OSI-SAF ice concentration data for northern hemisphere (NH) and southern hemisphere (SH).

Year/Month	missing days NH	missing days SH
1986/04	1.-17., 19.-30.	1.-3., 5.-9., 11., 13,. 15,. 17., 21., 23., 25., 27.
1986/05	1.-20., 22. ,26.	3., 5,. 7., 15., 17,. 21.-25., 27.-31.
1986/06	1., 7.-23., 25., 27., 29.	1.-6., 8.-16., 18., 25., 27.
1987/12	3.-31.	3.-31.
1987/01	1.-12.	1.-12.

3.5 Calculating SAL over snow-covered areas

Performing a robust and accurate BRDF correction for snow using currently available methods is difficult because many different types of snow exist with widely varying reflectance anisotropy characteristics. Since a robust instantaneous BRDF correction is beyond our currently available capabilities, we have chosen to account for reflectance anisotropical effects using an empirical time-averaging treatment.

Our approach is based on the assumption that the directional-hemispherical reflectance (black-sky albedo) can be estimated with sufficient accuracy by sampling it from various viewing directions. By averaging the directional-directional reflectances of a snow site over a sufficient time-period (5 days or more), the resulting temporal average of snow albedo should be accurate even if the observed directional-directional reflectances (observed CLARA SAL products) have significant BRDF-related under- and overestimations.

The retrieval method depends on sufficient sampling of the viewing hemisphere during the observation period. To demonstrate the achievable sampling, we show the sampled viewing zenith and azimuth angles during 2008 for the DYE-2 site on the Greenland Ice Shelf (66.48N, -46.28E) in Figure 3-12. The figure shows how the viewing geometries of the retrievals are evenly distributed except for an angular range in the cross-principal plane direction (keeping in mind the principal plane symmetry). The unsampled angular range contributes very little to the angular reflectance isotropy of snow, as shown through comparison to modelled snow reflectance anisotropy on the right after Jiao et al. (2019). As it is a fair assumption that such distributions are similar at each longitude, we expect that similar distributions will occur over Canada and Northern Eurasia as well. As we approach the poles, the satellite retrieval density increases, further increasing the representativeness of our hemispherical reflectance sample and thus increasing the accuracy of the albedo estimate.

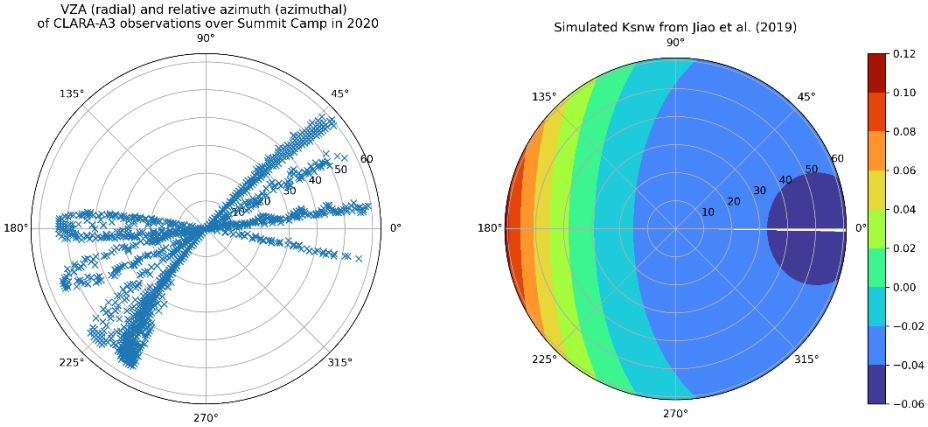

Figure 3-12: Satellite zenith and azimuth angles of successful CLARA-A3 SAL retrievals during 2020 at Summit Camp in Greenland (left). The polar plot shows viewing (satellite) zenith angles in the radial axis and viewing azimuth angles in the angular axis. On the right, an example of the deviation of angular snow reflectance from its isotropic mean as modeled by the snow kernel proposed by Jiao et al. (2019).

The method is most accurate during periods when the snow over a site experiences no significant changes. Melting and first snowfall periods will show a different BRDF signature over a site, and thus the estimated temporal means of albedo may suffer in accuracy. However, using our method, the albedo estimate is always based on the realized reflectances of the snow pack. Thus none of the inaccuracy results from an inappropriately chosen snow reflectance model for a scene. Furthermore, it should be noted that the narrow-to-broadband conversion (discussed next) self-adapts to wet and dry snow cover.

3.6 Narrow-to-Broadband Conversion of SAL

The last remaining stage in deriving the surface broadband albedo is the conversion from spectral directional albedo to broadband albedo. The instruments observing the radiances only pick up information in discrete spectral bands, such as the 0.58 - 0.68 μm red and 0.725 - 1 μm NIR wavelength channels of AVHRR (used for CLARA SAL/WAL/BAL). Climatological applications for albedo require a total shortwave broadband albedo to be derived, so the observed spectral albedos must be extended to full shortwave spectral width. This is accomplished by the narrow-to-broadband conversion (NTBC) algorithm.

There are several NTBC algorithms employed in CLARA SAL to account for all the surface types. The employed algorithms are based on the study results that atmospheric conditions do not significantly affect the conversion from narrow- to broadband albedo, and therefore linear regression may be used to extrapolate broadband albedo from the narrowband observations as shown by several studies (van Leeuwen and Roujean 2002, Xiong et al. 2002, Liang 2000, Song and Gao 1999, and references therein).The methodology of deriving the regression coefficients may be found in the relevant publications.

Broadband surface albedo algorithms are usually limited by the sun zenith angle range that they can accept. For many surface types, the albedo of a scene with a large sun zenith angle

becomes difficult to model due to extensive atmospheric scattering because of longer path lengths, as well as the irregularity of the scene BRDF at large sun zenith angles (van Leeuwen and Roujean 2002, DeAbreu et al. 1994). Similar limitations apply to satellite observations with large satellite zenith angles for similar reasons. As a result, CLARA SAL omits all observations with larger sun zenith angles (SZA) or viewing zenith angles (VZA) than a preprogrammed maximum. The assigned limits to SZA and VZA in CLARA SAL are 70 degrees and 60 degrees, respectively.

CLARA SAL chooses the linear combination method according to sensor and surface type. For all non-snow land surfaces observed by an AVHRR, the broadband albedo is computed following a narrow-to-broadband conversion (NTBC) approach by Liang (2000). The NTBC is

$$\alpha = -0.3376 \cdot \alpha_{RED}^2 - 0.2707 \cdot \alpha_{NIR}^2 + 0.7074 \cdot \alpha_{RED} \cdot \alpha_{NIR} + 0.2915 \cdot \alpha_{RED} + 0.5256 \cdot \alpha_{NIR} + 0.0035 \quad (49)$$

For any snow/sea ice pixels (identified by cloud mask snow/ice flag or OSI-SAF over ocean pixels), the method follows Xiong et al. (2002). The equation is as follows:

$$\alpha = 0.28(1 + 8.26\Gamma)\alpha_{RED} + 0.63(1 - 3.96\Gamma)\alpha_{NIR} + 0.22\Gamma - 0.009 \quad (50)$$

where

$$\Gamma = \frac{\alpha_{RED} - \alpha_{NIR}}{\alpha_{RED} + \alpha_{NIR}} \quad (51)$$

Again, the reader is reminded that the chosen empirical-temporal BRDF correction method implies that the output of the NTBC algorithm at the instantaneous image level is a bidirectional surface reflectance, which the temporal averaging (may be thought of as a coarse integration over the viewing hemisphere) converts into a directional-hemispherical reflectance (or black-sky albedo).

Since the SZA dependency of a snow pack depends on the snow pack characteristics (Wang and Zender, 2011), it is more difficult to model, and a single normalization scheme for SZA dependency of snow albedo is not yet available. Therefore we omit this normalization at this time to avoid introducing artificial errors into the product, as well as the normalization of snow free pixels on land to retain better homogeneity within the product.

The realized SZA for land/snow pixels in the end products will correspond with the average SZA of the individual overpasses that consist of the time averaged product. The processing limit for SZA remains at 70 degrees, thus providing an upper limit for the realized SZA of the products. Mean SZA per pixel is provided for users wishing to make their own normalization.

Since the CM SAF CLARA SAL distributable products are the pentad and monthly means, the final step performed is the temporal averaging. The currently used method is the arithmetic average of all observed retrievals in a 0.25 degree end product pixel over the pentad/month in question (25 km in equal-area polar subsets).

3.7 Level 3 processing for spatiotemporally aggregated SAL, WAL, and BAL

3.7.1 Overview & spatio-temporal averaging

Upon completion of the level 2 processing outlined earlier, the overpass-level albedo estimate data are reprojected onto a global 0.25 degree lat-lon grid, as well as the polar 25 km EASE-2 grids (EPSG 6931 & 6932). Bucket resampling is used, i.e. the sums of the variable data (also in second, third, and fourth power) and the number of pixels in each "bucket" is saved. All non-valid observations are discarded. For direct irradiance fraction f_{dir}, all valid-geometry observations are accepted in order to generate a temporal average of f_{dir} which represents the actual cloud conditions of the whole observation period.

In order to calculate the final results, moments and standard deviation of the variables are first computed as follows (*sum* and *num* denoting the temporally-aggregated sum and observation count per grid cell, i.e. temporal sums of spatially summed data from bucket-resampled overpasses):

$$mean = sum / num \quad (52)$$

$$square_of_means = mean * mean \quad (53)$$

$$cube_of_means = square_of_means * mean \quad (54)$$

$$fourth_of_means = square_of_means * square_of_means \quad (55)$$

$$mean_of_squares = sum*sum / num \quad (56)$$

$$mean_of_cubes = sum*sum*sum / num \quad (57)$$

$$mean_of_fourths = sum*sum*sum*sum / num \quad (58)$$

$$moment2 = mean_of_squares - square_of_means \quad (59)$$

$$moment3 = (mean_of_cubes - 3 * mean * mean_of_squares + 2 * cube_of_means) \quad (60)$$

$$moment4 = (mean_of_fourths - 4 * mean * mean_of_cubes + 6 * square_of_means * mean_of_squares - 3 * fourth_of_means) \quad (61)$$

$$std = sqrt(num / (num - 1) * moment2) \quad (62)$$

Following this stage, skewness and kurtosis are calculated as follows:

$$Skewness = moment3 / std\text{^}3 \quad (63)$$

Kurtosis = moment4 / std^4 (64)

Skewness is limited to range -5000…5000 and kurtosis to 0…5000. In addition, the median of the data is calculated, and for snow, the mean reflectances are calculated at overpass level, i.e. sum/num calculated for each overpass, and averaged over all valid overpasses to yield the mean snow reflectance for use in calculating WAL and BAL.

Following the discussion in section 3.2, the black-sky albedo mean, std, skewness, and kurtosis are corrected for non-zero cloud probability during the observation times with eqs. (65 & 66). The correction is applied everywhere except over open water bodies.

Then, the temporal mean of white-sky albedo is calculated from the observed statistics of black-sky albedo and SZA (see section 3.7.2.2). Finally, the blue-sky albedo (BAL) is estimated from the f_{dir}-weighted SAL and WAL (see section 3.7.2.3). At this stage, observations classified as snow and non-snow are available separately. The combined snow + non-snow albedo estimates are finally formed through observation count-weighted summing of the snow and non-snow albedo estimates. Figure 3-13 summarizes the level 3 processing flow for easier reference.

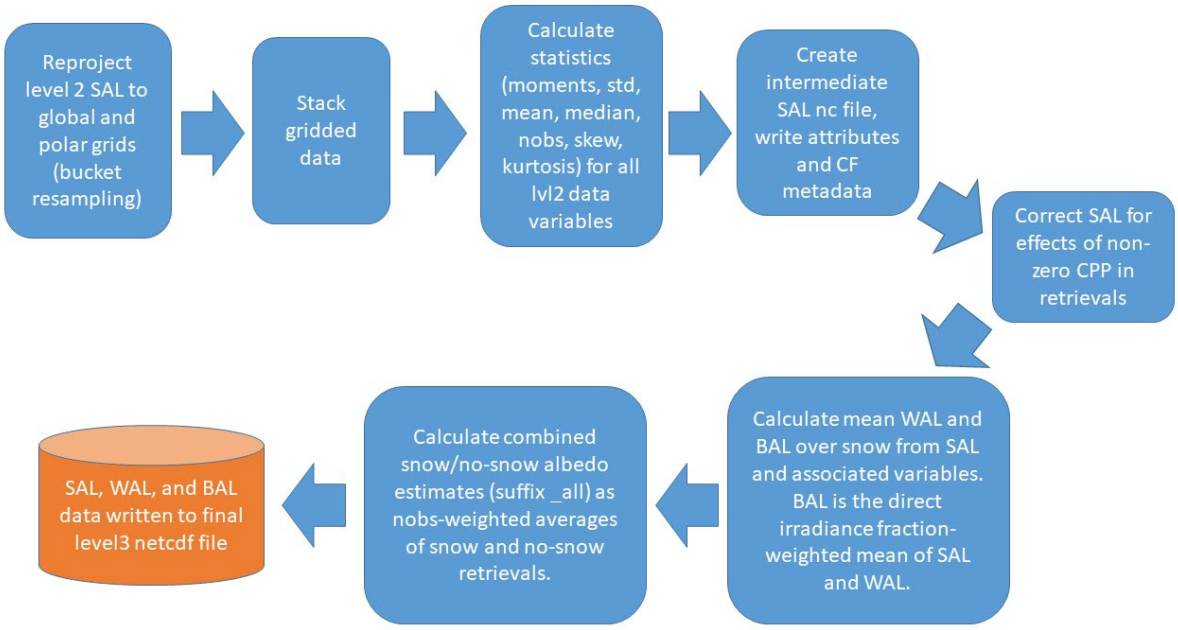

Figure 3-13: Overview of CLARA-A3 SAL/WAL/BAL level 3 processing flow

3.7.2 Deriving final albedo estimates, cloud probability usage

3.7.2.1 Correcting SAL for non-zero cloud probability

The top of atmosphere (TOA) reflectances used as CLARA SAL input are derived by the PPS software package. Satellite inter-calibration and trend corrections for individual sensors are accomplished using an updated version of the method described by Heidinger et al. (2010). The process creates the Fundamental Climate Data Record (FCDR) of AVHRR normalized

radiances with respect to irradiance at the top of atmosphere. The Heidinger algorithm recalibrates AVHRR radiances using simultaneous Moderate Resolution Imaging Spectroradiometer (MODIS) overpasses at nadir viewing geometry during the MODIS data period (2000-2014). For the older AVHRR period, targets with stable surface reflectance (Libyan Desert and Dome-C on Antarctica and in the recent version also a target on Greenland) were characterized by MODIS observations and then assumed to be fully stable calibration points for the rest of the AVHRR data series.

Sun-Earth distance variation is also accounted for in the preprocessing. A separate pre-processing script for CLARA SAL then corrects the Sun Zenith angle difference from 0 degrees (the so-called cosine correction).

The identification of cloud probabilities per pixel in the AVHRR images is performed by the PPS software package in the pre-processing stage. Its detailed performance description is beyond the scope of this document - details on the AVHRR-PPS package and cloud probability and cloud mask derivation may be found in Karlsson et al. (2020), the NWC SAF ATBD (2021) by Karlsson et al. and Dybbroe et al. (2005). PPS outputs include both the binary cloud mask, derived by a decision tree-approach, and the probability of cloudiness as derived from Bayesian theory. The cloud probability values provided by the PPS software are used in CLARA SAL as the main cloud input data. The flags of the cloud mask are used as additional information to flag questionable pixels not to be used for albedo retrieval. The cloud probabilities are retrieved at nominal GAC resolution, thus they are directly applicable data for CLARA SAL processing.

Previously it has been shown that the black-sky albedo can be estimated from not cloud masked albedo distributions (Manninen et al., 2004). For typical snow-free land cover types the cloudy pixels constitute an essentially exponentially decaying tail of higher values for the surface albedo distribution. Since the surface albedo of a snow-free pixel does not typically vary in a large range, whereas the cloud cover albedo does, the cloud-free pixels typically constitute the peak of the distribution. For snow-covered terrain the cloudy pixels constitute an essentially exponentially decaying tail of smaller albedo values, as snow is typically higher reflecting than clouds. For old snow and sea ice the cloud and snow albedo distributions may coincide. For snow-free land cover the albedo distribution alone is mostly sufficient for albedo estimation, but for snow covered terrain the availability of pixelwise cloud probability values improves the discrimination of the land, snow and sea ice from cloud cover. However, processing monthly distributions for every pixel of the SAL product (1440*720) for every month and year (1979-2020 plus ICDR extension) is too time consuming to be practical. Hence, for each pixel the first estimates for the monthly mean albedo values $\bar{\alpha}$ were derived simply as weighted means of the individual pixelwise albedo values α_i using as the weights exponentials of the individual pixelwise cloud probability values CP_i

$$\bar{\alpha} = \sum_{i=1}^{n} \alpha_i \exp(-d\ CP_i) / \sum_{i=1}^{n} \exp(-d\ CP_i) \quad , \tag{65}$$

where n is the number of individual albedo values within the average (month or pentad). The value 0.1 for the coefficient d was derived empirically. Thus, more weight is given to albedo estimates corresponding to lower cloud probability. For monthly means the number of individual observations having cloud probability smaller than 20 % is typically sufficient and

was used for SAL retrieval. It should be noticed that here α_l refers to values already processed to the surface according to Sections 3.3 or 3.4.

It should be noted that the weighted mean approach of eq. 65 might produce biased values, when only relatively cloudy (*CP* = 20%) pixels are available. Therefore, statistical relationships were simulated theoretically between the albedo estimates and the true cloud-free albedo value (Manninen et al., 2021) and the following correction formula for pixelwise monthly mean albedo values was derived to obtain the final monthly mean albedo estimate $\hat{\alpha}$

$$\hat{\alpha} = \bar{\alpha}\left(1 + c_1\overline{CP} - \frac{c_2\,\overline{CP}}{\bar{\alpha}}\right) \quad . \tag{66}$$

Here $\overline{CP}$ denotes the monthly mean cloud probability for values in the range [0,20). Similar type of corrections were made also for the standard deviation, skewness and kurtosis of the monthly albedo. Pentad values were derived similarly as the monthly values. The values for the empirical parameters c_1 and c_2 are given in Table 3-7.

Table 3-7: Parameter values of eq. 66 for monthly mean, standard deviation, skewness and kurtosis of surface albedo.

Variable	c_1	c_2
Mean	0.006343	-0.1335
Standard deviation	-0.0005595	-0.04121
Skewness	0.008168	0.05647
Kurtosis	0.001205	0.1137

Statistical relationship between simulated albedo and its estimate from eqs. 65 and 66 are presented in Table 3-8 for 612 cases with varying number of individual points and varying empirical cloud probabilities picked from a global data set of June 2012 (Manninen et al., 2021). The number of individual albedo values, on which the previous statistics is based is not crucial for the albedo estimation accuracy (Figure 3-14).

Table 3-8. Simulated statistics for the absolute and relative absolute differences of the estimates (^) and true values of albedo (α), standard deviation (σ) skewness (γ) and kurtosis (β). The calculations were made for simulated true albedo values (α) of 10%, 20%, 30%, 40%, 50%, 60%, 70% and 80%. The albedo values are in the range 0 – 100%.

	$\lvert\hat{\alpha}-\alpha\rvert$	$\frac{\lvert\hat{\alpha}-\alpha\rvert}{\alpha}$	$\lvert\hat{\sigma}-\sigma\rvert$	$\frac{\lvert\hat{\sigma}-\sigma\rvert}{\sigma}$	$\lvert\hat{\gamma}-\gamma\rvert$	$\frac{\lvert\hat{\gamma}-\gamma\rvert}{\gamma}$	$\lvert\hat{\beta}-\beta\rvert$	$\frac{\lvert\hat{\beta}-\beta\rvert}{\beta}$
Mean	0.48	0.011	0.0079	0.0076	0.038	0.0098	0.0033	0.018
Median	0.32	0.0089	0.0063	0.0041	0.020	0.0056	0.0018	0.010
90 % quantile	1.1	0.022	0.019	0.018	0.09	0.022	0.0083	0.042
Max	2.8	0.078	0.037	0.058	0.30	0.071	0.035	0.124

The theoretical form of eq. 66 turned out to slightly underestimate high monthly mean albedo values. Hence, an empirical relationship was derived for the monthly mean surface albedo

values and instead of eq. 66 the following formula was used in CLARA-A3 SAL for the monthly mean values

$$SAL = \hat{\alpha} = 1.0332\,\bar{\alpha} - \overline{CP}(-0.05600 + 0.007026\,\bar{\alpha}) \quad . \qquad (67)$$

It is anticipated that better values for parameters c_1 and c_2 will be derived, when CLARA-A3 *CP* data is available globally for at least one year. Then the final correction for the monthly mean surface albedo value will be made for CLARA-A3.5 using eq. 66 and the new parameter values.

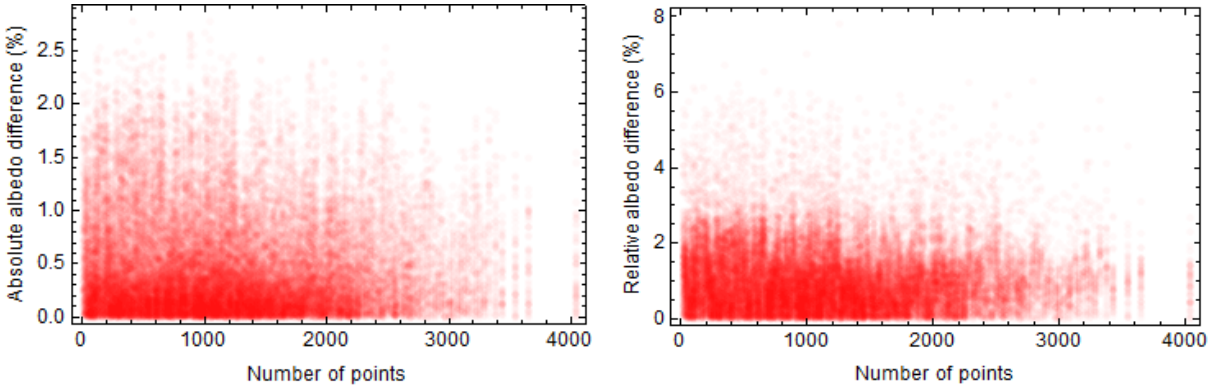

Figure 3-14: Absolute (left) and relative (right) difference between the albedo estimate and the true albedo value as a function of the number of points included in the mean albedo value.

Examples of albedo distributions with cloud probability restricted to smaller than 20 % are shown in Figure 3-15 and Figure 3-16. The monthly albedo estimate $\hat{\alpha}$ is shown as well. Corresponding in situ measured albedo distributions are shown also in Figure 3-15. The estimated monthly mean black-sky albedo values are compared with in situ measured monthly mean values exclusively collected during clear-sky satellite retrieval times, thus ensuring comparability, as direct radiation dominates the in situ albedo (Table 3-9). Since the in situ measurements contain contribution of the atmosphere in the global radiation value, but not in the reflected radiation value, the in situ albedo values of dark targets are higher than the corresponding satellite black-sky retrievals, and the higher the larger the aerosol optical depth (AOD) is. In addition, where the surroundings of the in situ measurements are heterogeneous and deviate clearly from the in situ measurement surface (like the agricultural areas in Fort Peck), the seasonal variation of the satellite retrieval may be dominated by the surroundings of the in situ site rather than the in situ value itself. In the sea ice area the concentration of the sea ice dominates the surface albedo value.

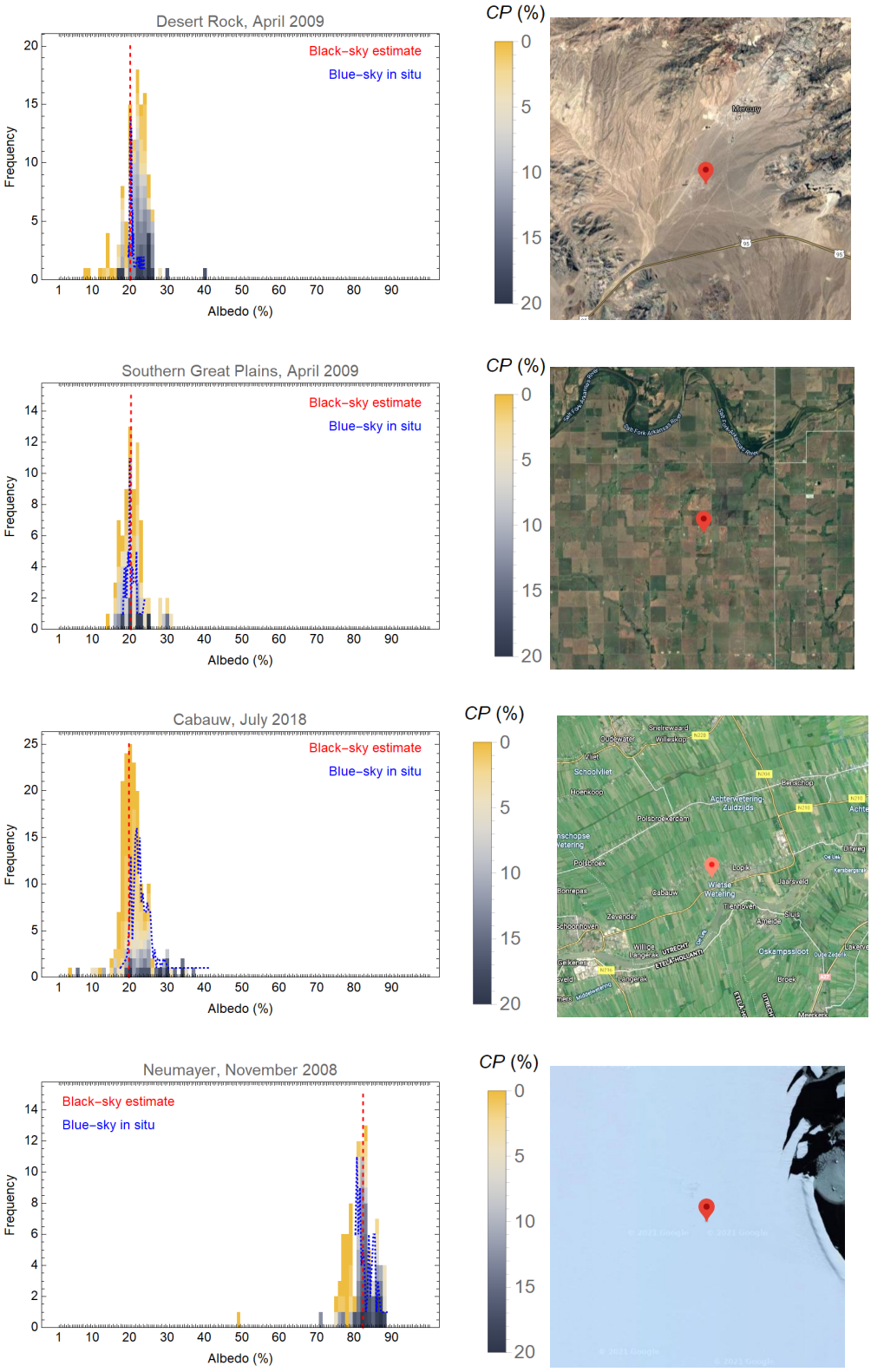

Figure 3-15: The SAL retrieval distributions at the BSRN stations Desert Rock, Southern Great Plains in April 2009 and Cabauw in July 2081 and Neumayer Station in November July 2008. The cloud probability of the satellite retrievals is indicated with the yellow-graytones. The final albedo estimates (eq. 67) are shown as dashed red lines and the in situ albedo distributions as dotted blue curves. The map (© Google Maps) shows the locations of the measurement site within a square of 10 km x 10 km.

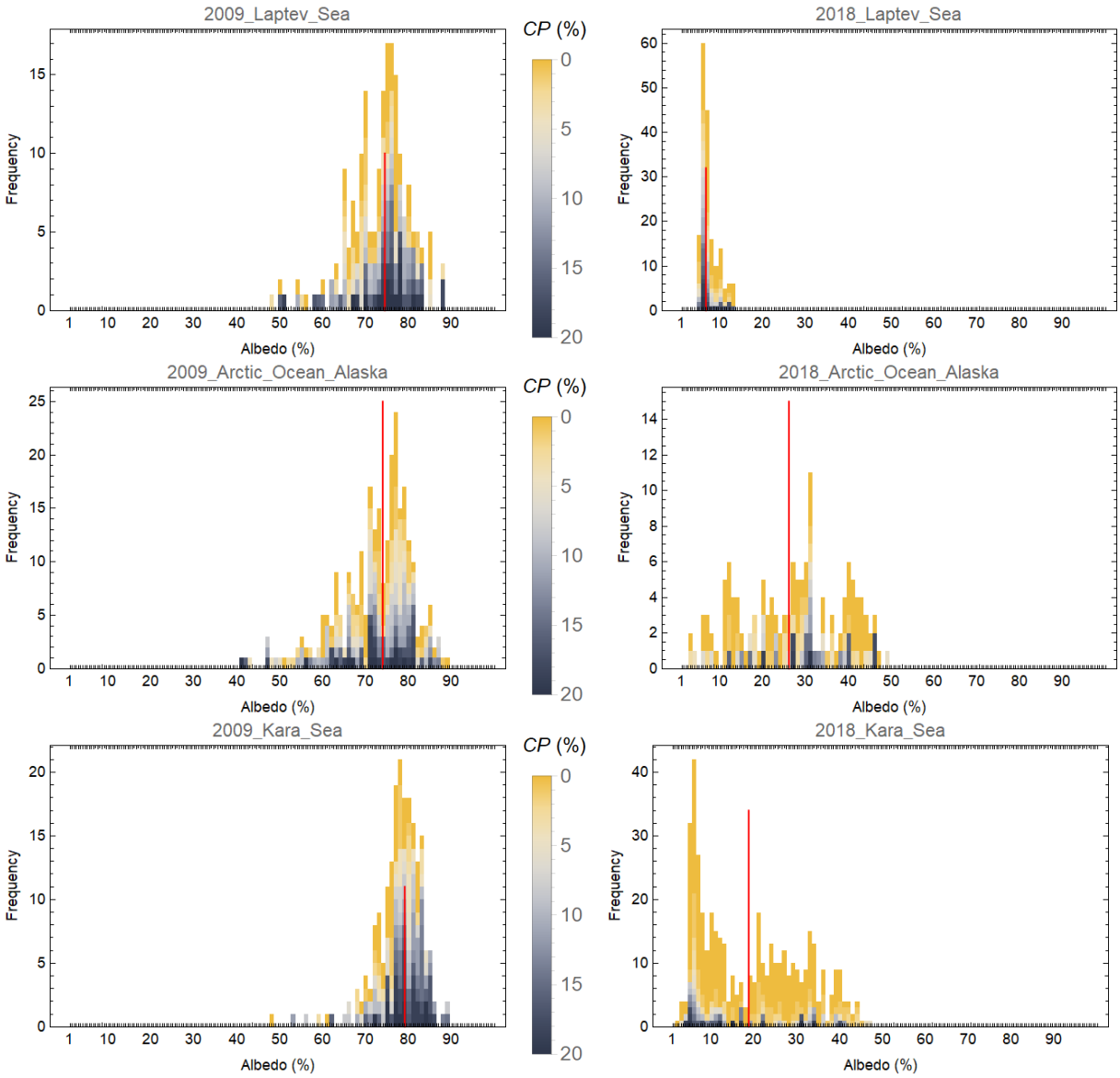

Figure 3-16: The SAL retrieval distributions at Laptev Sea (75.320°N, 125.720°E), Arctic Ocean (73.370°N, 139.180°W) and Kara Sea (2.680°N, 62.860°E) in April 2009 and July 2018. The cloud probability of the satellite retrievals is indicated with the yellow-graytones.

Table 3-9: Monthly mean black-sky surface albedo values based on AVHRR reflectance and *CP* values and the monthly means of the corresponding (satellite clear-sky overpass) times of in situ surface albedo measurements for several in situ sites (König-Langlo et el., 2013; Driemel et al., 2018). The number of observations included in the mean value are given as well as the mean distance of the satellite pixels from the in situ measurement mast.

Site	Location	Time	Number of observations	Mean distance [km]	In situ albedo [%]	AVHRR based black-sky albedo [%]
Desert Rock	36.626°N, 116.018°W	November 2008	69	3.0	21.5	20.3
		April 2009	120	3.1	20.7	20.0
		July 2018	124	2.6	20.7	21.0
Fort Peck	48.31°N, 105.1°W	November 2008	19	3.1	18.8	15.8
		April 2009	90	2.9	17.3	15.2
		July 2018	177	2.7	16.2	17.4
Payerne	46.815°N, 6.944°E	November 2008	17	3.2	24.6	17.6
		April 2009	124	3.1	23.3	21.3
		July 2018	151	2.5	21.6	19.8
Southern Great Plains	36.605°N, 97.485°W	November 2008	65	2.0	20.9	19.3
		April 2009	77	2.9	20.2	20.2
Cabauw	51.971°N, 4.927°E	July 2018	171	2.9	23.0	19.7
Syowa	69.005°S, 39.589°E	November 2008	63	2.9	81.3	80.7
Georg von Neumayer	70.65°S, 8.25°W	November 2008	80	2.6	82.3	82.8
Greenland Summit	72.580°N, 38.500°W	April 2009	79	3.1	84.4	85.4

Cloud shadows are not specifically handled, as it is assumed that the coarse GAC resolution (~5km) compensates for shadowing issues. It is possible that this assumption fails at low Sun elevation conditions, but the processing is always limited to Sun Zenith Angles below 70 degrees. Therefore, we found no need for a cloud shadow correction at this time.

The cloud mask is particularly challenged by snow and cloud delineation, unfavourable illumination conditions, and cloud detection over coast lines. The effects of classification errors will be discussed in more detail in section 4.2.

For the pixels that are classified as cloud free by PPS and are in Arctic or Antarctic Sea areas CLARA-A2-SAL algorithm uses OSI-SAF to confirm the snow/ice – no snow/ice classifications as the cloud/snow separation is particularly difficult in these areas where the Sun elevation angles are low.

The TOA reflectances of the CLARA-A3 AVHRR red and near infrared channels used for SAL retrieval are directly the output provided by PPS. In addition, the ERA-5 reanalysis-based water vapour and ozone content and the sea ice mask (of OSI SAF) are delivered to SAL processing via the PPS software.

3.7.2.2 Deriving WAL from SAL estimates

The white-sky albedo α_{white} for snow-free surfaces is derived from (Yang et al., 2008)

$$WAL = \alpha_{white} = \frac{1+1.48\ \cos\theta_z}{2.14}\alpha_{black} \quad (68)$$

where α_{black} is the black-sky albedo (SAL) and θ_z the solar zenith angle.

For snow-covered surfaces the white-sky albedo can be estimated only on monthly level from the black-sky albedo and the monthly mean white-sky albedo $\overline{\alpha_{white}}$ is derived for open areas from (Manninen et al., 2019)

$$\begin{aligned} WAL = \overline{\alpha_{white}} = \overline{\alpha_{black}}[1 \\ + \overline{\theta_z}(1.003 + 0.128\,\overline{\theta_z} - 1.390\,\overline{\alpha_{black}} + 0.0341\widetilde{\alpha_{black}} - 0.998\,\sigma_{black} \\ - 0.0155\,\gamma_{1black} - 0.000625\,\beta_{2black})] \end{aligned} \quad (69)$$

where $\overline{\alpha_{black}}$ is the monthly mean black-sky albedo and $\widetilde{\alpha_{black}}$ refers to the median, σ_{black} to the standard deviation, γ_1 to the skewness and β_{2black} to the kurtosis of the black-sky albedo monthly distribution and $\overline{\theta_z}$ is in radians.

For forested snow-covered areas the white-sky albedo monthly mean (WAL) is calculated from (Manninen et al., 2019)

$$\begin{aligned} WAL = \overline{\alpha_{white}} = \overline{\alpha_{black}}[1 \\ + \overline{\theta_z}(-0.592 + 0.709\,\overline{\theta_z} - 11.4\,\overline{\alpha_{black}} + 11.0\widetilde{\alpha_{black}} + 5.10\,\sigma_{black} \\ + 0.0204\,\gamma_{1black} - 0.0205\,\beta_{2black})] \end{aligned} \quad (70)$$

Equation (70) is further applied only if $\overline{\alpha_{black}}$ <50% to focus on sufficiently dense forests, otherwise the open snow cover equation (69) is applied. For the forested land area white-sky albedo values are still multiplied by the empirical factor (0.1 exp($\overline{\alpha_{white}}^4$)) to achieve higher values for very bright targets. For open snow-covered land and sea ice areas this additional correction is made, if

$$0.1\ \exp\left(\overline{\alpha_{white}}^4\right) < 1 + 0.01(\exp(0.003(100\,\overline{\alpha_{black}})^{1.5}) - 1) \quad (71)$$

3.7.2.3 Deriving BAL from SAL and WAL estimates

The blue-sky albedo is defined as (Lucht et al., 2000; Pinty et al., 2005; Schaepman-Strub et al., 2006; Román et al., 2010)

$$\alpha_{blue} = f_{dir}\alpha_{black} + f_{diff}\,\alpha_{white} \quad (72)$$

where f_{dir} and f_{diff} are the fractions of direct and diffuse irradiance, respectively. Theoretically the diffuse irradiance is assumed to be completely isotropic, which may not be the case in realistic clear sky conditions. In fact, deviations of several percent are possible, when the solar zenith angle value θ_z is large, even for optically thin atmosphere (Pinty et al., 2005).

In addition, the estimate of f_{diff} provided by SMAC is sufficiently accurate for atmospheric correction of reasonably clear pixels, but not for cloudy cases. Hence, another alternative was sought on the basis that f_{diff} (and hence also f_{dir}) has an essentially sigmoid statistical relationship with the clearness index, which is the fraction of the measured global irradiance to the clear sky irradiance (Hofmann and Seckmeyer, 2017). Approximating the clearness index with the cloud probability a sigmoid relationship between *CP* and f_{dir} is derived, the f_{dir} values chosen to vary in the range 0.01 (*CP* = 100%) and 0.99 (*CP* = 0%) times the value f_{dir} corresponding to θ_z = 0°. The effect of the solar zenith angle is taken into account so that the limit value at *CP* = 0% depends on the solar zenith angle. Thus, the following formula is used

$$f_{dir}(\theta_z, CP) = \frac{f_{dir}(\theta_z, CP=0)}{1 + \exp(0.0919*\mathrm{CP} - 4.5951)} = \frac{\exp(-0.1)\cos(\theta_z)}{1 + \exp(0.0919*\mathrm{CP} - 4.5951)} \quad . \tag{73}$$

Here the attenuation of the atmosphere is estimated to be that of atmosphere thickness 0.1. This assumption is considered to be reasonable as in any case estimating the direct irradiance from cloudy pixels of satellite data is rather inaccurate.

The blue-sky albedo for snow-covered areas, whether forested or not, is derived from

$$BAL = \overline{\alpha_{blue}} = \overline{f_{dir}}\,\overline{\alpha_{black}} + \overline{f_{diff}}\,\overline{\alpha_{white}} = \overline{f_{dir}}\,SAL + \overline{f_{diff}}\,WAL \tag{74}$$

where the monthly mean values of the direct and diffuse irradiance are denoted by $\overline{f_{dir}}$ and $\overline{f_{diff}} = 1 - \overline{f_{dir}}$, respectively.

4 Uncertainty and sensitivity analysis of the algorithm

4.1 Input data uncertainty

The main input data uncertainty sources are the TOA reflectance calibration (Heidinger et al., 2010; Rossow and Ferried, 2015), the cloud probability (Karlsson et al., 2020) and the geolocation (Devhastale et al., 2016; Wu et al., 2020). In addition, the land cover map may cause inaccuracy on SAL estimation of land areas (Table 4-1). The estimation of the coverage factor of these uncertainties (i.e. the comprehensiveness of the given uncertainty estimate) is difficult as most studies do not report this. TOA reflectance is given a higher factor to reflect the statistical treatments in the associated studies; for all others, coverage factor of 1 is estimated.

The accuracy of the cloud probability values is essential for the accuracy of the CLARA SAL product as the albedo values depend on them directly. While the current probability values are in general reliable, the user should be aware that there is a higher risk that the cloud probability accuracy affects CLARA SAL in coastal areas and over snow-covered rough terrain, especially when the sun elevation is low.

The geolocation accuracy is very important at surface discontinuities with very different albedo values, for example at shorelines, where the water is not frozen, but there is snow or very bright sand on the ground.

The surface reflectance retrieval contains also a random risk due to fauna. Large gatherings of animals (birds, antilopes, reindeer etc.) inevitably mask the ground reflectance. Flying flocks of birds or insects may not typically cause serious problems at pixels of nadir view, but the larger is the satellite view angle, the larger is their effect on the pixel reflectance and only middle pixel has nadir view. In addition, an improbable but possible failure of the cloud probability retrieval could result in a large error anywhere, as snow/hail precipitation can take place anywhere, so that no pixel can be considered false because of being very bright. However, the effect in temporal means at the SAL grid cell resolution level is typically very small.

Table 4-1: Uncertainty estimates for input data used for SAL retrieval and their effect on SAL accuracy.

Parameter	uncertainty	SAL	Coverage factor for uncertainty
TOA reflectance calibration	Δ_{TOA} = 3 - 5%	~ Δ_{TOA}	2
Cloud probability	Δ_{CP} to be assessed by SMHI	~ exp(-0.1Δ_{CP})	1
AVHRR geolocation	2.5 – 7 km	random	1
LUC uncertainty	misclassification	0 - 5% (on land)	1

Since SAL is used as input for WAL and BAL, they will also have all the uncertainty sources of SAL.

4.2 Uncertainty budget estimates

Due to the complex, multistage computation process required to obtain the surface albedo product, there are several sources of uncertainty that may propagate through the production chain. The sources of uncertainty and their estimated relative effect is shown in Table 4-2. It should be stressed that the values are estimates based on the algorithm literature and simulations of the behavior of the CLARA SAL code with input data modified to reflect sources of inaccuracy. Information on the actual achieved accuracy is obtainable from the Validation Reports of prior CLARA SAL data records.

Table 4-2: Estimates of uncertainty sources and their effects on the observed CLARA SAL product. All values are in relative albedo (percent).

Source of uncertainty \ Instrument and scene type	AVHRR land	AVHRR Snow & ice
uncertainty caused by SMAC coeff. and aux-data	<0-4% (over desert 0-8%)	0-4% (assumed)
BRDF uncertainty	0-5%	unknown
NTBC uncertainty	0-10%	0-10%
Total	0-24% for the known sources of uncertainty	0-14% for the known sources of uncertainty
Over desert	0-28%	

The SMAC coefficients used for atmospheric correction are different for continental areas and desert due to the heavy aerosol loading over desert areas. In addition, to be fully accurate SMAC requires pixelwise data on water vapor content, integrated ozone amount, AOD at 550 nm, and pressure at surface level. This release of CLARA SAL has access to the water vapor, ozone, surface pressure and AOD data on a continuous basis. (Note that the AOD data for 2015-2020 is a climatology.)

Proud et al. (2010) has proposed a correction to the SMAC algorithm for SEVIRI. Their study results showed that the SMAC algorithm for SEVIRI may suffer from considerably low accuracy when the solar zenith angle over a scene exceeds 30 degrees. Their proposed changes to the algorithm add only a minor additional CPU load, while improving the correction results over their African test sites. They also state that a similar correction would improve the SMAC accuracy on other instruments. Based on the results of their study, CLARA SAL users should also be aware of additional potential uncertainties within the SMAC correction algorithm.

The land use classification information is needed by several CLARA SAL processing steps to assign BRDF kernels and distinguish between ocean and permanent snow/ice areas, among other things. Man-made changes in LUC may cause poor matches between assigned BRDF and actual reflectance behavior, resulting in uncertainty in the retrieved albedo. Oceans, barren areas and snow/ice do not generally suffer from man-made changes for obvious reasons, but other misclassifications such as cropland portrayed as forest due to an outdated LUC dataset may occur. We have studied the computed albedo changes resulting from different LUC datasets, and the results indicate that the uncertainty is in the order of 0 - 5 % relative for land surfaces. In CLARA-A1 a single LUC dataset was used for the 27-year period. Therefore larger regional differences may be found as natural and man-made changes in the landscape occur. In CLARA-A3 four additional LUC datasets have been used. We presume that the errors caused by LUC datasets are therefore smaller in CLARA-A3 than they were in CLARA-A1.

BRDF errors are a potential factor in the retrieval accuracy of CLARA SAL. Incomplete understanding of the reflectance properties of natural targets is a difficult thing to estimate, so the range of probable inaccuracy for this factor is also large enough to be considered. The values obtained for the estimated error are from the relevant algorithm publications using typical surface broadband albedo values.

Inaccuracies may also arise from the need to compress the LUC dataset classes into the internal CLARA SAL LUC types, as in Table 3-4. This likely causes some BRDF inaccuracies for different forest types or marshlands. However, over the generally heterogeneous 0.25 degree resolution of the end user products their contribution is estimated to be minor.

Because the BRDF correction for snow is treated with an empirical temporal averaging scheme, the under- or overestimations of individual CLARA SAL retrievals is very difficult to estimate. The overall accuracy of CLARA-A1 SAL algorithm for snow albedo retrievals over the Greenland Ice Sheet and Arctic Ocean in 2007 has been discussed in a publication by Riihelä et al. (2010). They found the overall accuracy of CLARA SAL over snow surfaces to be between 5-10% (relative) in most cases where drastic snowmelt or topography did not degrade the algorithm performance. The treatment of snow-covered pixels has not changed in CLARA-A3 SAL. Therefore we presume that these figures are still up to date. More details on the CLARA SAL behaviour over snow and ice may be found in Riihelä et al. (2013) and Karlsson et al. (2017).

The Narrow-to-Broadband-Conversion (NTBC) inaccuracies listed here are derived directly from the publications describing the algorithms. The interested reader should see Xiong et al. (2002), and Liang (2000) for details.

This release of CLARA SAL is not normalized for a common Sun Zenith Angle for land and snow/ice surfaces. While this does not constitute a retrieval error in itself, the products will show a somewhat larger degree of variability in the temporal means as a result. The variability is typically on the order of 0.01 to 0.02.

A similar topography correction as in CLARA-A1 has been applied to CLARA-A2. There is currently insufficient data to estimate the effectiveness of the correction, therefore we do not offer such numbers here. Based on the theoretical studies (see sections 3.3.1 and Appendix A for discussion), we expect at least a 10% (relative) improvement in accuracy over

mountainous areas (over 5 degree mean slope). The true effect will be studied in future validation work.

The uncertainty of WAL and BAL besides those of SAL are related to the white-sky albedo retrieval methods and the estimation of the fraction of diffuse irradiance. The white-sky albedo estimation method by Yang et al. (2008) and Manninen et al., (2019) uncertainty is given in Table 4-3. The estimation accuracy of the diffuse irradiance fraction (Hofmann and Seckmeyer, 2017) is given in Table 4-4.

Table 4-3: Estimates of uncertainty sources (not already included in retrieval of SAL) and their effects on the observed CLARA WAL product. All values are in relative albedo (percent).

Source of uncertainty \ Instrument and scene type	AVHRR snow-free land	AVHRR Snow & ice
white-sky albedo estimation method	< 4%	not forested < 4% forested ~6%

Table 4-4: Estimates of uncertainty sources (not already included in retrieval of SAL and WAL) and their effects on the observed CLARA BAL product. All values are in relative albedo (percent).

Source of uncertainty \ Instrument and scene type	AVHRR
diffuse irradiance fraction estimation method	RMSE = 0.116

4.3 AOD sensitivity analysis

AOD is the dominating part of the atmospheric correction. It is also a highly dynamic parameter that varies both diurnally and seasonally. Therefore, it should be derived simultaneously with the albedo. However, AVHRR data has only one visible and one NIR channel available consistently. Hence, it is not possible to derive both aerosol and broadband surface albedo values from one AVHRR image. As SAL is provided only in monthly and pentad level the complication of using an AOD time series that is not simultaneous with the AVHRR retrievals is smoothed out by the large number of observations used for the monthly and pentad albedo means. As long as the AOD level represents well the time window in question, it should provide reasonable results.

The effect of AOD is naturally more pronounced for large solar and satellite view angles, as the path in the atmosphere is then long. For this reason, those angles are limited to 70° and 60°, respectively, in SAL retrieval. Luckily, the AOD tends to be smaller close to the poles, where the sun zenith angle is always relatively large. Yet, even in the Arctic there is

occasionally remote transportation of aerosols. These transient events do not generally dominate longer temporal aggregates of satellite observations.

The effect of aerosols on surface albedo is based on their scattering characteristics. When aerosol concentration is low, molecular scattering and absorption dominates. As the aerosol concentration increases, either aerosol scattering processes dominate (over dark targets) or aerosol absorption dominates (over bright targets) (Kaufman and Tanré, 1996). Thus the correction will either increase or decrease the corrected surface reflectance relative to the TOA reflectance. Over a bright target such as a desert, the correction increases the surface reflectance to compensate for the dominant absorption effect, and vice versa over darker vegetation targets at visible wavelengths. The viewing geometry also plays its role, as the atmospheric path length increases when SZA and/or VZA are large and the correction becomes larger. The relative azimuth angle between Sun and observer is also important, as the scattering processes between sunlight and atmospheric constituents have anisotropic characteristics. More specifically, molecular backscattering is very weak, whereas aerosol backscatter is relatively much stronger. Both scattering processes prefer small scattering angles, leading to the “wave-like” structure of the correction magnitude (see ATBD for CLARA-A1 SAL for more details). As mentioned, the aerosol effects become dominant over molecular scattering at large AOD, which is why the rate of change in the correction magnitude is of opposite signs in the forward and backscattering directions.

For CLARA-A2 we developed an AOD time series that is based on AI values from TOMS and OMI instruments (Jääskeläinen et al., 2017). It is continued to cover the years 2015-2020. This dataset is used as input for the SMAC algorithm. The annual global mean AOD of land areas (for SZA $\leq 70°$) derived from the CM SAF TOMS/OMI based AOD time series for 1980 - 2020 is about 0.3. The monthly distributions for 2010 are shown in Figure 4-1. Obviously the aerosol distributions are dominated by the larger land areas of the northern hemisphere, since the larger aerosol values occur during the growth season of that area. Since the goal is not to derive an AOD product, but to carry out atmospheric correction in order to derive the surface reflectance from TOA reflectance values, the derived AOD is optimized for that. I.e. its accuracy is best for AOD range 0 – 1 and the SZA $\leq 70°$ and it is derived only for land areas without snow. For that reason, it provided better surface reflectance estimates than high quality AOD products (Jääskeläinen et al., 2017).

To assess the effects of applying a daily aerosol input in the atmospheric correction, we have performed a sensitivity study. In the following sections we will assess first the sensitivity of SMAC algorithm for changing AOD values and secondly the effect of changing AOD values to SAL values, including the use of daily AOD data. A more thorough analysis on the effect of AOD on surface albedo can be found in Manninen et al. (2013).

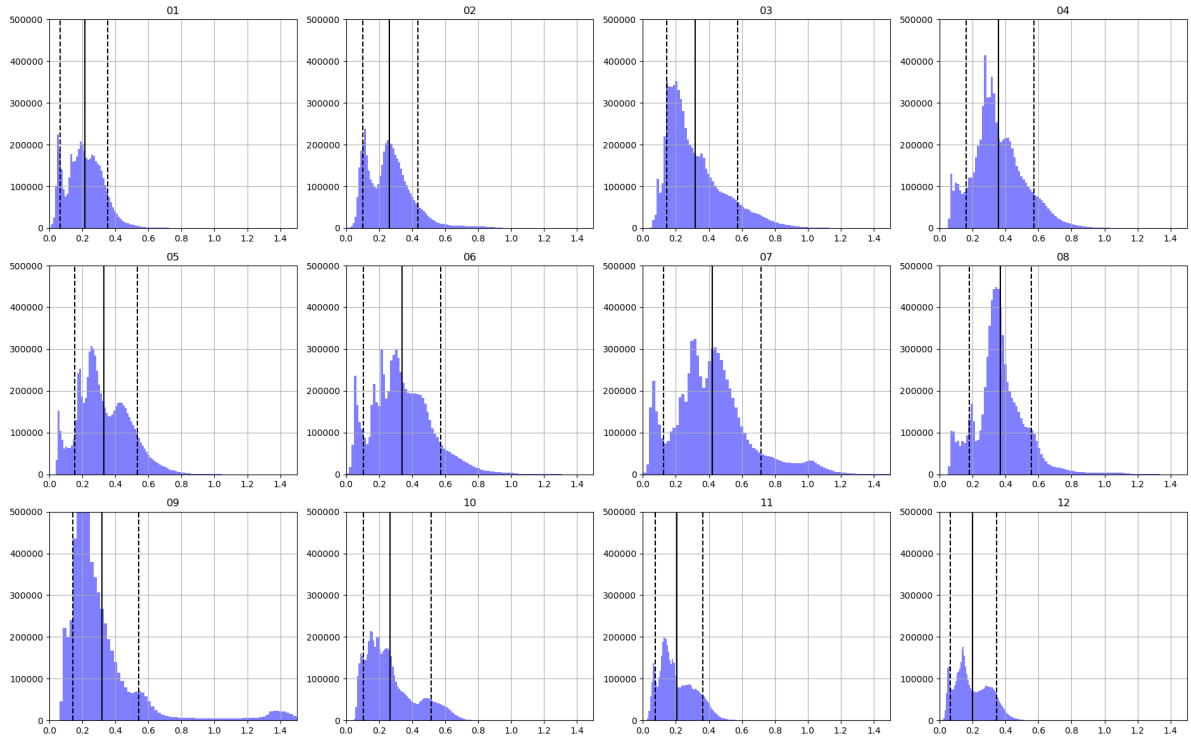

Figure 4-1: The monthly AOD distributions in 2010 of the global AOD data set based on TOMS/OMI time series used for atmospheric correction in SAL retrieval. The mean values are indicated by solid vertical lines and the 10% and 90% quantiles with dashed vertical lines.

4.3.1 SMAC atmospheric corrections sensitivity analysis

In the following, the effect of the SMAC atmospheric correction with different values for AOD, sun and satellite angles and vegetation parameters on simulated albedo will be studied. The analysis will be divided into two cases: moderate and extreme values for satellite and sun zenith angles. The moderate angles are: sun zenith angle 40°, satellite zenith angle 20°, sun azimuth angle 180° and satellite azimuth angle 260°. The extreme angles are: sun zenith angle 60°, satellite zenith angle 50°, sun azimuth angle 180° and satellite azimuth angle 260°. The water vapor pressure is 2.5 g/cm^2, ozone 0.35 atm-cm^2 and pressure at surface level 1013 hPa. The data is analyzed separately for four different land use classes: barren, forest, cropland and grassland.

The effect of changing AOD value on VIS and NIR albedos of barren ground, grassland, forest and cropland are shown in Figure 4-2 to Figure 4-9 with different TOA reflectances using moderate and extreme sun and satellite angles. The TOA reflectances for different land use types other than barren have been selected so that they give NDVI between 0.2 and 0.8. Note that in these figures, albedo is represented in range 0…1 instead of 0.100% as elsewhere in this ATBD.

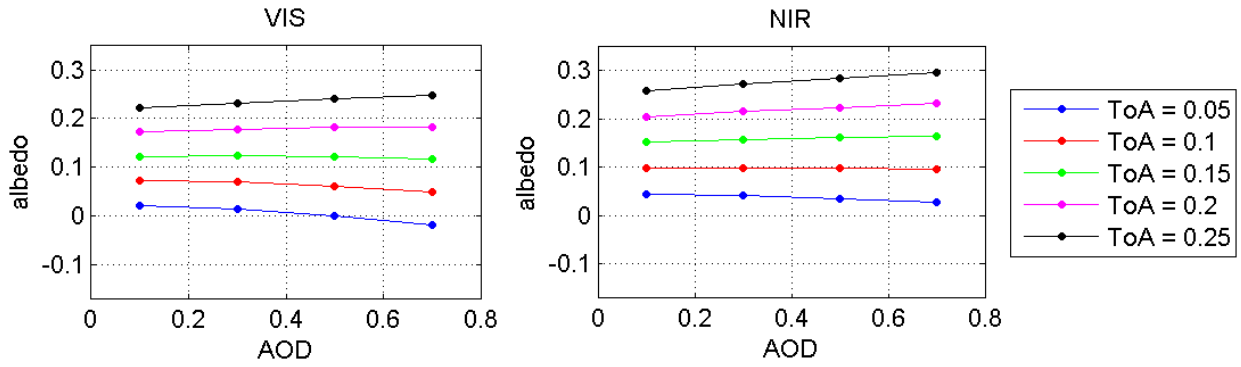

Figure 4-2: The sensitivity of VIS and NIR albedos of barren ground on changing AOD for different TOA reflectances using SMAC with moderate angles.

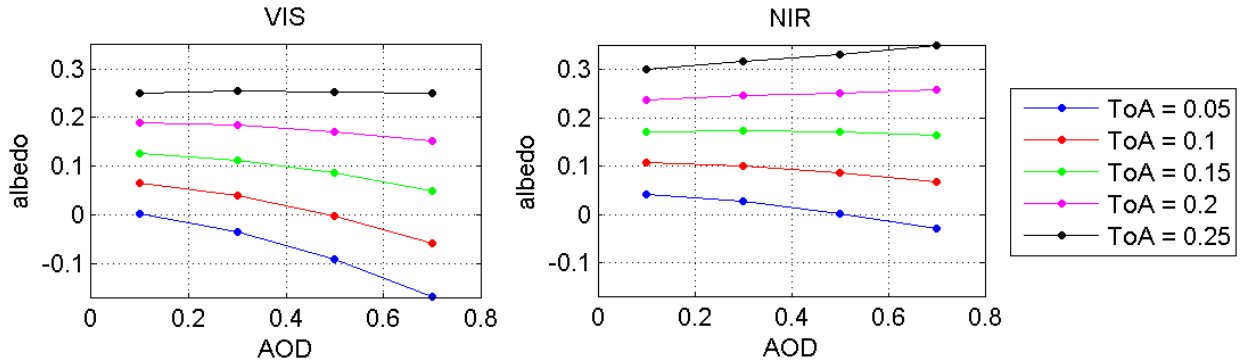

Figure 4-3: The sensitivity of VIS and NIR albedos of barren ground on changing AOD for different TOA reflectances using SMAC with extreme angles.

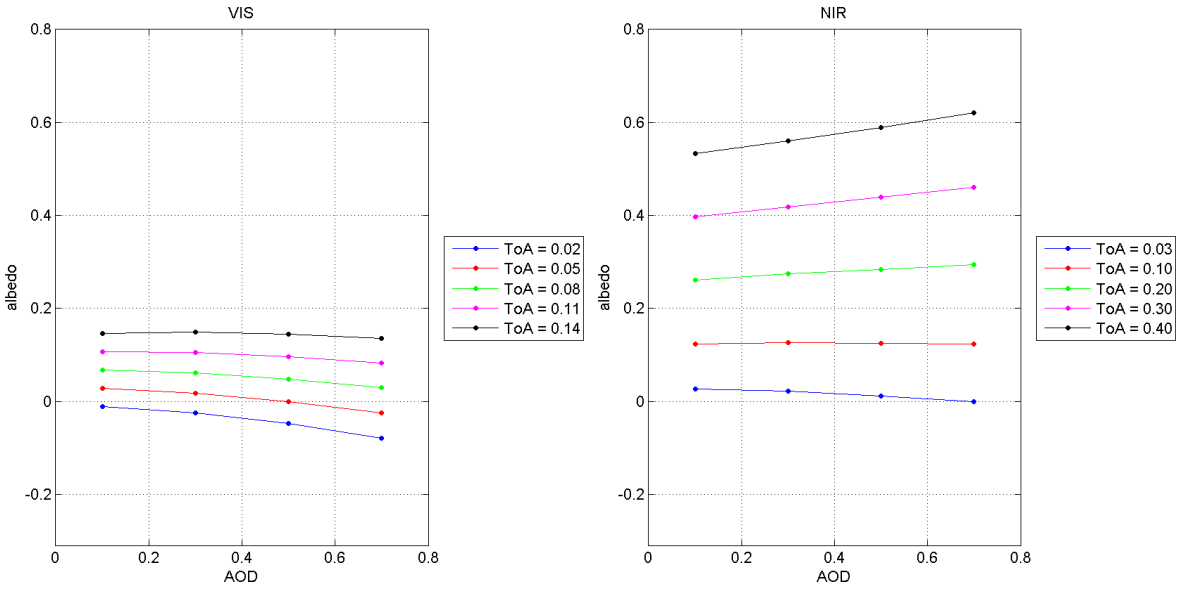

Figure 4-4: The sensitivity of VIS and NIR albedos of cropland on changing AOD for different TOA reflectances using SMAC with moderate angles.

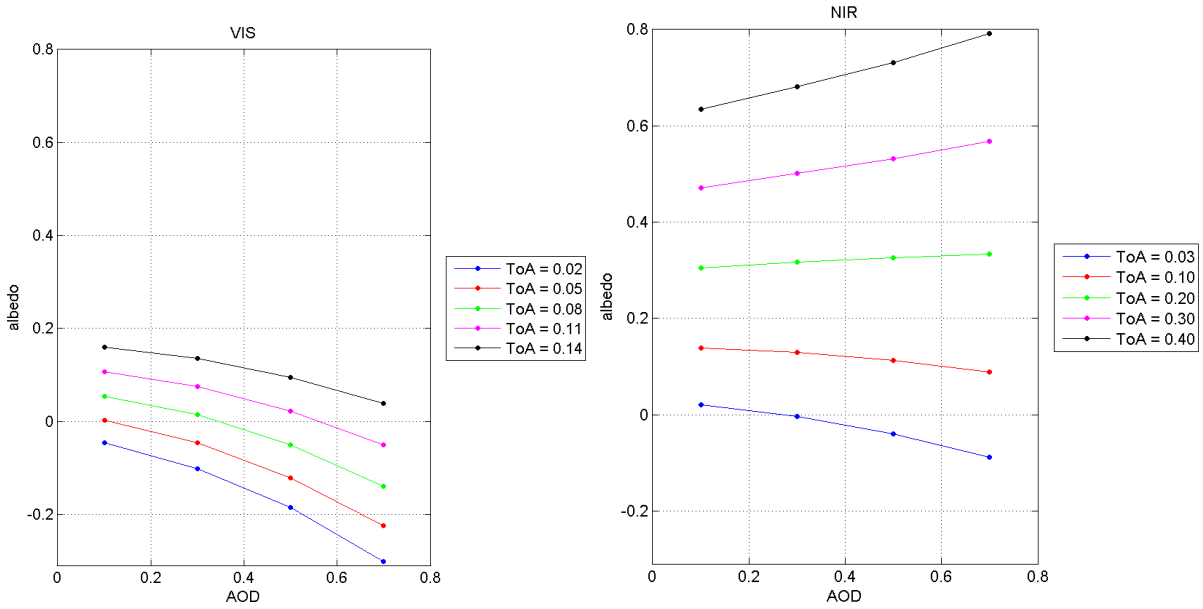

Figure 4-5: The sensitivity of VIS and NIR albedos of cropland on changing AOD for different TOA reflectances using SMAC with extreme angles.

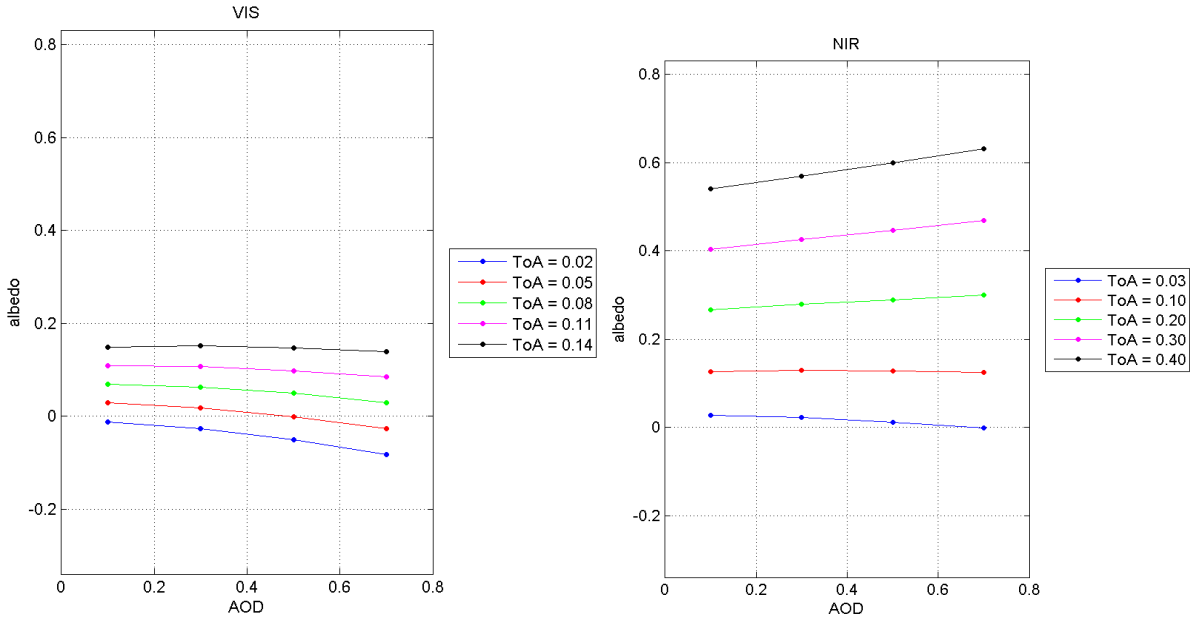

Figure 4-6: The sensitivity of VIS and NIR albedos of forest on changing AOD for different TOA reflectances using SMAC with moderate angles.

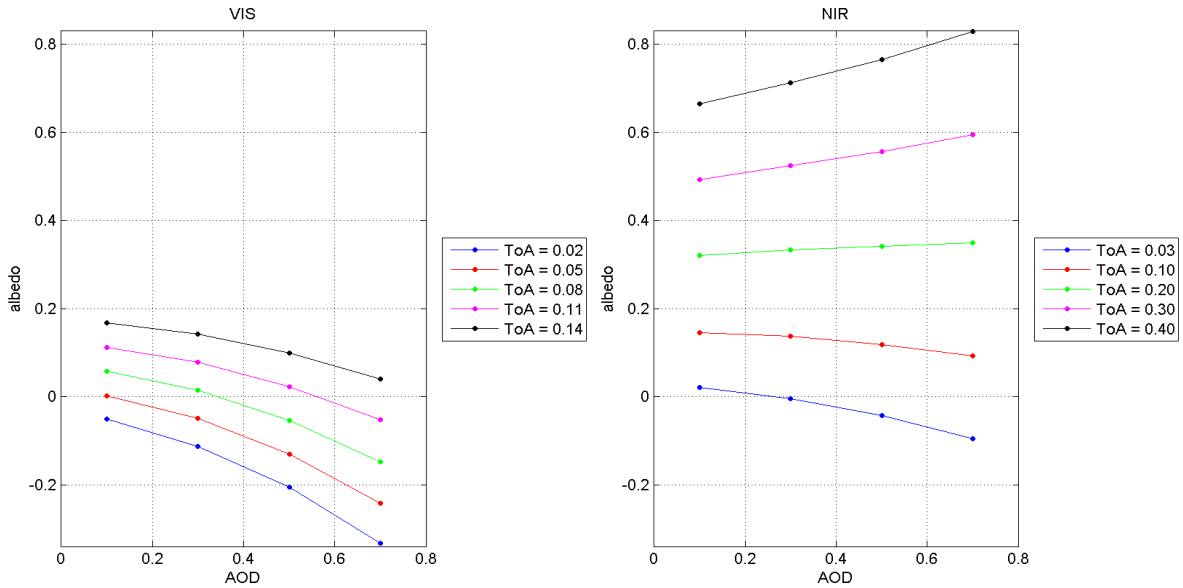

Figure 4-7: The sensitivity of VIS and NIR albedos of forest on changing AOD for different TOA reflectances using SMAC with extreme angles.

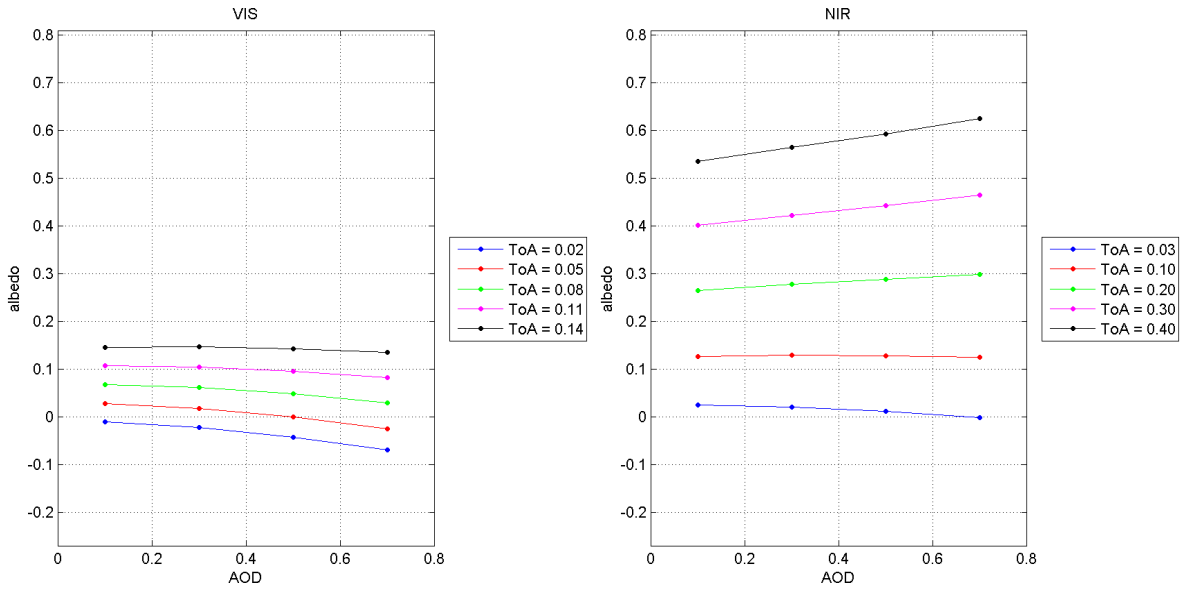

Figure 4-8: The sensitivity of VIS and NIR albedos of grassland on changing AOD for different TOA reflectances using SMAC with moderate angles.

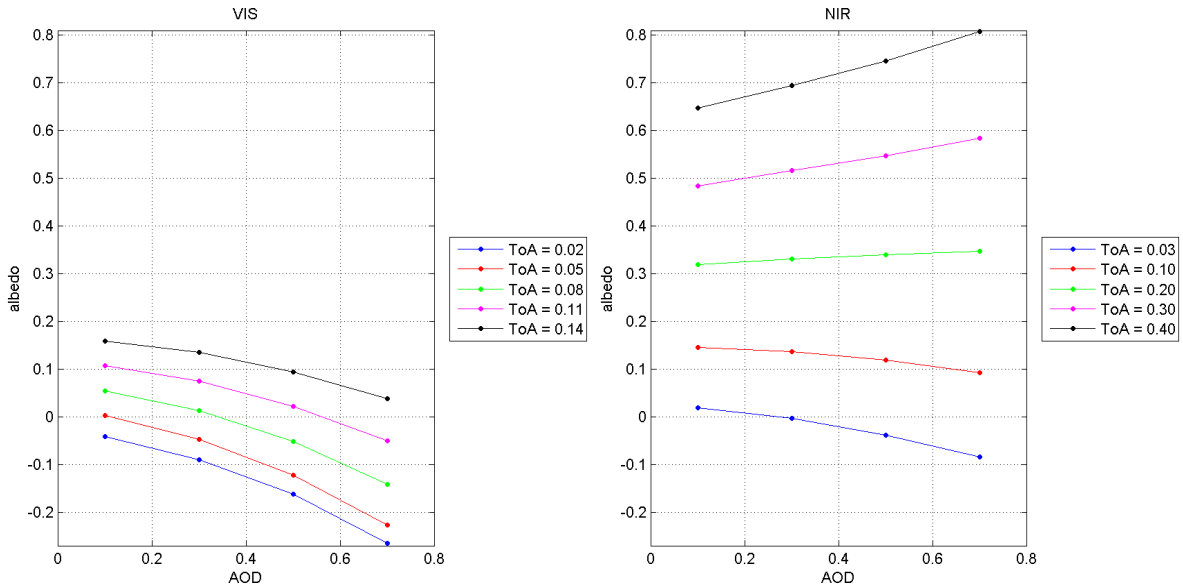

Figure 4-9: The sensitivity of VIS and NIR albedos of grassland on changing AOD for different TOA reflectances using SMAC with extreme angles.

The NIR albedo is more sensitive to the change in AOD for all land use types than VIS albedo. For VIS albedo the increase in AOD leads to lower albedo values with all TOA reflectances and land use types, whereas with high

4.3.2 SAL albedo values sensitivity to change of AOD

The sensitivity of SAL algorithm on the AOD values has been studied using two overpasses: NOAA-18 overpass (noaa18_99999_20080620T1257010Z) from 20th June 2008 Covering North Western Africa, and Metop-image (metop02_20090415_1004_12910) from 15th April 2009 covering Western Europe. The analysis has been made for the parts of the overpasses covering the largest land area visible in the overpass. The sea and ice sheet surfaces have been excluded from the analysis. The sensitivity of the SAL values to AOD has been studied by calculating SAL values using static AOD values of 0.1 (also used in CLARA-A1), 0.3 and 0.5. For comparison a test data using the daily AOD data of CLARA-A2 has been calculated.

CASE STUDY 1: Europe

Figure 4-10 shows the SAL values of the test area in Europe calculated using the different AOD values. Other input parameters have been kept the same. The mean and standard deviation of the SAL values are shown in Table 4-5. The sea and no data pixels have been excluded from the analysis.

The effect of change in AOD is less than 2 % units in this study area, where the albedo values are low. The higher value of AOD seems to lower the mean and standard deviation of the albedo, with the effect of the daily AOD dataset being somewhere between the AOD values 0.1 and 0.3.

The absolute changes caused by the different AOD values as compared to AOD being 0.1 (as in CLARA-A1) are shown in Figure 4-11 and the mean and standard deviation of the changes in SAL values related to the change in AOD values are shown in Table 4-6. The change in the albedo values seem to be largest in the areas where the albedo is the highest. In this case the biggest changes are in the Alps. This can also be seen in Table 4-7, which shows the mean absolute change in SAL values related to changes in AOD values at different albedo levels. Again the overall effect of the daily albedo seems to be less than that of AOD value 0.3.

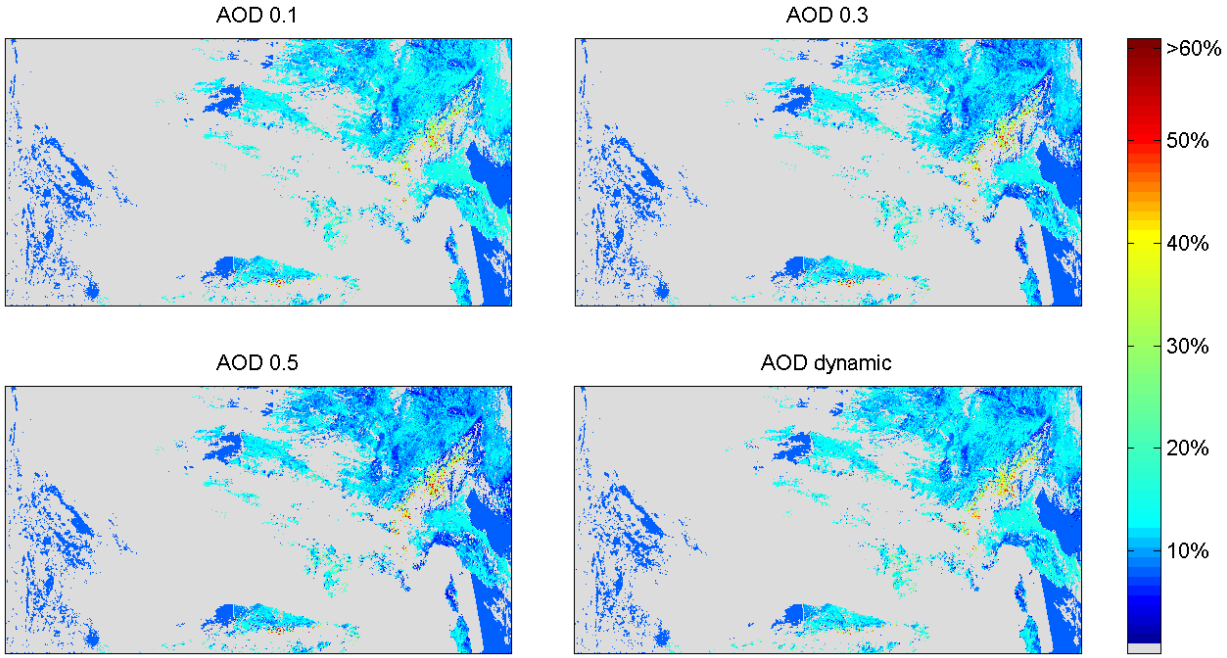

Figure 4-10: SAL values of Europe using AOD values of 0.1, 0.3, 0.5 and daily AOD. The islands of Sardinia and Corse are at the lower right corner.

Table 4-5: Mean and standard deviation of the SAL values of the test area (Europe) using different AOD values.

AOD	Mean	STD
0.1	12,89	4,50
0.3	12,20	4,93
0.5	11,62	5,28
Daily	12,54	4,75

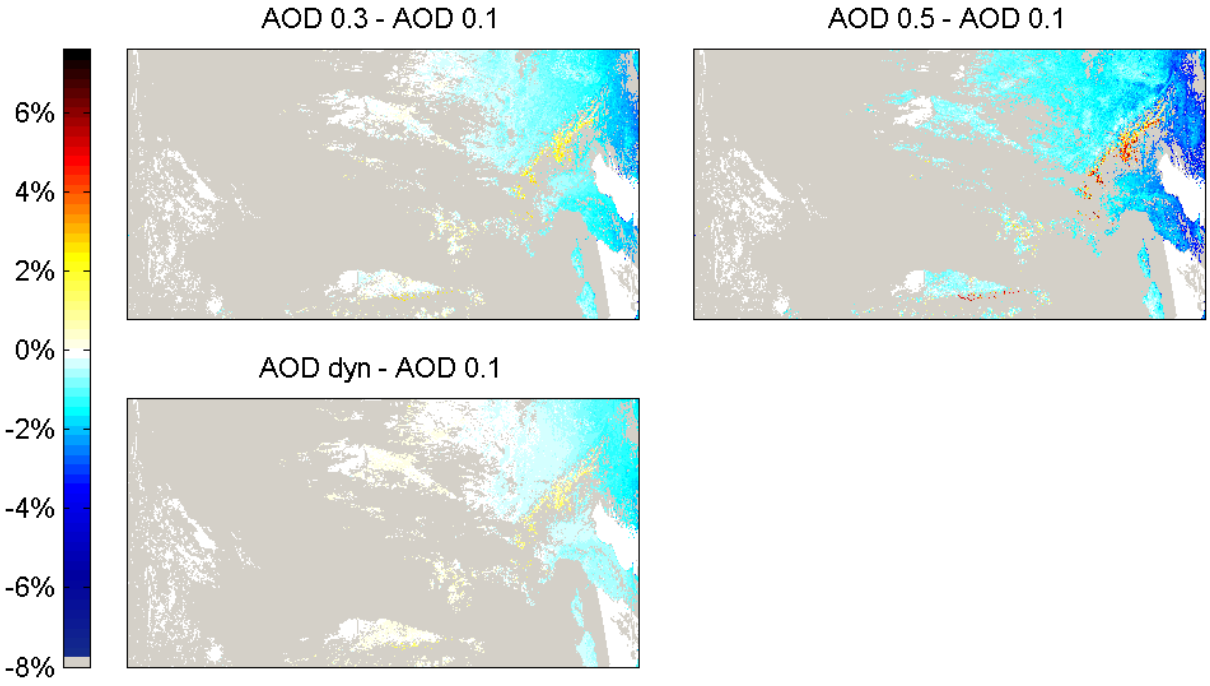

Figure 4-11: The absolute change in SAL albedo values in Europe between 0.3->0.1, 0.5->0.1 and daily->0.1. The pixels without data are marked with grey.

Table 4-6: Mean and standard deviation of the change in SAL values caused by the change in AOD value in Europe.

Abs. diff.	Mean	STD
0.3 – 0.1	-0,691	0,775
0.5 – 0.1	-1,270	1,158
Daily – 0.1	-0,348	0,488

Table 4-7: The mean absolute difference in SAL values for different levels of albedo in Europe.

Albedo	0.1 -> 0.3	0.1 -> 0.5	0.1 -> Daily
1-30	-0,73	-1,35	-0,36
30-50	1,95	3,98	1,06
50-70	2,96	6,14	1,60
>70	4,18	8,70	2,25

CASE STUDY 2: North Western Africa

The NOAA-18 test area in North Western Africa with SAL values calculated using the different AOD values are shown in Figure 4-12. Other input parameters have been kept the same. The mean and standard deviation of the SAL values are shown in Table 4-8. The sea and no data pixels have been excluded from the analysis.

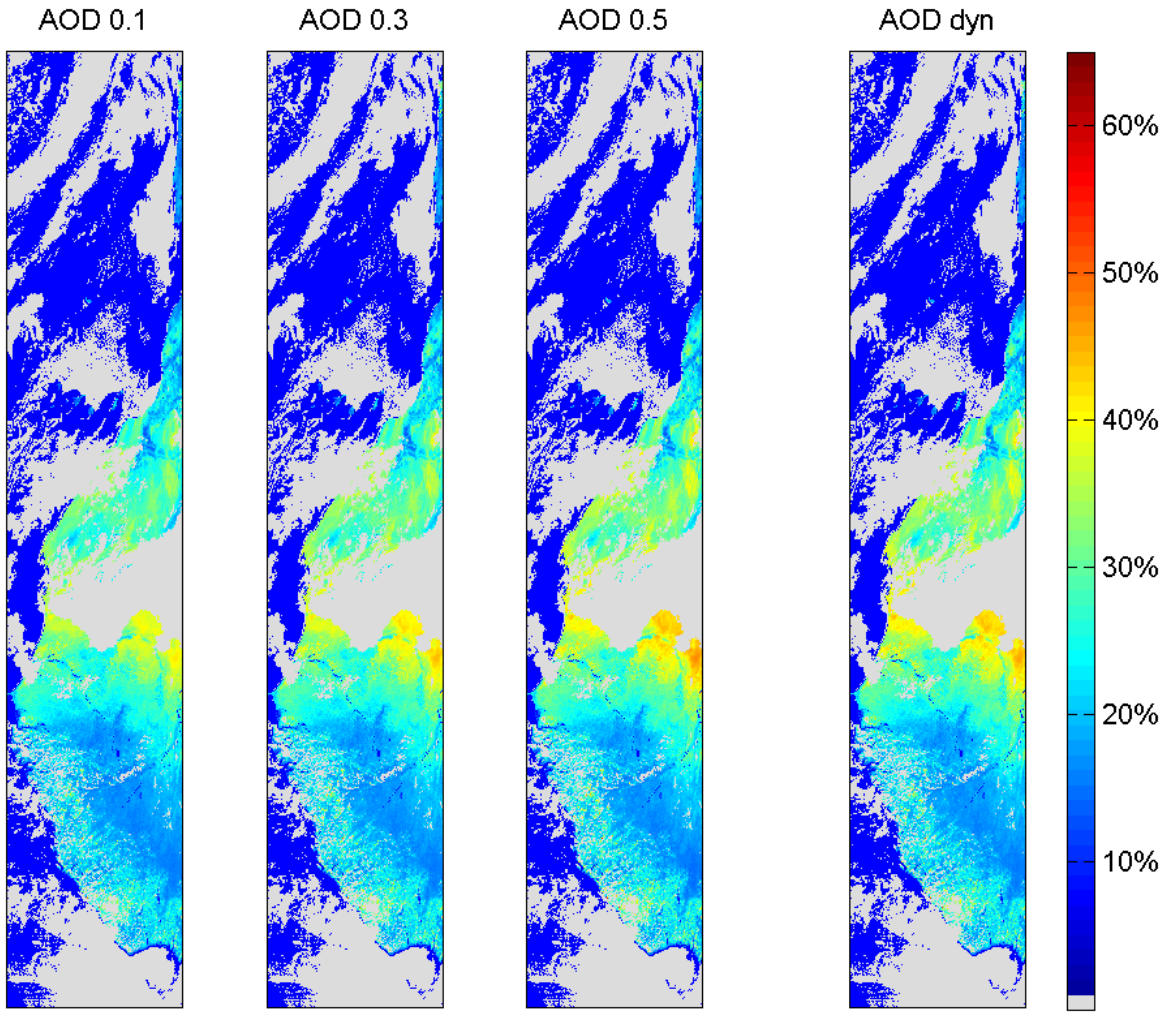

Figure 4-12: SAL values of North Western Africa using different AOD values. SAL value 0 represents pixels without data.

Table 4-8: Mean and standard deviation of the SAL values of the test area using different AOD values.

AOD	Mean	STD
0.1	24,14	6,10
0.3	25,17	6,61
0.5	26,03	7,26
Daily	25,80	7,15

The study area has much higher albedo values as compared to Europe. Therefore the higher AOD values have an increasing effect on the calculated albedo. Also the AOD values are typically higher in this area than in Europe, hence the effect of the daily AOD value is between the effects of AOD values 0.3 and 0.5. The standard deviation is also higher here than in Europe.

The absolute change caused by the different AOD values as compared to AOD being 0.1 (as in CLARA-A1) are shown in Figure 4-13 and the mean and standard deviation of the changes in SAL values related to the change in AOD values are shown in Table 4-9. In this study area the increasing AOD value constitutes to higher albedo values. This is to be expected for areas of high albedo. The effect of the daily AOD dataset is something between the AOD values 0.3 and 0.5. The mean absolute difference in SAL values for different albedo levels with given the changes in AOD values are shown in Table 4-10.

Table 4-9: Mean and standard deviation of the change in SAL values caused by the change in AOD value.

AOD difference	Mean	STD
0.3 – 0.1	1,033	0,528
0.5 – 0.1	1,891	1,201
Daily – 0.1	1,665	1,118

Table 4-10: The mean absolute difference in SAL values for different levels of albedo.

Albedo	0.1 -> 0.3	0.1 -> 0.5	0.1 -> Daily
10-30	0,868	1,518	1,305
30-50	1,785	3,583	3,295
50-70	2,687	5,489	3,242
>70	-	-	-

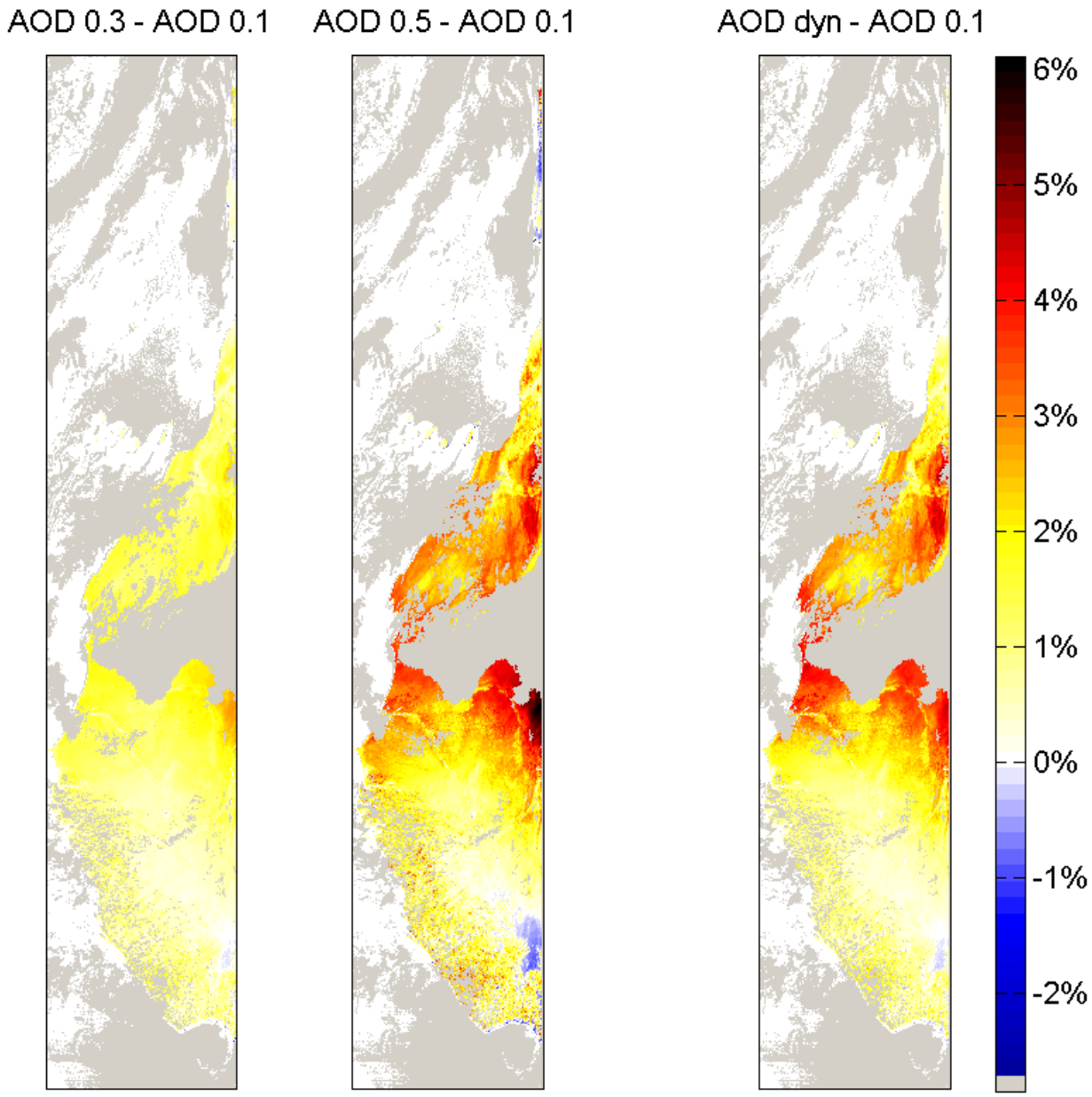

Figure 4-13: The absolute change in SAL albedo values between (from left to right) 0.3->0.1, 0.5->0.1 and daily->0.1. The pixels without data have been marked with grey.

5 Assumptions and limitations

This chapter summarizes the main points concerning the assumptions and limitations of the algorithm. For details on the issues, the reader should see the previous section on error budget.

5.1 Assumptions and mandatory inputs

One of the main assumptions of the CLARA SAL algorithm is that the cloud probabilities are reliable. Also, beside normal sanity checking, the input data is not monitored for large variations between overpasses or other signs of anomalous behavior. On the other hand, because of the large change in surface albedo during snowfall, a change monitoring tool would be challenging to implement while considering the fact that some large and sudden variations in albedo are natural.

The algorithm inherently assumes that the land use classification information is always accurate, and that the BRDF models work equally well in all geographical areas and during all seasons. This may not always be the case.

The mandatory inputs for the algorithm are

- Red and NIR channel TOA reflectances (AVHRR/SEVIRI ch. 1 & 2)
- Sun Zenith Angles
- Satellite Zenith angles
- Relative Azimuth angles between Sun and the satellite / Separate Sun and Satellite Azimuth angles required for reliable topography correction computation
- Cloud probability map / binary cloud mask (backup, not used in CLARA-A3)
- Cloud identification quality data
- Land cover data
- SMAC atmospheric correction coefficients

5.2 Constraints and limitations

CLARA SAL computation is dependent upon low cloud probability (≤ 20 %) (Karlsson et al., 2020) and appropriate Sun-satellite geometry. The existence of high cloud probability precludes robust surface albedo retrieval and therefore such areas are masked out. As for the sun-satellite geometry, the atmospheric and BRDF corrections become unreliable when either the Sun or the satellite are too low over the horizon. Therefore, CLARA SAL computation is limited to times when the Sun zenith angle < 70 degrees and the satellite zenith angle < 60 degrees.

Ocean albedo is also currently not taking into account the changes in chlorophyll content. However, already for the CLARA-A2 version a wind speed time series was added as an input value, which improves the accuracy of the albedo values over oceans as compared to CLARA-A1. The CLARA-A3 uses the same (extended) wind speed time series as CLARA-A2.

The accuracy of the cloud probability is critical to the SAL product quality. Cloud probability overestimation is not a problem since the weekly and monthly SAL end products generally have sufficient sampling to compensate. However, underestimation of cloud probability may lead to sporadic observed surface albedo retrieval overestimations. Over snow-covered areas, the underestimation of cloud cover typically leads to an underestimation of the observed surface albedo. The end products are resistant to such effects because they are the result of averaging of observed products, leading to mitigation of sporadic errors.

The current atmospheric correction is a compromise between the need to avoid introducing artificial retrieval errors into the product and a desire to correctly account for the atmospheric physics affecting the surface albedo retrieval. We currently use an atmospheric model to account for the second-order atmospheric variables that affect surface albedo retrievals, namely columnar water vapor, ozone content and surface pressure. However, the most important atmospheric variable affecting the surface albedo retrievals is the aerosol optical depth (AOD) in the atmosphere. Variations in AOD are both regional and global; their effect in space-observed surface reflectances may be substantial.

An accurate derivation of AOD from satellite observations to support surface albedo retrievals requires assumptions on the albedo of the underlying surface. Through making these assumptions, the product contains an internal correlation between the AOD and the albedo of the terrain underneath, which is an undesired combination. The surface albedo used in the AOD time series of CLARA-A3 SAL is independent of the SAL-albedo. Though additional albedo retrieval errors will occasionally occur as a result, we make this choice consciously in order to preserve the trend analysis capabilities of the CLARA SAL product.

One may also attempt to solve the aerosol-albedo problem by a simultaneous retrieval of both quantities. Such a method has been proposed and implemented for MSG/SEVIRI by Govaerts et al. (2010) as well as for MODIS by Strahler et al. (1999). While proven effective (Wagner et al., 2010), the technique requires a large amount of daily observations for each retrieval location and is computationally fairly expensive. It also assumes that the land cover within the pixel is homogeneous, which is not typical of the GAC pixel size. Therefore we do not attempt to implement a similar procedure for CLARA SAL. In addition, combining topography correction and simultaneous aerosol-albedo problem might not be realistic, as the topography correction is already such a heavy task that neighbour pixel interaction can’t be taken into account.

Errors in the land use classification data are another source of retrieval error that should be considered. The LUC data is not continuously updated, therefore man-made or natural changes in land cover are generally not correctly picked up by CLARA SAL, which is dependent on LUC data to choose a proper surface albedo subroutine. A known location where errors do occur is the ablation zone in West Greenland for Arctic SAL. There rough terrain, ice flows and progressing snow melt in summer seasons cause the LUC classification to be inaccurate, leading to major retrieval errors. The deserts land cover class has been added to the oldest LUCs assuming them to be the same as later, which causes still some inaccuracy

in desert areas. Since the CLARA SAL dataset covers about 40 years in time, inaccuracies in the earlier years land cover classification are unavoidable. For the later year the situation has improved by implementing the more up–to-date LUC datasets. However, similar limitations appear with these as well, only the magnitude of the errors is smaller since they are used for a shorter time period. Their effect and source is also very difficult to localize in time or space.

6 ICDR specific adaptations

The CLARA-A3 coverage of 1979-2020 is continued forward through an Interim Climate Data Record (ICDR), processed with the same algorithms but with modifications in inputs to account for the timeliness requirement for a continuous data record production. The spatiotemporal resolution of the ICDR remains exactly the same as for the (T)CDR.

Specifically, the following changes in the ICDR versus the (T)CDR should be noted:

- As the data source for atmospheric composition (pressure, ozone and water vapour content), the ERA5 reanalysis has been switched to the continuously updated ERA5T.
- AOD and ocean wind speeds are based on climatologies (multiyear for AOD, re-use of 2020 for winds)
- Ocean sea ice data source changed to the operationally available OSI-401b data record.
- The AVHRR radiances have not gone through the level of rigorous intercalibration that has been applied to the (T)CDR input; the ICDR data stream is from NOAA CLASS (for details, please refer to the PUM on Cloud Products in CLARA-A3). As a result, perfect consistency in estimated surface albedo should not be expected.
- Metop-C is excluded from ICDR processing until further notice. The reason is that the (vicarious) calibration of AVHRR onboard Metop-C has relied only on 1.5 years of data for the v2017 release and was therefore too uncertain for use. Re-introduction of Metop-C is foreseen once a more robust calibration becomes available in 2023 or later.

While mean differences between the (T)CDR and ICDR have been evaluated to be modest, changes in the instrument constellation, its radiance calibration as well as the atmospheric composition will result in variability in retrieved albedo estimates. Application of the combined CDR+ICDR time series particularly for climate trend analysis should be done carefully, noting the potential for increased uncertainty for the ICDR part.

7 References

Algorithm Theoretical Basis Document for the Cloud Probability of the NWC/PPS, NWC/CDOP3/PPS/SMHI/SCI/ATBD/CloudProbability 2.0 26/04/2021.

Ångström, A. 1929: On the Atmospheric of Sun Radiation and on Dust in the Air, Geogr. Ann., 11, 156-166.

Breuer, L., Eckhardt, K., Frede, H.-G., 2003: Plant parameter values for ecological modeling approaches in temperate climates, Ecol Model, 169, 237 - 293.

DeAbreu, R.A. Jeffrey Key, J.A. Maslanik, M.C. Serreze, and E.F. LeDrew, 1994: Comparison of in situ and AVHRR-derived broadband albedo over arctic sea ice. Arctic, 47(3), 288–297.

Devasthale, A., Raspaud, M., Schlundt, C., Hanschmann, T., Finkensieper, S., Dybbroe, A., and Karlsson, K. G.: PyGAC: an open-source, community-driven Python interface to preprocess more than 30-year AVHRR Global Area Coverage (GAC) data, 2016.

Dybbroe, A., Thoss, A. and K-G. Karlsson, 2005: SAFNWC AVHRR cloud detection and analysis using dynamic thresholds and radiative transfer modelling part I: Algorithm description. Journal of Applied Meteorology, 44, 39–54.

GCOS Secretariat, 2006: Systematic observation requirements for satellite-based products for climate. Technical Report 107, Global Climate Observing System,World Meteorological Organization, 7 bis, Avenue de la Paix P.O. Box No. 2300 CH-1211 Geneva 2, Switzerland.

Govaerts, Y. M., Wagner, S., Lattanzio, A., and Watts, P., 2010: Joint retrieval of surface reflectance and aerosol optical depth from MSG/SEVIRI observations with an optimal estimation approach: 1. Theory, J. Geophys. Res., 115, D02203, doi:10.1029/2009JD011779

Heidinger, A. K., Straka, III, W. C., Molling, C. C., Sullivan, J. T., and Wu, X., 2010: Deriving an inter-sensor consistent calibration for the AVHRR solar reflectance data record, Int. J. Remote Sens., 31, 6493-6517.

Herman, J. R., Bhartia, P. K., Torres, O., Hsu, C., Seftor, C. and Celarier, E., 1997: Global Distribution of UV-Absorbing Aerosols From Nimbus-7/TOMS Data, J. Geophys. Res., 102(D14), 16911 - 16922.

Hofmann, M. and Seckmeyer, G., 2017: A New Model for Estimating the Diffuse Fraction of Solar Irradiance for Photovoltaic System Simulations, Energies, 10, 248. doi:10.3390/en10020248

Jin, Z., T.P. Charlock and K. Rutledge, 2002: Analysis of Broadband Solar Radiation and Albedo over the Ocean Surface at COVE. J. Atmos. Oceanic Technol., 19, 1585–1601.

Jin, Z., T. Charlock, W. Smith Jr., and K. Rutledge, 2004: “A parameterization of ocean surface albedo.” Geophys. Res. Let. 31, L22301, doi:10.1029/2004GL021180.

Jin, Z., Qiao, Y., Wang, Y., Fang, Y. and Yi, W., 2011: A new parameterization of spectral and broadband ocean surface albedo, Optics Express, Vol. 19, Issue 27, pp. 26429-26443.

Jääskeläinen, E. and Manninen, T., 2021: “The effect of snow at forest floor on boreal forest albedo diurnal and seasonal variation during the melting season”, Cold Regions Science and Technology, 185, 103249.

Jääskeläinen, E., Manninen, T., Tamminen, J. and Laine, M., 2017: The Aerosol Index and Land Cover Class Based Atmospheric Correction Aerosol Optical Depth Time Series 1982-2014 for the SMAC Algorithm, Remote Sens. 2017, 9(11), 1095; doi:10.3390/rs9111095 (registering DOI).

Karlsson, K.-G. and Dybbroe, A. 2010: Evaluation of Arctic cloud products from the EUMETSAT Climate Monitoring Satellite Application Facility based on CALIPSO-CALIOP observations. Atmospheric Chemistry and Physics, 10, 1789-1807.

Karlsson, K. G., Anttila, K., Trentmann, J., Stengel, M., Fokke Meirink, J., Devasthale, A., ... & Hollmann, R. 2017. CLARA-A2: the second edition of the CM SAF cloud and radiation data record from 34 years of global AVHRR data. Atmospheric Chemistry and Physics, 17(9), 5809-5828.

Karlsson, K.-G., E. Johansson, N. Håkansson, J. Sedlar, S. Eliasson, 2020: Probabilistic Cloud Masking for the Generation of CM SAF Cloud Climate Data Records from AVHRR and SEVIRI Sensors. Remote Sens. 12, 713. https://doi.org/10.3390/rs12040713

Karlsson, K.-G., Johansson, E., Eliasson, S. Håkansson, N. Hörnquist, S. and Sedlar, J., 2021: Algorithm Theoretical Basis Document for the Cloud Probability product of the NWC/PPS package, EUMETSAT, to be submitted for review.

Kaufman Y.J., Tanré, D., 1996: Strategy for direct and indirect methods for correcting the aerosol effect on remote sensing: From AVHRR to EOS-MODIS, Remote Sensing of Environment, 55(1), pp. 65–79.

Kiss, P., Jánosi, I. M. and O. Torres, 2007: Early calibration problems detected in TOMS Earth-Probe aerosol signal, Geophys. Res. Lett., 34, L07803, doi:10.1029/2006GL028108.

Kotchenova, S. Y., Vermote, E. F., Matarrese, R., & Klemm Jr, F. J., 2006: Validation of a vector version of the 6S radiative transfer code for atmospheric correction of satellite data. Part I: Path radiance. Applied optics, 45(26), 6762-6774.

van Leeuwen, W.J.D. and Roujean, J.L., 2002: Land surface albedo from the synergistic use of polar (EPS) and geo-stationary (MSG) observing systems: An assessment of physical uncertainties. Remote Sensing of Environment, 81, 273–289.

Li, Z. Cihlar, J., Zheng, X., Moreau, L., and Ly, H, 1996: The bidirectional effects of avhrr measurements over boreal regions. IEEE Transactions on Geoscience and Remote Sensing, 34(6), 1308–1322.

Liang, S, 2000: Narrowband to broadband conversions of land surface albedo I: Algorithms. Remote Sensing of Environment, 76, 213–238.

Lucht, W., Schaaf, C.B., and Strahler, A.H., 2000: An algorithm for the retrieval of albedo from space using semiempirical BRDF models. IEEE Transactions on Geoscience and Remote Sensing, Vol. 38 (No. 2): pp. 977–998. doi:10.1109/36.841980.

Manninen, T., N. Siljamo, J. Poutiainen, L. Vuilleumier, F. Bosveld, A. Gratzki, 2004: Cloud statistics based estimation of land surface albedo from AVHRR data. Proc. of SPIE, Remote Sensing of Clouds and the Atmosphere IX, Gran Canaria, Spain, 13-15 September 2004, Vol. 5571, pp. 412 –423.

Manninen, T., Andersson, K. and Riihelä, A., 2011: “Topography correction of the CM-SAF surface albedo product SAL “, Proc. 2011 EUMETSAT Meteorological Satellite Conference, Oslo, CD, 8p.

Manninen, T., Riihelä, A. and Jääskeläinen, E., 2013: ”Subsequent atmospheric correction of the CLARA-SAL surface albedo time series 1982-2009“, Proc. of 2013 EUMETSAT Meteorological Satellite Conference and the 19th Satellite Meteorology, Oceanography and Climatology Conference of the American Meteorological Society (AMS), Vienna 16-20 September 2013, 8 p.

Manninen, T. and Jääskeläinen, E., 2018: “The effect of boreal forest canopy on snow covered terrain broadband albedo”, Geophysica, 53(1), 7–27.

Manninen, T., Jääskeläinen, E. and Riihelä, A., 2019: Black and White-Sky Albedo Values of Snow: In Situ Relationships for AVHRR-Based Estimation Using CLARA-A2 SAL, Canadian Journal of Remote Sensing, 18 p. DOI: 10.1080/07038992.2019.1632177

Manninen, T., Jääskeläinen, E. and Riihelä, A., 2020: Diurnal Black-Sky Surface Albedo Parameterization of Snow. Journal of Applied Meteorology and Climatology, 59 (9): 1415–1428. DOI: https://doi.org/10.1175/JAMC-D-20-0036.1

Manninen, T., Jääskeläinen, E., Siljamo, N., Riihelä, A., & Karlsson, K. G. (2022). Cloud-probability-based estimation of black-sky surface albedo from AVHRR data. Atmospheric Measurement Techniques, 15(4), 879-893.

Manninen, T., Riihelä, A. and Jaaskelainen, E., 2013: Subsequent Atmospheric Correction of the CLARA SAL surface albedo time series 1982-2009, Proc. 2013 EUMETSAT Meteorological Satellite Conference, Wien, 8p.

Nicodemus, F.E., 1970: Reflectance nomenclature and directional reflectance and emissivity. Applied Optics, 9(6), 1474–1475.doi: http://dx.doi.org/10.1175/1520-0469(2002)059<0398:ALTROA>2.0.CO;2

Pinty, B., Lattanzio, A., Martonchik, J.V., Verstraete, M.M., Gobron, N., Taberner, M., Widlowski, J.-L., Dickinson, R.E. and Govaerts, Y., 2005: Coupling Diffuse Sky Radiation and Surface Albedo. Journal of Atmospheric Sciences, 62, 2580-2591.

Proud, S.R., Rasmussen, M.O., Fensholt, R., Sandholt, I., Shisanya, C., Wycliffe, M., Mbow, C. and Anyamba, A, 2010: Improving the SMAC atmospheric correction code by analysis of Meteosat Second Generation NDVI and surface reflectance data. Remote Sensing of Environment, 114(8), 1687-1698.

Rahman, H. and Dedieu, G., 1994: SMAC: a simplified method for the atmospheric correction of satellite measurements in the solar spectrum. International Journal of Remote Sensing, 15, 123-143.

Riihelä A., Laine V., Manninen T., Palo T., Vihma T., 2010: Validation of the CM SAF surface broadband albedo product: Comparisons with in situ observations over Greenland and the ice-covered Arctic Ocean. Remote Sensing of Environment, 114 (11), 2779-2790.

Riihelä, A., Manninen, T., Laine, V., Andersson, K., and Kaspar, F., 2013: CLARA SAL: a global 28 yr timeseries of Earth's black-sky surface albedo, Atmos. Chem. Phys., 13, 3743-3762, doi:10.5194/acp-13-3743-2013.

Román, M. O., and Coauthors, 2010: Assessing the coupling between surface albedo derived from MODIS and the fraction of diffuse skylight over spatially-characterized landscapes. Remote Sens. Environ., 114, 738–760. https://doi.org/10.1016/j.rse.2009.11.014.

Rossow, W. B., & Ferrier, J., 2015: Evaluation of Long-Term Calibrations of the AVHRR Visible Radiances. Journal of Atmospheric and Oceanic Technology, 32(4), 744-766.

Roujean, J.L., Leroy, M., and Deschamps, P-Y., 1992: A bidirectional reflectance model of the earth's surface for the correction of remote sensing data. Journal of Geophysical Research, 97(18), 20455–20468.

Röttgers, R., Doerffer, R., McKee, D. and Schönfeld, W., 2011: Algorithm Theoretical Basis Document, The Water Optical Properties Processor (WOPP), Pure water spectral absorption, scattering, and real part of refractive index model, 20 p.

Schaepman-Strub, G., Schaepman, M.E., Painter, T.H., Dangel, S., Martonchik, J.V., 2006: Reflectance quantities in optical remote sensing – definitions and case studies. Remote Sensing of Environment, 103, 27-42.

Strahler, A. H., Muller, J-P., MODIS Science Team Members, 1999: MODIS BRDF/Albedo Product: Algorithm Theoretical Basis Document Version 5.0. 53 p. http://modis.gsfc.nasa.gov/data/atbd/atbd_mod09.pdf

Song, J. and Gao, W., 1999: An improved method to derive surface albedo from narrowband AVHRR satellite data: narrowband to broadband conversion. Journal of Applied Meteorology, 38, 239–249.

Tanré, D., Deroo, C., Duhaut, P., Herman, M., Morcrette, J. J., Perbos, J., & Deschamps, P. Y. (1990). Technical note Description of a computer code to simulate the satellite signal in the solar spectrum: the 5S code. International Journal of Remote Sensing, 11(4), 659-668.

Tanré, D.; Holben, B.N.; Kaufman, Y.J., 1992: Atmospheric correction against algorithm for NOAA-AVHRR products: theory and application, IEEE TGRS 30(2), pp.231 - 248

Tokinaga, Hiroki & National Center for Atmospheric Research Staff (Eds). Last modified 20 Aug 2013. "The Climate Data Guide: WASWind: Wave and Anemometer-based Sea Surface Wind." Retrieved from https://climatedataguide.ucar.edu/climate-data/waswind-wave-and-anemometer-based-sea-surface-wind.

Thomas, B. R., Kent, E. C., Swail, V. R., & Berry, D. I. (2008). Trends in ship wind speeds adjusted for observation method and height. International Journal of Climatology: A Journal of the Royal Meteorological Society, 28(6), 747-763.

Torres, O., Bhartia, P. K., Herman, J. R., Ahmad, Z.and ,Gleason, J., 1998: Derivation of aerosol properties from satellite measurements of backscattered ultraviolet radiation: Theoretical basis, Journal of Geophysical Research, vol 103, NO. D14, Pages 17099 - 17110.

Toutin, T.,2008: ASTER DEMs for geomatic and geoscientific applications: a review. International Journal of Remote Sensing, 29, pp.1855–1875.

Vazquez, J. Nimbus-7 SMMR Ocean Products:1979-1984. September, 1997. PO.DAAC.

Vermote, E., Tanré, D., Deuzé, J., Herman, M., and Morcrette, J.J., 1997: Second Simulation of the Satellite Signal in the Solar Spectrum, 6S: An Overview. IEEE TGRS, 35(3), 675-686.

Wagner, S. C., Govaerts, Y.M., and Lattanzio, A., 2010: Joint retrieval of surface reflectance and aerosol optical depth from MSG/SEVIRI observations with an optimal estimation approach: 2. Implementation and evaluation, J. Geophys. Res., 115, D02204, doi:10.1029/2009JD011780.

Wang, X. and Zender, C.S., 2011: Arctic and Antarctic Diurnal and Seasonal Variations of Snow Albedo from Multi-year BSRN Measurements. Journal of Geophysical Research (Earth Surface), in press. doi:10.1029/2010JF001864.

Wentz F. J. 1997: A well-calibrated ocean algorithm for SSM/I, J. Geophys. Res., 102, 8703-8718. http://ghrc.nsstc.nasa.gov/uso/ds_docs/ssmi_netcdf/ssmi_ssmis_dataset.html

Wu, A. Li, Z. and Cihlar, J., 1995: Effects of land cover type and greenness on advanced very high resolution radiometer bidirectional reflectances: Analysis and removal. Journal of Geophysical Research, 100(D5), 9179–9192.

Wu, X., Naegeli, K. and Wunderle, S., 2020: Geometric accuracy assessment of coarse-resolution satellite datasets: a study based on AVHRR GAC data at the sub-pixel level. Earth Syst. Sci. Data, 12, 539–553.

https://doi.org/10.5194/essd-12-539-2020

Xiong, X., Stamnes, K. and Lubin D., 2002: Surface albedo over the arctic ocean derived from AVHRR and its validation with SHEBA data. Journal of Applied Meteorology, 41, 413–425.

Yang, F., Mitchell, K., Hou, Y.-T., Dai, Y., Zeng, X., Wang, Z., and Liang, X.-Z., 2008: Dependence of Land Surface Albedo on Solar Zenith Angle: Observations and Model Parametrization. Journal of Applied Meteorology and Climatology, Vol. 47 (No. 11): pp. 2963–2982. doi:10.1175/2008JAMC1843.1.

8 Appendix A: Topography effect on BRDF

Since the BRDF function used in the albedo calculations has been derived for flat terrain (Roujean et al. 1992), it is essential to study theoretically the errors that the flat terrain assumption may cause in mountainous areas. For this purpose a few ASTER DEMs with 30 m x 30 m pixel size were acquired from the Alps (Figure 8-1). The maximum height in that area is 4208 m and the maximum slope is 88°. All aspect angle values naturally exist there, but peaks in the angle distribution are at about 135°, 316° and 226°. Thus the area is not isotropic from the point of view of the sun or a satellite.

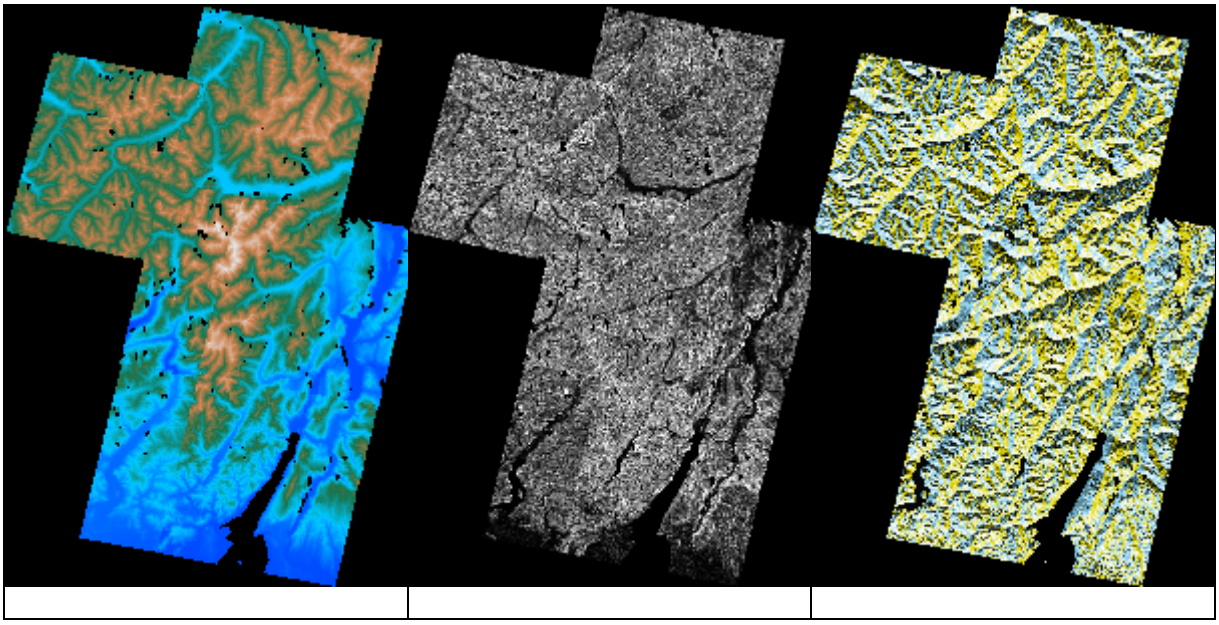

Figure 8-1: The ASTER DEM (left) and corresponding slope (middle) and azimuth (right) angle images from the Alps.

For albedo calculation the BRDF function is needed to describe the 3D-complexity of the target. In the existing version of the CLARA SAL product all pixels are assumed to be horizontal and the BRDF function used is directly that derived for flat terrain (Roujean et al. 1992). If topography information were available the BRDF function of horizontal flat terrain could take the inclination into account just replacing the global angles by the corresponding local angles, i.e. angles with respect to the normal of the terrain pixel. Like for horizontal flat terrain one has to take into account that the pixel should receive sunlight, for which the condition is

$$\sin(\theta_s)\sin(\theta_g)\cos(\varphi_s - \varphi_g) + \cos(\theta_s)\cos(\theta_g) \geq 0 \qquad (75)$$

Moreover, the satellite should also see the pixel, so that

$$\sin(\theta_v)\sin(\theta_g)\cos(\varphi_v - \varphi_g) + \cos(\theta_v)\cos(\theta_g) \geq 0 \quad (76)$$

where

θ_s = Global sun zenith angle

θ_v = Global satellite zenith angle

θ_g = DEM slope angle

θ_s' = Local sun zenith angle

θ_v' = Local satellite zenith angle

φ_s = Global sun azimuth angle

φ_v = Global satellite azimuth angle

φ_g = DEM azimuth angle

φ_s' = Local sun azimuth angle

φ_v' = Local satellite azimuth angle

The relationships between the local and global sun and satellite angles are

$$\cos(\theta_s') = \sin(\theta_s)\sin(\theta_g)\cos(\varphi_s - \varphi_g) + \cos(\theta_s)\cos(\theta_g) \quad (77)$$

$$\cos(\theta_v') = \sin(\theta_v)\sin(\theta_g)\cos(\varphi_v - \varphi_g) + \cos(\theta_v)\cos(\theta_g) \quad (78)$$

The difference between the horizontal terrain and inclined terrain case is that no light comes from below the horizon and the satellite cannot see the terrain from below the horizon (Figure 8-2). Thus the only difference in calculating the BRDF function for inclined terrain is that the variation range of θ_s' and θ_v' is less than 0 … $\pi/2$. The effect of the inclination and azimuth angles of the pixel on the shortwave albedo is estimated for various land cover types in Figure 8-3 to Figure 8-6.

Basically all the land use types have the same kind of errors. When the azimuth angle difference between the terrain normal and the sun viewing direction is larger than 90°, the inclined terrain values would be larger than those of flat terrain, unless the pixel is not seen by the sun or the satellite, when the albedo value is then zero.

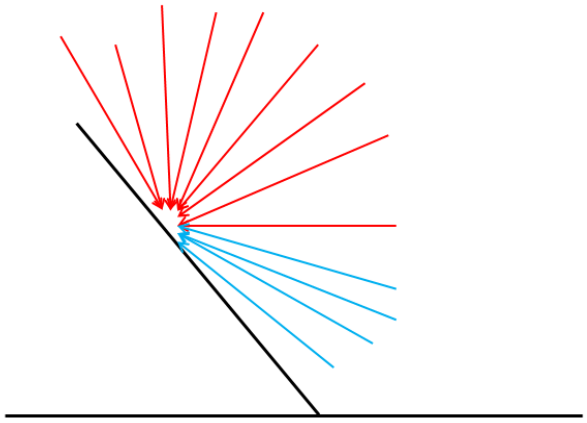

Figure 8-2: The possible sun and satellite zenith angle range for the inclined terrain case (red arrows). The flat terrain case would have a full 0 … 90° range (blue arrows included).

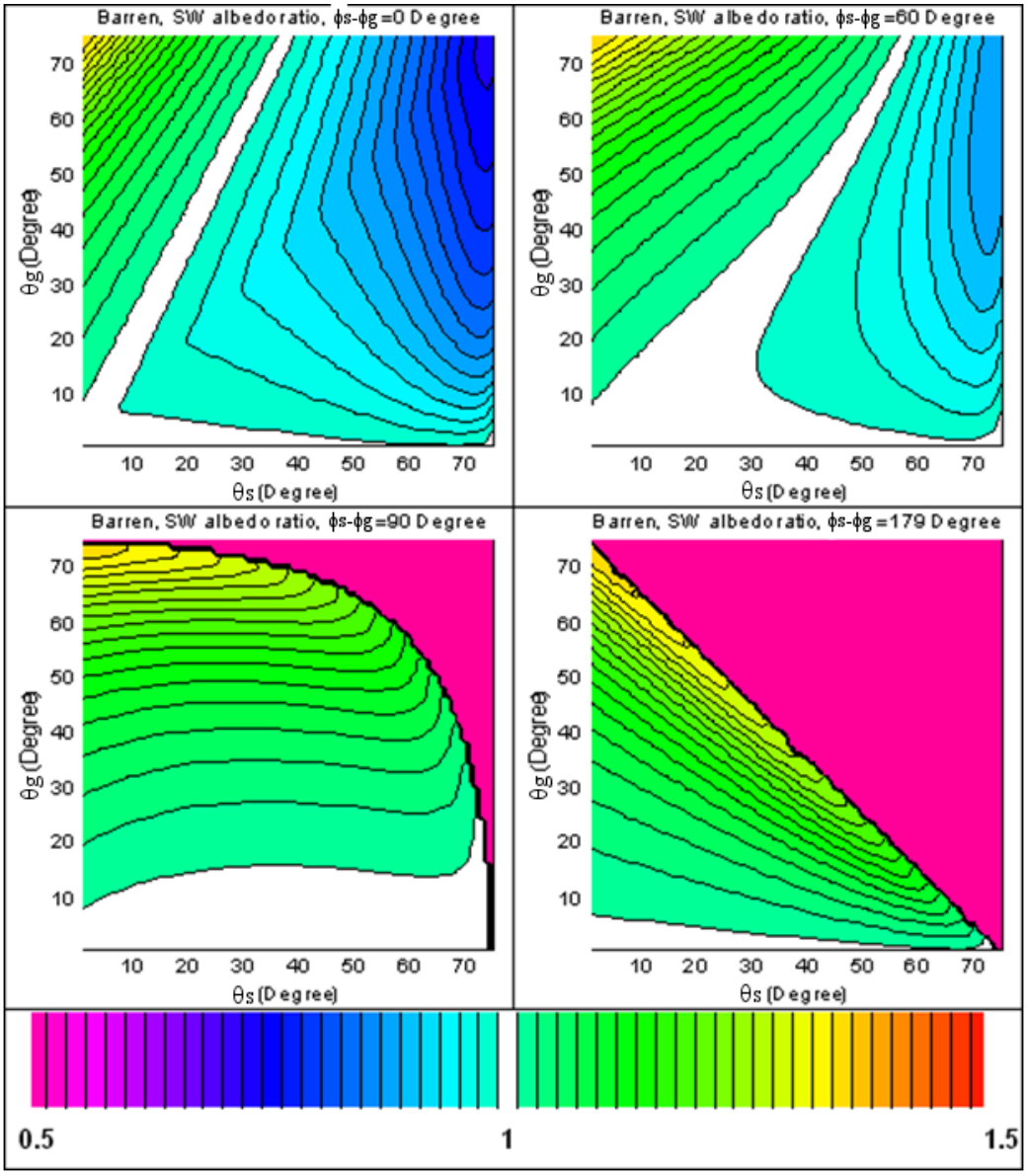

Figure 8-3: The ratio of the inclined and flat terrain short wave albedo of barren land for various ground (θ_g) and sun (θ_s) inclination angle and the azimuth angle difference (ϕ_s-ϕ_g) values. The pink shade of the images corresponding to ϕ_s-ϕ_g=90° and ϕ_s-ϕ_g=179° indicates the angle combinations, which do not contribute to the reflection at all. The lines are spaced with 2 % interval. The white area shows the parameter range producing inclined terrain albedo values matching flat terrain albedo values with ±1% accuracy.

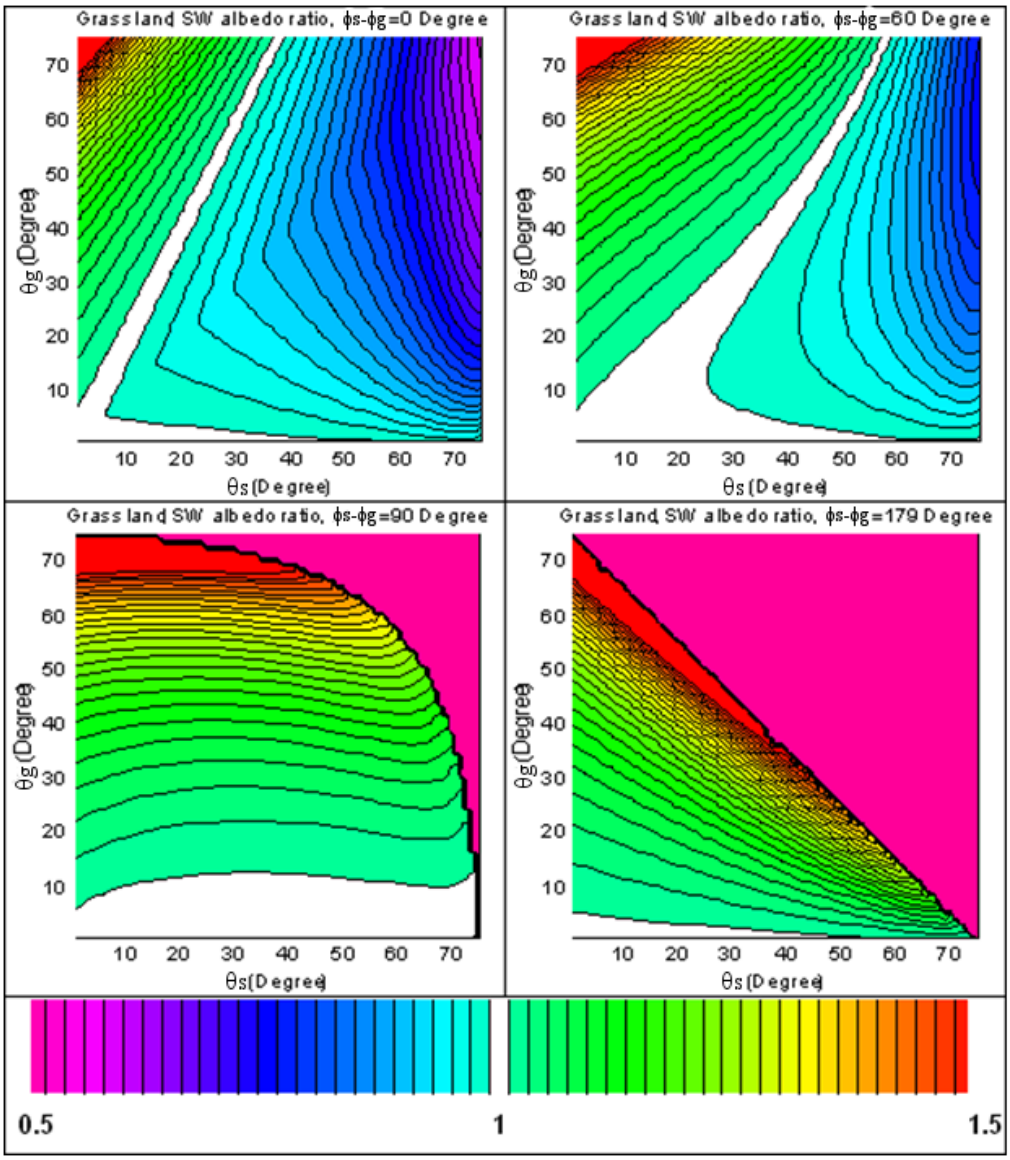

Figure 8-4: The ratio of the inclined and flat terrain short wave albedo of grassland for various ground (θ_g) and sun (θ_s) inclination angle and the azimuth angle difference (ϕ_s-ϕ_g) values. The pink shade of the images corresponding to ϕ_s-ϕ_g=90° and ϕ_s-ϕ_g=179° indicates the angle combinations, which do not contribute to the reflection at all. The lines are spaced with 2 % interval. The white area shows the parameter range producing inclined terrain albedo values matching flat terrain albedo values with ±1% accuracy.

If the sun zenith angle is large (>60 degrees) and the azimuthal difference between the ground normal and the sun viewing direction is moderate (<70 degrees), the inclined terrain albedo values would be smaller than the flat terrain albedo values. For smaller sun elevation (0...40 degrees, depending on the ground inclination angle) and moderate azimuthal difference the inclined terrain would have higher albedo values than the flat terrain. When the azimuth angle difference increases the probability of the inclined terrain albedo to go to zero increases and when the azimuth angle difference is larger than 180°, the albedo value of inclined terrain will be zero independently of the slope steepness and the sun zenith angle. Although increasing slope angle naturally increases the difference between the inclined and flat terrain albedo

value, the azimuth angle of the slope has a larger effect due to complete shadowing probability being so high (larger than 50 % for uniform azimuth angle distribution).

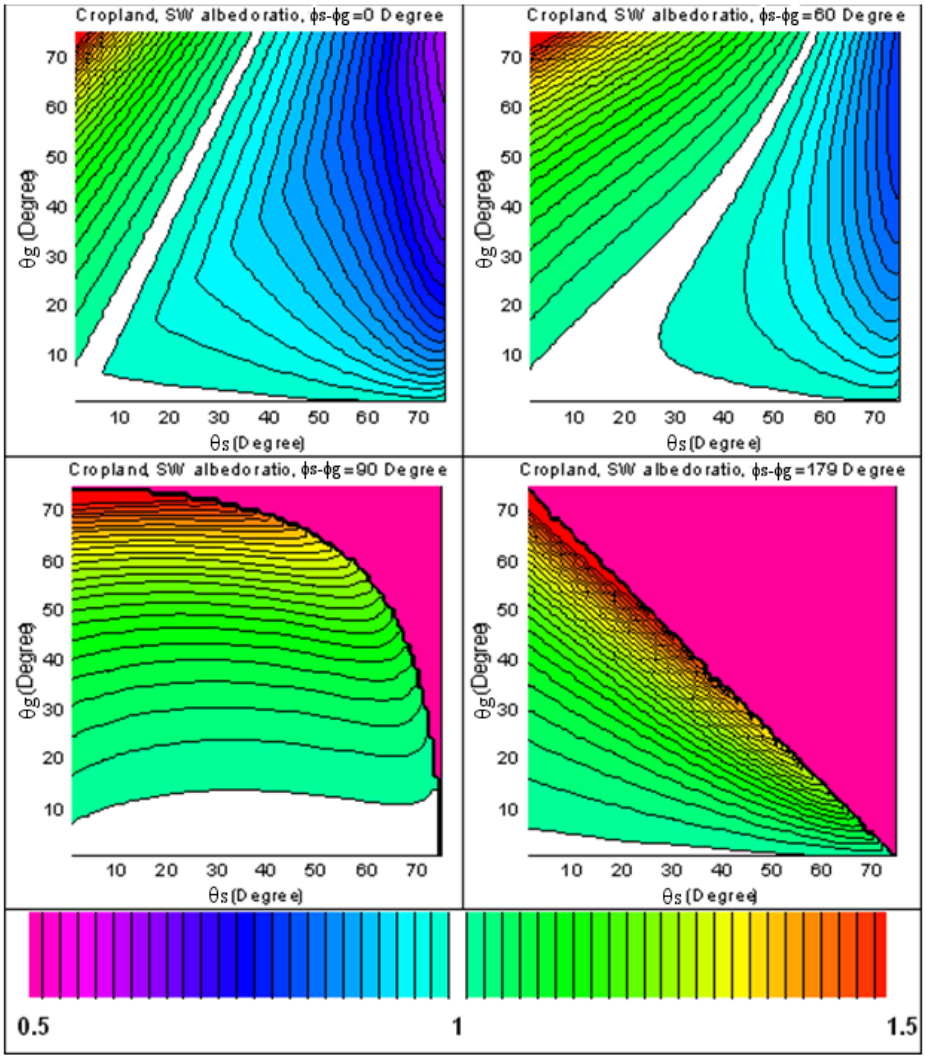

Figure 8-5: The ratio of the inclined and flat terrain short wave albedo of cropland for various ground (θ_g) and sun (θ_s) inclination angle and the azimuth angle difference (ϕ_s-ϕ_g) values. The pink shade of the images corresponding to ϕ_s-ϕ_g=90° and ϕ_s-ϕ_g=179° indicates the angle combinations, which do not contribute to the reflection at all. The lines are spaced with 2 % interval. The white area shows the parameter range producing inclined terrain albedo values matching flat terrain albedo values with ±1% accuracy.

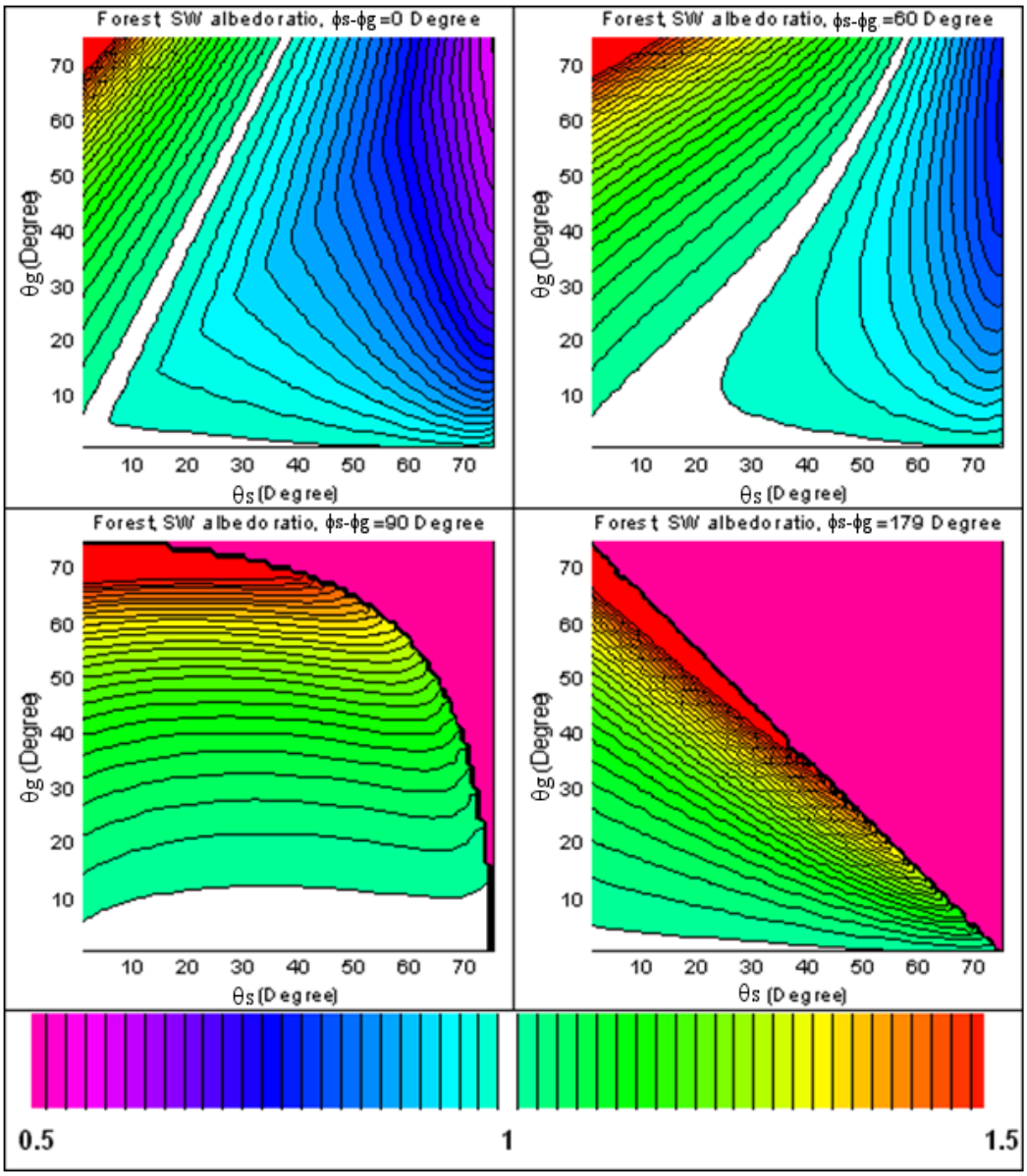

Figure 8-6: The ratio of the inclined and flat terrain short wave albedo of forested land for various ground (θ_g) and sun (θ_s) inclination angle and the azimuth angle difference (ϕ_s-ϕ_g) values. The pink shade of the images corresponding to ϕ_s-ϕ_g=90° and ϕ_s-ϕ_g=179° indicates the angle combinations, which do not contribute to the reflection at all. The lines are spaced with 2 % interval. The white area shows the parameter range producing inclined terrain albedo values matching flat terrain albedo values with ±1% accuracy.

The effect of topography on the albedo of the Alpine test area was calculated using the ASTER slope and aspect images and the USGS land use class. The histograms of the ratio of the true and flat terrain albedos are shown for two sun and satellite angle cases in Figure 8-7. The first case is a favorable one the sun and satellite having as high elevation as realistic and the latter case is an unfavorable one the sun and satellite having their acceptable lower limit zenith angle values. In both cases both overestimates and underestimates of the albedo value will appear, but when the sun and satellite elevation are small (<20 degrees), the inclined terrain tends to have even smaller values.

Since the albedo values vary also with the land use classes the net effect of the topography can be estimated only by calculating the absolute albedo values. The albedo difference images have been produced according to

$$\Delta\, albedo = class\, albedo * \left(1 - albedoratio\right) \tag{79}$$

where the *albedo ratio* is the ratio of the true terrain and flat terrain albedos and the *class albedo* is taken from Table 8-1 .

Table 8-1: The average land use class albedo values derived for the USGS land use classes (http://edcdaac.usgs.gov/glcc/glcc.html) using PlaPaDa data base, urban albedo calculator and Finnish Meteorological Institute (FMI) radiation data of snow covered land (Breuer et al., 2003, http://www.staff.uni-giessen.de/~gh1461/plapada/plapada.html).

	USGS Land use class	Average albedo in percent
1	100 Urban and Built-Up Land	33
2	211 Dryland Cropland and Pasture	23
3	212 Irrigated Cropland and Pasture	23
4	213 Mixed Dryland/Irrigated Cropland and Pasture	23
5	280 Cropland/Grassland Mosaic	23
6	290 Cropland/Woodland Mosaic	23
7	311 Grassland	32
8	321 Shrubland	32
9	330 Mixed Shrubland/Grassland	32
10	332 Savanna	32
11	411 Deciduous Broadleaf Forest	18
12	412 Deciduous Needleleaf Forest	18
13	421 Evergreen Broadleaf Forest	18
14	422 Evergreen Needleleaf Forest	18
15	430 Mixed Forest	18
16	500 Water Bodies	5
17	620 Herbaceous Wetland	32
18	610 Wooded Wetland	18
19	770 Barren or Sparsely Vegetated	23
20	820 Herbaceous Tundra	32
21	810 Wooded Tundra	32
22	850 Mixed Tundra	32
23	830 Bare Ground Tundra	23
24	900 Snow or Ice	70

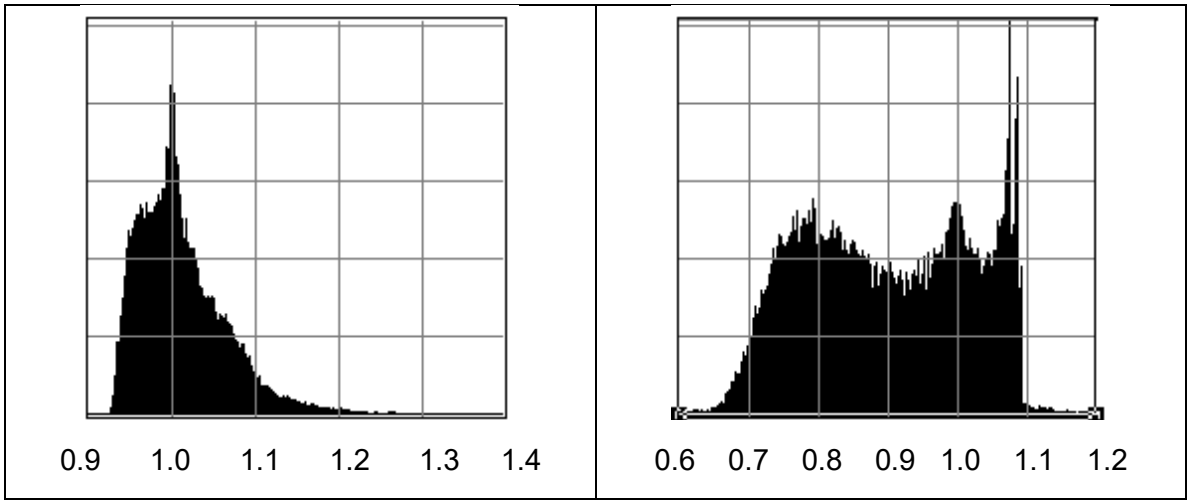

Figure 8-7: The histogram of the true terrain and flat terrain albedo ratio values for the Alpine test area for two sun and satellite angle cases. Left) The sun zenith angle was 31 °, the sun azimuth angle was 141°, the satellite zenith angle was 25° and the satellite azimuth angle was 181°. Right) The sun zenith angle was 70 °, the sun azimuth angle was 118°, the satellite zenith angle was 50° and the satellite azimuth angle was 181°.

The difference between the flat terrain albedo and the true terrain albedo is shown in Figure 8-7 and Figure 8-8 for the two sun and satellite constellations. Typically the albedo of slopes is overestimated. This is natural, since completely shaded slopes have zero albedo values in the image. The mountain tops are covered with permanent snow and there the flat terrain albedo value tends to be smaller than that of inclined terrain. The underestimated land use pixels clearly identifiable in Figure 8-8 belong to the urban land use class for which the same BRDF function type is used as for barren areas. Possibly the average value of urban class of Table 8-1 is too high representing more just the city centre albedo, so that the albedo difference is then too large.

In order to estimate the effect of the topography on AVHRR, details of Figure 8-8 and Figure 8-9 have been median filtered to 1 km x 1 km resolution (

Figure 8-10). Averaging would have caused too drastic effects, because of some extreme values of the albedo ratio. Although the flat terrain albedo values are reasonably good for the favourable sun and satellite constellation, the composite albedo products contain also images corresponding to the unfavourable case, especially at high latitudes where the sun elevation is never high. Thus it is obvious that in rough topography the slope and aspect angles should be taken into account in estimating the BRDF function. Mostly this concerns mountainous areas, but also terrain of moderate height variation may have a quite distinct slope structure.

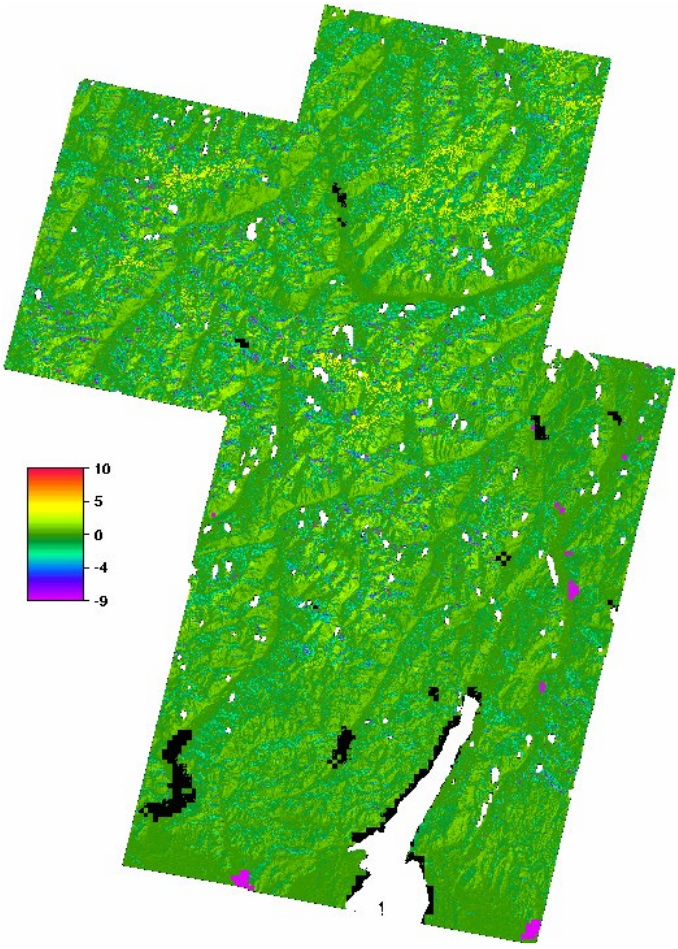

Figure 8-8: The difference between the flat terrain and true terrain albedo values at the Alps. The slope and aspect values were derived from ASTER DEMs and the land use classes from USGS land use map. The sun zenith angle was 31°, the sun azimuth angle was 141°, the satellite zenith angle was 25° and the satellite azimuth angle was 181°

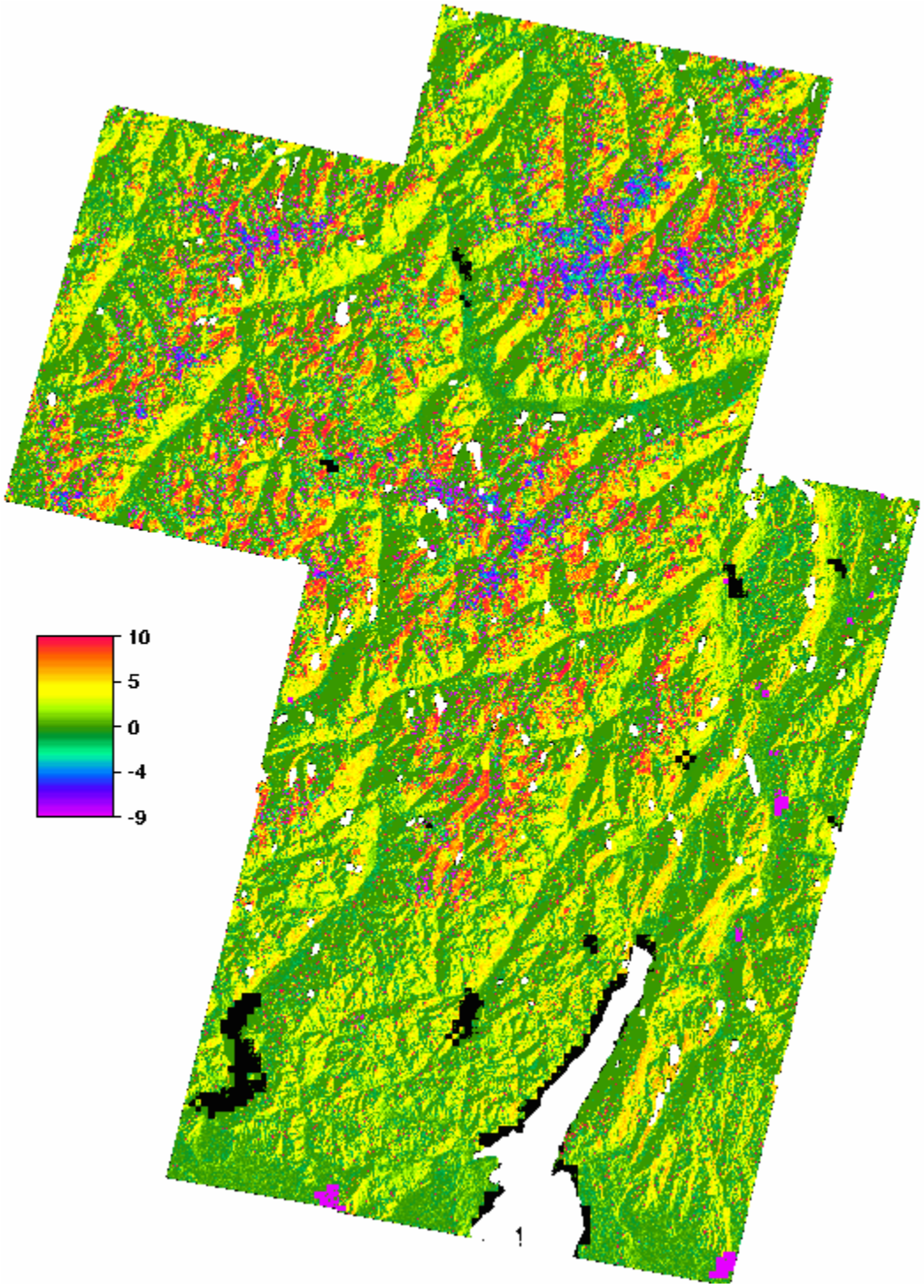

Figure 8-9: The difference between the flat terrain and true terrain albedo values at the Alps. The slope and aspect values were derived from ASTER DEMs and the land use classes from USGS land use map. The sun zenith angle was 70°, the sun azimuth angle was 118°, the satellite zenith angle was 50° and the satellite azimuth angle was 181°.

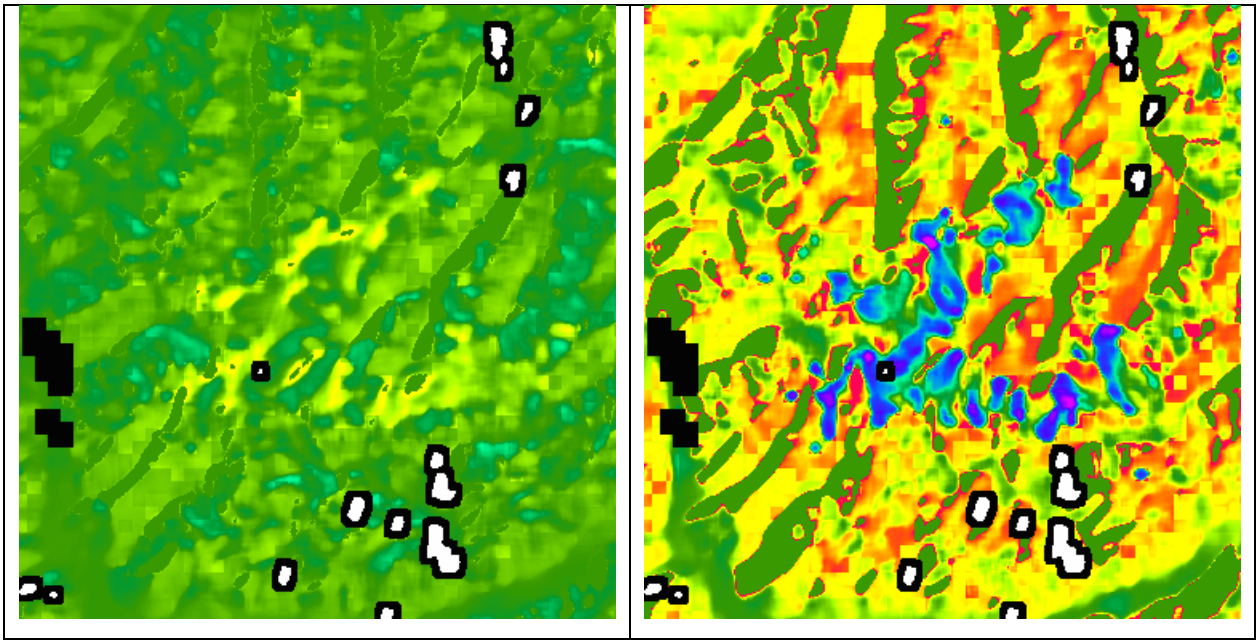

Figure 8-10: The difference between the flat terrain and true terrain albedo values at the Alps. A detail of Figure 7-8 (left) and Figure 7-9 (right) has been median filtered to 1 km resolution to correspond to the CLARA SAL product. The colour code is the same as in those two Figures.

Although the topography correction related to the slopes of the terrain can be determined when the albedos of the individual slope areas are known, the inverse problem cannot be solved deterministically. The reason is that slopes not seen by the sun or the satellite have not contributed to the reflectance value at all, but the topographically corrected surface albedo value of a pixel should be the average of all individual slope area albedo values, when the slopes areas would be in horizontal position. For the shaded pixels the individual albedo values are missing. For an individual image it is not always realistic to assume that the shaded slopes would have the average value of the existing slopes. However, the end products are pentad and monthly averages, which constitute of varying illumination and viewing directions, so that the slopes visible and shaded will be different in the various images. Therefore it is assumed that taking the average albedo value of visible slopes is a reasonable estimate for the shaded slopes.

The calculation of the BRDF for the inclined slopes just assuming that the local incidence and viewing angles have to be used instead of global is a good assumption for many land cover classes, such as snow and sand. For forests one should basically take into account that the tree trunks are often essentially vertical even when the ground is tilted. However, the BRDF model used for forests (Roujean et al. 1992) treats the canopy as a layer of random scatterers without any special attention to tree trunks. Yet the grouping of the trees will affect the radiation characteristics of a canopy. Probably this effect will just average out in coarse resolution images. Hence it is considered justified to use the BRDF model also for forests on inclined slopes.

9 Appendix B: SMAC numeric equations

```
Z    = d - (ω0)*3*(g)*μv*dp + (ω0)*aer_phase/4 ;
X    = c1 - (ω0)*3*(g)*μv*cp1 ;
Y    = c2 - (ω0)*3*(g)*μv*cp2 ;
```

where

```
aer_phase = (a0P) + (a1P)*ξ + (a2P)*ξ*ξ +(a3P)*power(ξ,3) + (a4P)
* power(ξ,4);

ak2 = (1 - (ω0))*(3 - (ω0)*3*(g)) ;
ak   = sqrt(ak2) ;
e    = -3*μs*μs*(ω0) /  (4*(1 - ak2*μs*μs) ) ;
f    = -(1 - (ω0))*3*(g)*μs*μs*(ω0) / (4*(1 - ak2*μs*μs)) ;
dp   = e / (3*μs) + μs*f ;
d    = e + f ;
b    = 2*ak / (3 - (ω0)*3*(g));
del = exp( ak*τp )*(1 + b)*(1 + b) - exp(-ak*τp)*(1 - b)*(1 - b)
;
ww   = (ω0)/4;
ss   = μs / (1 - ak2*μs*μs) ;
q1   = 2 + 3*μs + (1 - (ω0))*3*(g)*μs*(1 + 2*μs) ;
q2   = 2 - 3*μs - (1 - (ω0))*3*(g)*μs*(1 - 2*μs) ;
q3   = q2*exp( -τp/μs ) ;
c1   = ((ww*ss) / del) * (q1*exp(ak*τp)*(1 + b) + q3*(1 - b) ) ;
c2   = -((ww*ss) / del) * (q1*exp(-ak*τp)*(1 - b) + q3*(1 + b) )
;
cp1 =  c1*ak / ( 3 - (ω0)*3*(g) ) ;
cp2 = -c2*ak / ( 3 - (ω0)*3*(g) ) ;
```

in the preceding code, a0P, a1P, a2P, a3P and a4P are predefined constants from the SMAC coefficient file.

10 Appendix C: Symbols

Physical symbols

Symbol	Meaning	Unit
α	albedo	unitless
θ	zenith angle	Degrees
φ	azimuth angle	Degrees
ρ	Reflectance from a direction to a direction	sr^{-1}
L	Radiance	$W \cdot sr^{-1} \cdot m^{-2}$
E	Irradiance	W / m^2
Ω	Anisotropy factor (reflectance relative to nadir)	sr^{-1}
P	Surface pressure	mbar
T_{550}	AOD at 550 nm	unitless
λ	Wavelength	m
Γ	Fraction of the difference and sum of red and NIR reflectance	unitless
γ	Scattering angle	Degrees
f	Frequency	Hz
F	Radiant Flux	W
R	Reflectivity	unitless

11 Glossary – List of Acronyms in alphabetical order

AI	Aerosol Index
AOD	Aerosol Optical Depth
AVHRR	Advanced Very High Resolution Radiometer (NOAA)
BB	Broadband
BRDF	Bidirectional Reflectance Distribution Function
BSRN	Baseline Surface Radiation Network
CDR	Climate Data Record
CLARA	cLouds, ALbedo and Radiation dataset family
CM SAF	Satellite Application Facility on Climate Monitoring
COART	Coupled Ocean-Atmosphere Radiative Transfer
DEM	Digital Elevation Model
DOY	Day of Year
DWD	Deutscher Wetterdienst
ECMWF	European Center for Medium-Range Weather Forecasts
ECV	Essential Climate Variable
EUMETSAT	European Organisation for the Exploitation of Meteorological Satellites
EPS	Enhanced Polar System
FMI	Finnish Meteorological Institute
FCDR	Fundamental Climate Data Record
GAC	Global Area Coverage
GACSAL	Global Area Coverage Surface Albedo
GCOS	Global Climate Observing System
ICDR	Interim Climate Data Record
IPCC	Intergovernmental Panel on Climate Change
KNMI	Koninklijk Nederlands Meteorologisch Instituut (Royal Netherlands Meteorological Institute)
LUC	Land Use Classification

LUT	Look-Up Table
MODIS	Moderate Resolution Imaging Spectroradiometer
NIR	Near InfraRed
NDVI	Normalized Difference Vegetation Index
NOAA	National Oceanic and Atmospheric Administration
NTB (C)	Narrow-to-Broadband (Conversion)
NWC-SAF	Nowcasting Satellite Application Facility
NWP	Numerical Weather Prediction
OSI-SAF	Ocean and Sea Ice Satellite Application Facility
PNG	Portable Network Graphics
PPS	Polar Platform System
PUM	Product User Manual
RMIB	Royal Meteorological Institute of Belgium
SAF	Satellite Application Facility
CLARA BAL	The CM SAF cLoud, Albedo and RAdiation dataset from AVHRR data – Blue-sky Surface Albedo
CLARA SAL	The CM SAF cLoud, Albedo and RAdiation dataset from AVHRR data – Black-sky Surface Albedo
CLARA WAL	The CM SAF cLoud, Albedo and RAdiation dataset from AVHRR data – White-sky Surface Albedo
SEVIRI	Spinning Enhanced Visible and Infra-Red Imager
SMAC	Simplified method for the atmospheric correction of satellite measurements in the solar spectrum
SMHI	Swedish Meteorological and Hydrological Institute
SMMR	Scanning Multi-channel Microwave Radiometer
SRTM	Shuttle Radar Topography Mission
SSM/I	TCDR Special Sensor Microwave Imager
SSMIS	Special Sensor Microwave Imager Sounder
SZA	Sun Zenith Angle

TCDR	Thematic Climate Data Record
TOA	Top of Atmosphere
TOMS	Total Ozone Mapping Spectrometer
UNFCCC	United Nations Framework Convention on Climate Change
USGS	United States Geological Survey
VTT	Technological Research Centre of Finland Ltd
VZA	Viewing Zenith Angle